HHS Public Access

Author manuscript

Chem Soc Rev. Author manuscript; available in PMC 2018 November 27.

Published in final edited form as:

Chem Soc Rev. 2017 November 27; 46(23): 7438–7468. doi:10.1039/c7cs00316a.

Engineering of inorganic nanoparticles as magnetic resonance imaging contrast agents

Dalong Ni[a,b,c], **Wenbo Bu**[a,b], **Emily B. Ehlerding**[c], **Weibo Cai**[c], and **Jianlin Shi**[a,b]

[a]State Key Laboratory of High Performance Ceramics and Superfine Microstructures, Shanghai Institute of Ceramics, Chinese Academy of Sciences, Shanghai, 200050, China

[b]Shanghai Key Laboratory of Green Chemistry and Chemical Processes, School of Chemistry and Molecular Engineering, East China Normal University, Shanghai, 200062, China

[c]Departments of Radiology and Medical Physics, University of Wisconsin-Madison, Wisconsin 53705, USA

Abstract

Magnetic resonance imaging (MRI) is a highly valuable non-invasive imaging tool owing to its exquisite soft tissue contrast, high spatial resolution, lack of ionizing radiation, and wide clinical applicability. Contrast agents (CAs) can be used to further enhance the sensitivity of MRI to obtain information-rich images. Recently, extensive research efforts have been focused on the design and synthesis of high-performance inorganic nanoparticle-based CAs to improve the quality and specificity of MRI. Herein, the basic rules, including the choice of metal ions, effect of electron motion on water relaxation, and involved mechanisms, of CAs for MRI have been elucidated in detail. In particular, various design principles, including size control, surface modification (*e.g.* organic ligand, silica shell, and inorganic nanolayers), and shape regulation, to impact relaxation of water molecules have been discussed in detail. Comprehensive understanding of how these factors work can guide the engineering of future inorganic nanoparticles with high relaxivity. Finally, we have summarized the currently available strategies and their mechanism for obtaining high-performance CAs and discussed the challenges and future developments of nanoparticulate CAs for clinical translation in MRI.

1. Introduction

Diagnostic imaging techniques to detect lesion information (*e.g.*, type, location, and stage) are currently playing diverse roles in the combat against serious diseases such as cancer.[1-3] Among all existing imaging techniques, magnetic resonance imaging (MRI) is a popular choice because of its exquisite soft tissue contrast, high spatial resolution, lack of ionizing radiation, unlimited signal penetration depth, and wide clinical applicability.[4] Contrast agents (CAs) can be used to further improve the sensitivity and detection capability of MRI. The use of CAs in MRI has greatly expanded the possible conditions that may be explored,

Correspondence to: Wenbo Bu; Weibo Cai; Jianlin Shi.

Conflicts of interest

There are no conflicts to declare.

offering physicians unprecedented noninvasive visualization of many ailments.[5,6] Most clinically available CAs are chemical agents, traditionally gadolinium (Gd^{3+}) chelates. Generally, these Gd^{3+} chelates have very short circulation lifetimes in the body, work in a nonspecific manner, and have certain limitations as molecular CAs for long-time tracking. Another disadvantage of clinically used Gd^{3+} chelates is their relatively low proton relaxation efficiency, which means that high doses are necessary for imaging (*e.g.*, mM concentrations of Gd^{3+} chelates at target areas).[7] However, high-dose injection of Gd^{3+} chelates may be harmful to the body as it has been reported that the released free Gd^{3+} ions may cause severe nephrogenic system fibrosis syndrome *in vivo*.[8] Therefore, the imaging performances of clinically available CAs to date have been far from optimal.

Nanoparticles naturally lend themselves to be used as CAs in MRI, where magnetically responsive atoms are essential.[9] T_1 or spin–lattice contrast may be enhanced through the use of paramagnetic centers such as gadolinium[10,11] or manganese ions,[12,13] whereas iron oxide-based nanosystems are often used for T_2-weighted[14-16] or spin–spin imaging. Unlike other molecular imaging agents, these nanoparticles are not directly imaged in the resulting MRI image; in fact, the metal ions perturb the magnetic properties of protons around them, which are the actual target of a traditional MRI scan.[6] Among various types of nanoscale imaging agents, inorganic nanoparticle (NP)-based CAs (hereafter, “NPs” refers to inorganic nanoparticles) have received great attention and have been regarded as promising imaging probes. This is due to their unique electronic, magnetic and optical properties at the nanoscale, facile intracellular uptake and accumulation, and excellent *in vivo* stability.[17] The high surface areas of these NPs also greatly enhance their chemical reactivity, allowing for easy surface modification with biological and bioactive materials. These characteristics have caused NPs to emerge as promising candidates for next-generation imaging CAs.[18]

The contrast behavior of NPs strongly depends on their perturbation of magnetic properties of nearby protons, which can be tuned through a series of factors (*e.g.*, size, surface, and shape) and various innovative approaches or strategies. Great efforts have been made for the rational design and manufacture of NPs with high relaxivity to elevate imaging sensitivity of CAs and even impart MRI with molecular imaging capabilities for better monitoring of biological processes (*e.g.*, tumor microenvironment, cell tracking, and cellular interactions). This has resulted in the wide expansion of this research area, leading to the formation of sub-branches such as ultra-high field MRI,[19-21] multi-modal imaging,[22-24] and incorporation of theranostic techniques into MRI.[25]

Both the rational design and engineering of nanoparticulate CAs play important roles in this field, whichmay, inthemeantime, broaden biomedical applications of MRI. However, the complexity of this process is much greater than initially expected, calling for broad expertise in a multidisciplinary manner through chemistry, physics, biology, and engineering. The goal of this review is not to comprehensively summarize nanoparticulate CAs for MRI that have been reported so far,[26] as there are many reviews available that list the major types of NPs as CAs (Gd^{3+}-based T_1 CAs,[11,27] magnetic T_2 CAs,[14,15,28-30] and dual- T_1/T_2 CAs[9,31]) or summarize a special application of CAs (*e.g.*, bioresponsive CAs,[32-34] and multimodal CAs[24]). Instead, this review intends to comprehensively discuss the main rules and mechanisms of nanoparticulate CAs, key factors influencing the relaxation of CAs, and

innovative strategies to engineer CAs with high relaxivity. As the Chinese aphorism goes, “It is better to teach a man to fish than to give him a fish,” we hope that this timely and comprehensive review can familiarize readers with the general principles of designing high-performance CAs, stimulate extensive further studies, and attract extensive attention from researchers worldwide.

2. Basic rules for MRI contrast agents

Since the mechanisms of MRI have been thoroughly described elsewhere,[11,29] herein, we will focus on the basic rules of CAs for MRI, an in-depth understanding of which is extremely important for formulating design principles of CAs. The contrast enhancement of MRI originates from the interaction between CAs and surrounding water protons, which shorten the longitudinal (T_1) or transverse (T_2) relaxation time of nearby water molecules. Usually, T_1 CAs are applied to increase signal intensity, resulting in a positive contrast enhancement (brighter image) in T_1-weighted MRI, whereas T_2 CAs can decrease signal intensity, providing a negative contrast enhancement (darker image) in T_2-weighted MRI. Relaxivity (r_i, i = 1, 2) is therefore used to evaluate the efficacy of CAs, which is defined as the slope of a plot of relaxation rate ($1/T_i$, i = 1, 2) *versus* concentration of CAs:

$$1/T_i = 1/T_{i0} + r_i C \quad (1)$$

where T_{i0} is the relaxation time without CAs and C is the concentration of CAs (mM). The values of r_1, r_2, and r_2/r_1 are typically used to evaluate MRI efficiency of nanoparticulate CAs. The transition metal ions (Mn^{2+}, Fe^{2+}/Fe^{3+}, Co^{2+}, and Cu^{2+}) and lanthanide metal ions (Eu^{3+}, Gd^{3+}, Ho^{3+}, and Dy^{3+}) are the major candidate relaxation centers that can be utilized to construct NPs with proper chemical compositions for enhanced contrast in MRI. The choice of a metal ion requires consideration of its electron motion, nanostructure-dependent effects, and involved relaxation mechanism to obtain high-relaxivity CAs.

2.1 Choice of ions

The selection of appropriate ions to construct nanoparticulate agents should obey certain rules. Inherently, one metal ion includes both the electron orbital motion and electron spin motion. The fast electron orbital motion is significantly higher than the speed of water proton relaxation, while the electron spin motion is slower and can be closely in tune with the slow water proton relaxation. Only the electron spinmagneticmoment of ions can efficiently influence the longitudinal water proton relaxation (r_1). Therefore, r_1 will be higher if the total electron angular momentum (J) contains a larger contribution from electron spin angular momentum (S) of adjacent ions. On the other hand, it will be small if J consists only of electron orbital angular momentum (L).[35] Table 1 summarizes the outer orbital, quantum parameters (S, L, and J) and effectivemagnetic moment (μ_{eff}) of candidate metal ions for MRI, from which we can determine suitable ions for chemical composition of CAs. For example, since Gd^{3+} has seven unpaired electrons and its J (J = 7/2) value is completely derived from S (S = 7/2, L = 0), inorganic Gd^{3+}-based NPs (*e.g.*, Gd_2O_3, $NaGdF_4$, GdF_3) have been widely explored as T_1 CAs.[36-49] Notably, Mn^{2+} plays a highly important role in biological processes as a cofactor of enzymes and through neurotransmitter

release control; moreover, Mn^{2+} has five unpaired electrons ($J = 5/2$, $S = 5/2$, $L = 0$), showing prominent contrast effects that have been shown to enable visualization of brain anatomic structure and its neuronal activity.[50] Therefore, Mn^{2+}-based NPs constitute a new imaging category and are promising candidates as T_1 CAs.[51-69]

The r_2 of a CA is largely proportional to the square of μ_{eff} of the ion, as T_2 CAs show reduced signal dependence on induced magnetic moment of these CAs.[70] Among all lanthanide ions, Dy^{3+} (together with Ho^{3+}) has the highest effective magnetic moment ($\mu_{eff} = 10.6\ \mu_B$) and much attention has been paid to synthesizing Dy^{3+}- or Ho^{3+}-based NPs as T_2 CAs,[70-72] especially for ultra-high field imaging.[19-21,73] Studies of D-glucuronic acid-coated ultra-small Ln_2O_3 NPs (Ln = Eu, Gd, Dy, Ho, or Er) show that Gd_2O_3 NPs exhibit the highest r_1 value, whereas Dy_2O_3 NPs possess the highest r_2 value among all studied NPs.[74] Unlike the lanthanides, iron is one of the most abundant metal elements in living organisms and deeply involved in various biological processes including cellular respiration by redox enzymes and oxygen transport by hemoglobin.[75] Magnetic iron oxide NPs (*e.g.*, Fe_3O_4, γ-Fe_2O_3, $Fe@Fe_3O_4$, $MnFe_2O_4$, *etc.*) are therefore very popular T_2 CAs that can produce negative imaging contrast.[29,30,76-84] The magnetization of paramagnetic NPs, such as Gd-based NPs and Mn-based NPs, directly depends on the total number of metal ions, and no magnetization is present in the absence of an external magnetic field. However, magnetic iron oxide NPs exhibit strong intrinsic magnetization, which may cause microscopic field inhomogeneity and accelerate the dephasing of protons for MRI contrast enhancement when an external magnetic field is applied.

In addition to relaxation impact from ion species, the ion valency also affects relaxation interaction between ions and water protons. Variable valencies (*e.g.*, Mn^{4+}/Mn^{2+} ions,[54] Co^{3+}/Co^{2+} ions,[85] Eu^{3+}/Eu^{2+} ions[86]) can endow these ions with tunable MRI performance under certain reducing or oxidative microenvironments, thus creating responsive MRI CAs for molecular imaging.[32] Mn^{4+}-based NPs are widely used as pH or redoxresponsive MRI CAs because Mn^{4+} ($J = 9/2$, $S = 3/2$, $L = 3$) with negligible relaxation interactions can be easily reduced to Mn^{2+} ($J = 5/2$, $S = 5/2$, $L = 0$), which shows high MRI contrast capability according to the rules mentioned above. Overall, understanding the basic principles of NPs such as ion species, ion valency, and magnetic properties will facilitate the engineering of nanoparticulate CAs with excellent MRI performance for various applications.

2.2 Mechanisms of contrast enhancement

The relaxation enhancement of water protons near a paramagnetic center generally follows the inner sphere, secondary sphere, and outer sphere mechanism (Fig. 1).[87] The water molecules directly coordinated to the paramagnetic center are responsible for inner sphere relaxation contribution, while bulk water molecules in the nearby environment affect outer sphere relaxation. In some cases, water molecules that are hydrogen bonded to chelators are regarded as the secondary sphere. The contrast enhancement of individual CAs closely depends on their chemical composition, structure, and surfacemodification.

For T_1 CAs, on the basis of the classical Solomon–Bloembergen–Morgan (SBM) theory,[35,87,88] common strategies for enhancing relaxivity mainly include increasing the number of bound water molecules (q), enhancing rotational correlation time (τ_R), and

optimizing water residence time (τ_M). Higher τ_R values imply slower molecular tumbling and lead to increased proton relaxivity. τ_M is the inverse of water exchange rate in the inner sphere ($k_{ex} = 1/\tau_M$), which is favorable for proton relaxivity in the case of fast water exchange (high k_{ex}). The relationship between τ_R and τ_M can be described by the following equation:[89]

$$1/\tau_{ci}=1/T_{ie}+1/\tau_R+1/\tau_M \quad i=1,2 \qquad (2)$$

where τ_c is the correlation time parameter and T_{ie} (i = 1, 2) is the electronic relaxation time. Since it is challenging to predict and experimentally alter T_{ie}, approaches to obtain highly efficient CAs commonly focus on the regulation of τ_R and τ_M.[37] By immobilizing Gd^{3+} on the surface or lattice of NPs, prolonging τ_R will result in significantly enhanced r_1, which is a commonly used strategy because these nanoparticulate CAs can couple the tumbling rate of Gd^{3+} chelates to that of much larger species (*e.g.*, titanium, gold, and silica NPs).[90-98] Another widely used approach to enhance r_1 is the optimization of τ_M,[99,100] which is readily accessible because nanoparticulate CAs inherently have relatively slow tumbling rates.

Different from T_1 CAs that influence the relaxation of water proton through direct energy exchange between water and paramagnetic ions,[101] magnetized NPs can induce increased T_2 relaxivity, which reduces phase coherence of water molecules in an inhomogeneous magnetic field generated by magnetized NPs.[102-104] Based on the quantum mechanical outer sphere theory, T_2 relaxivity is given by eqn (3)[105]

$$1/T_2=(256\pi^2\gamma^2/405)V^*M_s{}^2r^2/D(1+L/r) \qquad (3)$$

where r and M_s are the effective radius of magnetic NPs and saturation magnetization, respectively, γ is the proton gyromagnetic ratio, V^* is the volume fraction, D is the diffusivity of water molecules, and L is the thickness of an impermeable surface shell on the magnetic core. It should be noted that M_s value of a magnetic NP can be tuned by its high surface area, where the interior spins of magnetic NPs are usually aligned, while the spins of surface atoms are magnetically disordered. This is known as the spin canting effect, which is non-negligible because NPs have a large surface-to-volume ratio.[29] According to eqn (3), T_2 relaxivity of magnetic NPs is highly dependent on effective radius of the magnetic core, M_s, and thickness of an impermeable surface.

3. Factors influencing relaxivity of MRI contrast agents

Recently, great advances in nanotechnology have stimulated the quick development of nanoparticulate CAs, which have two main traits of interest: the dominant quantum confinement effect and the large surface area. Size-dependent magnetic, electronic, and optical properties originating from dominant quantum confinement effects can be utilized in the rational design of high-performance MRI CAs at the nanoscale. Moreover, the large surface area of NPs offers increased chemical reactivity for surface modification with additional functional species, enabling enhanced magnetic relaxivity and higher-quality MRI

with reasonable detection limits. Typically, three techniques are applied for obtaining high-relaxivity CAs at the nanoscale: size control, surface modification, and shape regulation (Fig. 2).

3.1 Size effects

Inorganic NPs present a unique size-dependent effect on physical properties including surface plasmon resonance of metal nanoparticles,[106,107] fluorescence emission of semiconductor NPs,[108] and superparamagnetism or heating of magnetic NPs.[109,110] By controlling nucleation and growth, the size of NPs can be well controlled. The dependence of cellular uptake, biodistribution, and clearance rate on NP size has been widely investigated by many groups.[111-115] To date, several types of CAs have been developed for various applications in MRI, which can be classified according to their chemical composition (Gd-, Mn-, Fe-, Dy- or Ho-based CAs; Table 2). A deep understanding of the involved mechanisms between size effect and proton relaxation will undoubtedly benefit the rational design of T_1 or T_2 CAs for high-performance MRI. For T_1 CAs, smaller-sized NPs usually generate greater contrast enhancement because their surface-to-volume ratio is the dominant contributing factor, which increases as the size of NPs is decreases. However, τ_R will become much lower for large NPs and plays a dominant role in affecting relaxivity, causing larger NPs to possess higher r_1 values. For T_2 CAs, larger-sized magnetic NPs usually have higher magnetization than smaller-sized NPs, and therefore, r_2 values increase as size increases. However, this trend breaks down when sizes of magnetic NPs become too large.

3.1.1 Gd-based contrast agents—The recently developed Gd^{3+}-based NPs such as Gd_2O_3-,[43-45,116] $NaGdF_4$-,[36,38-41] GdF_3-,[46,117,118] and Gd^{3+}-doped NPs (*e.g.*, quantum dots,[119-123] upconversion NPs,[124-126] and carbon dots[127,128]) have been regarded as promising T_1 CAs because of their controllable size and morphology. By optimizing the reaction parameters during both nucleation and growth, Johnson *et al.* synthesized size-tunable ultra-small $NaGdF_4$ NPs with uniform sizes of around 2.5 nm, 4 nm, 6.5 nm, and 8 nm (Fig. 3a) and found that the r_1 value increased dramatically with decreasing size from 3.0 mM^{-1} s^{-1} for 8.0 nm NPs to 7.2 mM^{-1} s^{-1} for the smallest 2.5 nm ones (Fig. 3b).[49] Correlations of NPs' sizes and their r_1 values showed that contributions from the surface-tovolume ratio increased with decreasing NP size, becoming the dominant contributing factor. Several other research groups also reported similar size effects of $NaGdF_4$ NPs on relaxivity.[36,39] However, τ_R became much lower for larger $NaGdF_4$ NPs (>15 nm) and played a dominant role in affecting r_1 value, as demonstrated by Gao and co-workers, who found r_1 values of 5.7 mM^{-1} s^{-1} for 15 nm $NaGdF_4$ NPs, which increased to 8.78 mM^{-1} s^{-1} for 20 nm ones (Fig. 3c).[41] Inspired by this, we recently synthesized ultra-small sized and renal-clearable $NaGdF^4$ nanodots (~2 nm) with high r_1 values of 8.93mM^{-1} s^{-1}.[40] These nanodots exhibited excellent magnetic resonance angiography (MRA) performance, as the vascular signal was much stronger than that achieved using clinical MRI CAs (Fig. 3d). With the new CAs, even capillary vessels and atherosclerotic plaques could be clearly delineated (Fig. 3e).

The same trends were also observed for ultra-small Gd_2O_3 NPs,[45,129] such that r_1 values increased from 4.4 mM^{-1} s^{-1} (4.6 nm Gd_2O_3) to 8.8 mM^{-1} s^{-1} (2.2 nm Gd_2O_3).[45] Based on the fitting of Gaussian, Lorentzian, and log-normal functions, Lee *et al.* concluded that the optimal range of diameters for high-relaxivity Gd_2O_3 NPs should be 1–2.5 nm with a theoretical maximum r_1 value of 10.1–10.6 mM^{-1} s^{-1}.[48] In that study, they reported a large r_1 value of 9.9 mM^{-1} s^{-1} of ultra-small Gd_2O_3 NPs coated with D-glucuronic acid. Consistent with ultra-small $NaGdF_4$ NPs, such a large r_1 value of ultra-small Gd_2O_3 NPs was attributed to the large surface-to-volume ratio, as well as the cooperative induction of surface Gd^{3+} ions for longitudinal relaxation. It is generally accepted that the r_1 value should be as large as possible, and for high-performance T_1 MRI CAs, the r_2/r_1 ratio should be close to unity, while a greater value of r_2/r_1 will generally result in higher contrast enhancement efficiency for T_2 MRI CAs.[9] The r_2/r_1 ratio of ultra-small Gd_2O_3 NPs was estimated to be 1.06 (r_1 = 9.9 mM^{-1} s^{-1}, r_2 = 10.5 mM^{-1} s^{-1}), which seemed to satisfy this condition.

Biologically, these ultra-small sized agents can escape from recognition and can be capture by the liver and then be rapidly cleared through the kidneys, in which the basal lamina has pores of approximately 10 nm to filter metabolites (*e.g.*, ultrasmall sized NPs) from the bloodstream.[38,48,130] Such rapid renal clearance diminishes *in vivo* toxicity of NPs owing to the suppressed tissue accumulation and certainly facilitates their future clinical translation and application. In addition, ultrasmall Gd^{3+}-based NPs can be integrated with additional components such as multifunctional nanoplatforms for non-targeted blood pool imaging,[40] targeted molecular imaging,[41] pH/H_2O_2- responsive MRI,[131] and brain tumor diagnosis and image-guided therapy.[130]

3.1.2 Mn-based contrast agents—As another major class of T_1 CAs, Mn-based NPs (*e.g.*, MnO NPs, Mn_3O_4 NPs, and MnO_2 nanosheets) have gained extensive interest as GSH- or pHresponsive MRI CAs due to their readily changeable valency and easy release of manganese under acidic conditions.[54,55,63,133] The size-dependent magnetic properties of MnO and Mn_3O_4 NPs with monodispersed sizes in the range of 6–22 nm were initially reported by Seo *et al.*[134] Subsequently, the size-dependent T_1 relaxation properties of MnO NPs were investigated by Hyeon and co-workers,[69] demonstrating higher T_1 signal enhancement for smaller MnO NPs than larger ones (Fig. 4a and b). The interaction between proton spins and surface Mn^{2+} ions on NPs is regarded as the main dipolar interaction responsible for their relaxation properties. Clear T_1-weighted MR images of the brain, liver, kidney, and spinal cord with a fine anatomical structure were obtained after administration of MnO NPs. Since MnO NPs spontaneously get oxidized to Mn_3O_4 NPs in air,[68] An *et al.* reported measurements of T_1 and T_2 relaxation of spherical and tetrahedral Mn_3O_4 NPs with varied uniform sizes.[132] In agreement with the previous results, the r_1 value increased as the size of Mn_3O_4 NPs decreased for both spherical (Fig. 4c) and tetrahedral NPs (Fig. 4d), and 3 nm-sized spherical NPs exhibited the highest r_1 value of 2.38 mM^{-1} s^{-1}, again indicating that higher surface-to-volume ratios lead to higher relaxivity of ultrasmall NPs.

To further increase surface-to-volume ratio, Mn-based NPs were etched into hollow structures by selectively removing the core MnO phase from the Mn_3O_4 shell phase, thus exposing more active Mn^{2+} ions to water protons.[68] As a result, the hollow nanostructure

with a larger water-accessible surface area possessed a much higher r_1 value of 1.42 mM^{-1} s^{-1} compared to the solid ones (r_1 = 0.21 mM^{-1} s^{-1}) at 3.0 T. Such hollow structures could be used as a drug delivery system with marked MRI contrast enhancement for the monitoring of drug release.[139,140]

3.1.3 Fe-based contrast agents—Iron oxide NPs are generally regarded to be safer than Gd- or Mn-based CAs because iron is essential in the human body, mostly stored as ferritin in the blood. Fe^{3+} has 5 unpaired electrons (J = 5/2, S = 5/2, L = 0), the same as Mn^{2+}, making Fe^{3+} a promising candidate for T_1 CAs.[136,141-143] Small-sized iron oxide NPs show enhanced T_1 contrast effects due to the existence of a large number of Fe^{3+} ions on the surface, suppressing T_2 relaxation by their small magnetic moment. The magnetic properties and r_1 values of various small-sized iron oxide NPs from 1.5 to 12 nm have been investigated (Fig. 5a).[135] By canting the most surface spins (around 93.6%), 2.2 nm-sized iron oxide NPs with low magnetic moments exhibited a relatively high r_1 value of 4.78 mM^{-1} s^{-1}, while the r_1 values of 12 nm NPs (nearly 38.6% of spins were canted, Fig. 5b) decreased to 2.37 mM^{-1} s^{-1} (Fig. 5c). This phenomenon was further verified in cellular studies, in which significant T_1 signal enhancement for 3 nm-sized NPs and attenuated T_1 signal for cells incubated with 12 nm-sized iron oxide NPs were found (Fig. 5d). Another study from Zhang *et al.* also indicated similar size-dependences of r_1 values based on ultra-small $MnFe_2O_4$ NPs.[136] Recently, exceedingly small iron oxide NPs with a hydrodynamic size of 4.7 nm, consisting of approximately 3 nm inorganic cores and about 1 nm organic hydrophilic shell, were reported to have high T_1 relaxivity (r_1 = 5.2 mM^{-1} s^{-1} at 1.5 T).[142] Excreted mostly within the first 2.5 h through the urine, the exceedingly small iron oxide NPs have been successfully applied for high-performance magnetic resonance angiography (MRA) imaging (Fig. 5e and f). Strong positive contrast from both the heart and blood vessels has been found, which decreased over time, while the signal from the bladder increased, indicating renal clearance.

Importantly, iron oxide NPs are also widely used as T_2 CAs, where the magnetic moment of these NPs decreases rapidly as the size decreases due to reduced magnetic anisotropy and spin disordering on the surface of NPs.[30,144] The size-dependence of T_2 contrast has been extensively investigated both theoretically and experimentally. Theoretically, two different regimes are predicted. The first is called the “motional averaging regime” (MAR) that describes T_2 relaxation for relatively small iron oxide NPs,[104] where water diffusion near NPs occurs on a much faster timescale than the resonance frequency shift, resulting in increased r_2 values with increasing NP size. However, this theory breaks down for larger NPs because the induced surrounding perturbing field around larger NPs is much stronger, and proton diffusion becomes a nondominant factor for signal decay. Therefore, the relaxation rate is independent of diffusion and does not significantly increase with further increase in size of NPs. This process is termed the “static dephasing regime” (SDR), first introduced by Yablonskiy and Haacke.[145] Importantly, this tendency has been validated on NPs of varied sizes synthesized by many different groups.

Generally, small iron oxide NPs synthesized by various research groups are in the MAR, where larger NPs possess higher magnetization and therefore larger r_2 values. For example, such size effects on T_2 contrast have been reported by Cheon and co-workers,[79] using small

and size-controlled Fe_3O_4 NPs (Fig. 6a), where the variation of NPs size from 4 to 6, 9, and 12 nm resulted in r_2 values of 78, 106, 130, and 218 mM^{-1} s^{-1}, respectively (Fig. 6b–d). Similar size effect on relaxation rates has also been reported by many other research groups.[80,83,105,146-149] Importantly, this size effect is a universal phenomenon, which is not limited to spherical NPs. For example, octapod iron oxide NPs with average edge lengths of 30 nm exhibited a large r_2 value of 679.25 mM^{-1} s^{-1}, almost three times higher than that of the NPs of 20 nm in edge lengths.[137] However, according to the SDR theory, the r_2 value reaches a plateau as the size continues to increase. It has been reported by Chen and co-workers that the size effect became less significant for single iron oxide NPs of 50 nm (Fig. 6e).[138] They found that r_2 values increased rapidly from 173.37 to 203.86 and 239.98 mM^{-1} s^{-1} at 7 T, when the particle size increased from 8 to 23 and 37 nm, respectively (Fig. 6f), but r_2 value was only slightly higher at 248.89 mM^{-1} s^{-1} for 65 nm-sized iron oxide NPs (Fig. 6g). This SDR theory has also been experimentally verified in cells loaded with iron oxide NPs,[150] as well as in an induced clustering process.[151]

3.1.4 Dy- or Ho-based contrast agents—Ultra-high field MRI, the future of next-generation MRI scanners, brings not only new opportunities for biomedical research, but also great challenges in developing exogenous CAs, since most currently used CAs are only suitable at relatively lowmagnetic field strengths (*e.g.*, 1.5 T or 3.0 T) but are inefficient at higher magnetic field strengths (*e.g.*, 7.0 T). Dysprosium (Dy^{3+}) and holmium (Ho^{3+}) are promising candidates for imaging in an ultra-high magnetic field due to their relatively short electronic relaxation time (~10^{-13} s) and large magnetic moment (~10.6 μ_B).[71] The size-dependent properties of $NaDyF_4$ NPs under ultra-high magnetic fields were first reported by van Veggle and co-workers,[19] demonstrating that T_2 contrast was enhanced with increasing NP size and magnetic field strength (Fig. 7b and c), while r_1 value remained almost unchanged (Fig. 7a).

In a follow-up study, van Veggle and co-workers investigated in detail the involved relaxation mechanisms of $NaDyF_4$ and $NaHoF_4$ NPs in the range of 9–40 nm based on the outer sphere theory (Fig. 7d).[20] The larger particle had a larger volume fraction, and a three-fold increase in core size resulted in r_2 values that were 30 times larger. Further theoretical simulation results showed that Curie contribution became predominant under an increasing magnetic field. Recently, we have reported the size effect of $NaHoF_4$ NPs on magnetic relaxation (Fig. 7e).[21] Both experimental and theoretical findings revealed that Curie contribution to contrast enhancement was the principal mechanism when particle size was smaller than 7 nm (Fig. 7f and g), as the $\varphi(\tau_D)$ value from Curie relaxation remarkably decreased with increasing diffusion correlation time (τ_D) from 1 ns (3 nm $NaHoF_4$) to 5 ns (7 nm $NaHoF_4$). The $\varphi(\tau_D)$ value then slightly decreased as τ_D became larger, explaining the opposite change of r_2 values that was observed when NP size was less than 7.4 nm. As the size of NPs increased to 13 nm and 29 nm, the contribution of dipolar mechanism could not be neglected, and all relevant mechanisms mentioned above contributed to MRI contrast enhancement.

3.2 Surface effects

Apart from the size effect on MRI relaxation, surface properties of NPs also play an important role in MRI contrast enhancement based on interaction between NPs and water molecules, which happens primarily on the surface of NPs. Individual contributions from the inner sphere, secondary sphere, and outer sphere depends on the CA's structure and composition, which can be regulated by surface modifications of tuned composition and thicknesses. Most NPs developed for *in vivo* MRI applications could be stabilized and functionalized with coating materials such as organic surface ligands, dense or mesoporous silica shells, or an inorganic nanolayer (*e.g.*, Fe_xO_y or $NaGdF_4$ layers). These modifications, here termed surface effects, can in turn impact the relaxation of water protons in various configurations, such as hydration, hydrogen binding, and diffusion. For T_1 CAs, surface effects can enhance proximity of water to center paramagnetic ions by tuning the distance of water protons to the NP surface, generating greater contrast than small-molecule CAs alone. Such a process depends on the species, chain length, density, and functional group of organic ligands, as well as the thickness of silica shells or inorganic nanolayers. For T_2 CAs, proper surface modification of magnetic NPs will impact intrinsic surface spin disordering, increase inhomogeneity in the local magnetic field, or induce much stronger magnetization, leading to improvement in T_2 contrast effects.

3.2.1 Organic surface ligands—Organic surface ligands are critical for the synthesis of NPs, not only for controllable growth during synthesis but also for ensuring their biocompatibility for *in vivo* application. An early study by Lee *et al.* suggested that different types of organic surface moieties greatly impacted T_1 contrast enhancement.[60] Organic ligands including mercaptosuccinic acid (MSA), poly(maleic anhydride-*alt*-1-octadecene) (PMAO), PMAO–PEG, and Pluronic PF127 were capped on MnO NPs. The MnO@MSA exhibited the largest r_1 values of 2.55 mM^{-1} s^{-1} at pH 7.4 and 6.94mM^{-1} s^{-1} at pH 5.0 among all the coatings, indicating that r_1 relaxivity of the NPs depended on the surface ligands.

Furthermore, the addition of polyethylene glycol (PEG) to the surface (*i.e.*, PEGylation) of NPs has been widely applied to improve biocompatibility of NPs, prolong *in vivo* circulation, and reduce the capture by the reticuloendothelial system (RES).[152-155] Recently, Johnson *et al.* reported a compact micellization strategy that could achieve ultra-high r_1 values (around 80 mM^{-1} s^{-1} at 1.4 T), about 25 times higher than that of clinically used Gd^{3+} chelates, by regulating the surface ligands (Fig. 8a–c).[39] The compactly packed PEGylated lipids would bring the water protons closer to the surface of $NaGdF_4$ NPs and thus lead to enhanced relaxivity. They also found that the relaxivity was independent of outer PEG chain length (Fig. 8d and e), whereas increasing the inner core $NaGdF^4$ size resulted in lowered relaxivity values (Fig. 8f and g). Two important criteria to achieve ultra-high relaxivity with Gd^{3+}-based NPs were proposed: (i) extremely small core NPs (<5 nm) and (ii) surface coating strategies that can render compact and individually stabilized NPs in water.

After surface PEGylation of ultra-small $NaGdF_4$ nanodots, our group further conjugated DTPA on the surface of NPs to capture potentially released Gd^{3+} ions, effectively preventing

their liberation.[40] The Gd^{3+} ions captured by DTPA could directly interact with water protons to further enhance relaxivity. Recently, Yan and co-workers presented another simple strategy to improve r_1 values by taking advantage of surface ligands' strong interaction with water protons.[36] $NaGdF_4$ NPs coated with poly(acrylic acid) (PAA) exhibited largely enhanced r_1 values compared to those coated by polyethylenimine (PEI) or PEG (Fig. 8h), which resulted from the strong hydrogen-bonding capacity of PAA to water molecules according to their theoretical calculation (Fig. 8i).

By rationally designing the functional group of surface ligands, the transverse r_2 value can also be regulated for iron oxide NPs. Zeng *et al.* reported the surface modification of PEG2000 ligands with three different functional groups: diphosphate (DP-PEG), hydroxamate (HX-PEG), and catechol (CC-PEG) on 3.6 nm and 10.9 nm Fe_3O_4 NPs (Fig. 9a).[149] The r_2 values increased with increasing sizes for all three ligand-modified Fe_3O_4 NPs, and the HX- or CC-PEG modified NPs showed much higher r_2 values than the unconjugated functional group of DP-PEG for both sized Fe_3O_4 NPs (Fig. 9b), while the r_1 value only changed slightly with different anchored groups and NP sizes (Fig. 9c). The π–π conjugation and p–π conjugation from the CC and HX groups were believed to create increased inhomogeneity in the local magnetic field around the underlying Fe_3O_4 NPs when compared to the unconjugated DP group (which has no π–π or p–π conjugation), which effectively accelerated transverse relaxation of the water protons nearby.

Besides the surface groups, the ligand species and the methods of modification also affect T_2 contrast enhancement. The species effects of surface ligands on magnetic properties were verified by Duan *et al.* by coating ultra-small Fe_3O_4 NPs with different levels of hydrophilic ligands including hyperbranched PEI, PEG grafted PEI (PEG-*g*-PEI), and poly(maleic acid)-octadecene (PMO).[148] The hydrophilicity of surface ligands was found to greatly impact the intrinsic surface spin disordering of NPs for water proton relaxation, where the most hydrophilic PEI coated Fe_3O_4 NPs showed the highest r_2 value, nearly three times higher than that of the least hydrophilic PMO-coated NPs. Among different methods for surface modification of $MnFe_2O_4$ NPs such as ligand exchange, encapsulation with polymer shells, and embedding them into micelles (Fig. 9d), embedding NPs into lipid micelles was found to be the most efficient method for greatly enhancing r_2 relaxation.[147] The larger-sized core inside lipid micelles and the contribution from dephasing of proton spins of the lipid molecules due to high viscosity of these molecules were considered to be responsible for this phenomenon.

The accessibility of water molecules to the magnetic core of NPs depends on the thickness of surface ligands, which can influence T_2 relaxation of NPs. Tromsdorf *et al.* found that increasing PEG chain length from PEG350 to PEG550 on the surface of Fe_3O_4 NPs led to decreased r_2 and almost unchanged r_1 values due to aggregation of NPs.[141] However, slight changes were found for both r_1 and r_2 values when PEG chain length was increased from 550 to 2000. Another report by Tong *et al.* indicated that Fe_3O_4 NPs had a critical PEG ligand size, at which the r_2 value changed dramatically.[105] The coating thickness could be well controlled by varying the size of DSPE–PEG from 500 Da to 5000 Da (Fig. 9e). Interestingly, the r_2 value of 14 nm Fe_3O_4 NPs increased by 2.5-fold when PEG molecular weight decreased from5000 to 1000 Da (Fig. 9f). It was suggested that 14 nm iron oxide

NPs and PEG1000 surface modification was the optimal combination of core size and coating thickness according to T_2 relaxivity on a per-particle basis (Fig. 9g). However, r_2 values did not increase further when PEG size decreased to 750 and 550 Da. Such effects of PEG chain length on T_2 relaxivity can be partly attributed to changes in the shell/core ratio, *i.e.*, L/r in eqn (3), under the assumption that the coating was water impermeable.

3.2.2 Surface silica coatings—The growth of a dense or mesoporous silica shell on the surface of MRI CAs has been a commonly used strategy since silica exhibits excellent biocompatibility, and the active surface or pore volume of the shells can be used for conjugating or loading biological molecules, functional particles, and therapeutic agents.[156-158] Our group extensively investigated the effect of both dense ($dSiO_2$) and mesoporous ($mSiO_2$) silica shells and their thickness on the MRI relaxation of Gd^{3+}-based upconversion nanoparticles (UCNPs) (Fig. 10a).[159] The thicknesses of $dSiO_2$ and $mSiO_2$ shell could be well controlled and uniformly coated on each particle (Fig. 10b and c). It was found that both r_1 and r_2 values were independent of thickness of $mSiO_2$ shell, the thickness of which could be readily controlled from 11.1 nm to 23.4 nm. The dominant outer sphere mechanism determined by the translational diffusion of water molecules was thought to be responsible for this phenomenon, and the diffusion of water molecules in the mesoporous channels was not affected by the increased thickness of the $mSiO_2$ shell (Fig. 10d). However, the diffusion of water molecules in the $dSiO_2$ shell, in which large pore channels did not exist, became much more restricted by thicker $dSiO_2$ shells, leading to longer translational diffusion time and thus larger r_1 and r_2 values. Therefore, the r_1 value of UCNPs@$dSiO_2$ increased from4.03mM^{-1} s^{-1} to 9.7mM^{-1} s^{-1} as the thickness of $dSiO_2$ shell increased from 2.6 nm to 16.9 nm, while r_2 values almost doubled (from 57.58 mM^{-1} s^{-1} to 102.08 mM^{-1} s^{-1}, Fig. 10e).

In another study, both $mSiO_2$ and $dSiO_2$ shells were used to coat the surface of MnO NPs.[160] With these modifications, the r_1 value decreased substantially from 0.17 mM^{-1} s^{-1} for MnO NPs to 0.07 mM^{-1} s^{-1} for MnO@$dSiO_2$. For MnO@$mSiO_2$ nanostructures, the r_1 value was similar to MnO NPs (0.16 mM^{-1} s^{-1}), which was attributed to the existence of worm-like nanochannels in these NPs, where increased water exchange rates could be achieved. Similar results were also reported by Kim *et al.*, who found that $mSiO_2$-coated MnO NPs showed a much higher r_1 value of 0.65 mM^{-1} s^{-1} than those of $dSiO_2$-coated NPs (r_1 = 0.08mM^{-1} s^{-1}) and PEGlyated MnO NPs (r_1 = 0.11mM^{-1} s^{-1}). The r_1 value could be further increased to 0.99 mM^{-1} s^{-1} after acid etching of MnO NPs to generate a hollow nanostructure (*i.e.*, HMnO@$mSiO_2$) (Fig. 10f and g).[62] Such a hollow structure allowed more interior Mn^{2+} ions to interact with water molecules on the inner surface, resulting in a significantly higher r_1 value than that of MnO NPs encapsulated with PEG phospholipids. [69] Therefore, intracranial transplantation of HMnO@ $mSiO_2$-labeled mesenchymal stem cells could be monitored by serial MRI over 14 days (Fig. 10h). Among a number of surface modifications strategies of NPs with organic ligands and silica, Lee *et al.* found that silica-coated MnO exhibited the highest stability at neutral pH and the slowest dissolution rate when dispersed in acetate buffer solutions and showed continuous contrast enhancement in the rat brain.[60]

3.2.3 Inorganic surface nanolayers—Coating an inorganic nanolayer (*e.g.*, Fe_2O_3, Fe_3O_4, $NaGdF_4$, and so forth) on the surface of NPs to induce stronger magnetization and ensure adequate exposure to water molecules nearby is an attractive strategy to obtain high-relaxivity T_2 or T_1 CAs. MR relaxation enhancement effects of γ-Fe_2O_3 nanolayers were first reported by Xu and co-workers based on core/shell, yolk/shell, or hollow structures (Fig. 11a–d).[77] Field-dependent magnetization measurements showed that all these NPs were superparamagnetic (Fig. 11e), and the saturated magnetization (M_s) of the γ-Fe_2O_3 hollow nanostructure was the highest among these nanostructures (about 50.8 emu g^{-1}). Additionally, both the growth of a 5 nmFe_xO_y layer and self-assembly of ultra-small Fe_3O_4 on the surface of UCNPs generated much higher r_2 values than conventional iron oxide NPs.[161,162] Cheong *et al.* synthesized iron/iron oxide core/shell (Fe@Fe_3O_4) NPs by oxidizing the surface of iron nanocrystals in the air.[163] These core/shell Fe@Fe_3O_4 NPs had a r_2 value of 324 mM^{-1} s^{-1}, more than twice that of Fe_3O_4 NPs (145 mM^{-1} s^{-1}, Fig. 11h and i). Such an increase in r_2 value was attributed to the presence of a single-crystal iron core, which can induce much stronger magnetization than Fe_3O_4 NPs.

The coating of a $NaGdF_4$ layer is an intriguing approach not only to suppress surface quenching of UCNPs for enhanced luminescence emission but also to endow NPs with MRI capabilities, creating a dual-modality imaging system.[125,165,166] Results from different groups have suggested that the presence of Gd^{3+} ions on the surface of NPs might play a major role in accelerating relaxation, whereas the contribution from inner Gd^{3+} ions could be neglected; however, no direct evidence has been found to support this hypothesis.[46,48,49] To investigate this issue, our group designed Gd^{3+}-doped core NPs with multilayer coating of $NaYF_4$ and/or $NaGdF_4$.[164] The r_1 value was calculated to be 1.24 mM^{-1} s^{-1} for the core NPs, which decreased to nearly zero (r_1 = 0.037 mM^{-1} s^{-1}) after coating a ~4 nm$NaYF_4$ layer on the core NPs, and recovered to 1.18 mM^{-1} s^{-1} after further coating with a $NaGdF_4$ layer, clearly indicating the different effects between the bulk and surface Gd^{3+} ions in shortening T_1 relaxation time.

To further validate the hypothesis that Gd^{3+} ions in the inner crystal lattice contributed little to longitudinal relaxivity, Gd^{3+}-free core NPs were coated with a $NaGdF_4$ layer of varied thicknesses (Fig. 12). With an increase in $NaGdF_4$ layer thickness from approximately 0.2 nm to 3.7 nm, r_1 values decreased gradually from 6.18 mM^{-1} s^{-1} to 2.18 mM^{-1} s^{-1}, confirming that the main contribution to shortening T_1 values was by surfacebound Gd^{3+} ions on the NPs. Subsequently, these $NaGdF_4$ coated UCNPs were applied as dual-targeted nanoprobes by conjugating angiopep-2 peptide to cross the blood–brain barrier and target brain tumors for MRI-aided preoperative diagnosis and intraoperative identification of brain tumors by upconversion luminescence in an animal model.[166]

3.3 Shape effects

The shape effects of NPs can be as important as the size and surface effects in determining the properties of nanomaterials. The unusual shapes of these NPs could potentially dictate their interactions with single cells or whole organisms.[167] Shape-dependent relaxivity of NP-based MRI CAs has been revealed by many different groups, where shape anisotropy of magnetic NPs or shape confinement of Gd^{3+}-based CAs can improve the relaxation of

nearby water molecules. Employing the highly controllable shape of spherical or cubic magnetic $CoFe_2O_4$ NPs, Song *et al.* found that shape was an important factor in determining coercivity of magnetic NPs due to the varying effects of surface anisotropy.[82] Very strong localized magnetic field inhomogeneity was produced by shape anisotropy, and the generated magnetic field strength was found to be dependent on the shape of magnetic NPs due to demagnetization effect.[168] Shape-dependent enhancement of r_2 values was also observed with superparamagnetic NPs.[80,81,137] For example, faceted irregular cobalt ferrite nanostructures showed increased r_2 values when compared to spherical NPs of similar volume.[81] Zhao *et al.* synthesized branched octapod-shaped iron oxide NPs (edge length of 30 nm, Fig. 13a) with an ultra-high r_2 relaxivity of ~679.3 mM^{-1} s^{-1},[137] which was a much more effective T_2 CA for small tumor detection than conventional spherical iron oxide NPs (Fig. 13d and e) because of their unique morphology and larger effective boundary radius (Fig. 13c). The significant enhancement was attributed to an increase in the effective radius of the magnetic core, a parameter that is impacted by shape anisotropy and directly affects r_2 values (Fig. 13b).[80,137]

Recently, Mohapatra *et al.* suggested that although spherical iron oxide NPs exhibited higher magnetization than iron oxide nanorods (NRs) of the same volume,[80] high relaxivity (r_2 = 608mM^{-1} s^{-1}) was obtained for 50 nm NRs (Fig. 13g and h), while the relaxivity of the same volume of spherical NPs (the volume of a 50 nm NR was equivalent to that of a 16 nm NP) was only 297 mM^{-1} s^{-1}. This phenomenon was believed to be a result of the larger surface area of the anisotropic morphology for NRs. Using the software Comsol Multiphysics, the induced local field inhomogeneity surrounding the 50 nmNRs was calculated to be significantly stronger than that induced by 16 nmNPs (Fig. 13g and h). The higher outer sphere diameter of rod-shaped NPs resulted in a stronger local magnetic inhomogeneity with a larger number of water protons experiencing rapid dephasing, which gave a higher r_2 value. On the other hand, spherical NPs exhibited a smaller volume of magnetic field variation. Therefore, water protons diffused slowly and thus dephased slowly, resulting in a much lower r_2 value than NRs of equivalent volume (Fig. 13i).[80]

Importantly, the shape effects of NPs on r_2 values cannot be translated to r_1 values because mechanisms for enhancements in r_2 and r_1 are different. An early study from Hyeon and co-workers demonstrated the significant effects of shape on r_1 values using spherical and tetrahedral Mn_3O_4 NPs.[132] Recently, Rotz *et al.* described the surface conjugation of DNA–Gd onto gold nanostars and nanospheres[95] and found that DNA–Gd@stars exhibited remarkable r_1 values up to 98 mM^{-1} s^{-1}, much higher than those of DNA–Gd@spheres, where r_1 values were 25 times larger than FDA-approved Gd chelates at 25 °C (Fig. 14a and b). Nuclear magnetic relaxation dispersion (NMRD) analysis indicated that secondary-sphere relaxivity contributed significantly to the production of such an exceptionally high r_1 value of DNA–Gd@stars, while secondary-sphere enhancements were not observed for DNA–Gd@spheres (Fig. 14c). The shape of gold nanostars with hydrophilic microenvironment played a meaningful role in the sequestration of water molecules around the Gd^{3+} complexes, which facilitated longer access to secondarysphere water molecules and thereby generated greater contrast enhancement. Further studies from the same group reported that r_1 depended on the number of branches on the nanostars, as r_1 increased with increasing average number of branches (Fig. 14d).[94] Researches from many other groups

have also demonstrated that the shape of NPs can greatly impact their cellular uptake, biodistribution, clearance, and biocompatibility *in vivo*.[169-173] Thus, an in-depth understanding of the effects of shape on relaxation can enable the rational design of high-relaxivity CAs with outstanding performance for *in vivo* applications.

4. Strategies to achieve high relaxivity for MRI contrast enhancement

Size control, surface modifications (*e.g.*, organic surface ligands, silica shells, and inorganic nanolayers), and shape regulation at the nanoscale have been widely applied to regulate the behavior of CAs, resulting in largely accelerated relaxation for efficient T_1 or T_2 MRI contrast enhancement. A deep understanding of the involved nucleation, growth, and surface chemistry of NPs enables intelligent engineering of the key factors that affect relaxation, either independently or in combination. The development of such high-relaxivity CAs is crucial for molecular MRI applications such as early-stage disease detection,[174-176] gene expression monitoring,[177,178] drug release,[140,179-181] and cell tracking.[182-185] In addition to the traditionally investigated factors influencing the performance of CAs at the nanoscale, several novel strategies have been exploited to obtain high-relaxivity CAs, such as confining CAs in mesopores, doping with metal ions, self-assembly or disassembly, and so forth (Fig. 15).

4.1 Confinement in mesopores

The accessibility of water molecules to the paramagnetic center is highly important for the design of high-relaxivity CAs. Mesoporous silica nanoparticles (MSNs) provide an ideal platform for ready access of water molecules to the center due to their tunable pore structures and high surface areas. Dispersing CAs such as Gd^{3+} chelates,[90-92] MnO NPs,[61,64,139] and iron oxide NPs[143] into the mesopores of MSNs can efficiently prolong τ_R and thus greatly increase relaxivity. For example, Lin *et al.* loaded Gd–Si–DTPA complexes into the hexagon-ordered nanochannels (~2.4 nm diameter) of MSNs, obtaining extremely high r_1 values of 10.2 mM^{-1} s^{-1} at 9.4 T and 28.8 mM^{-1} s^{-1} at 3.0 T.[91] The geometrical confinements of Gd^{3+} chelates, gadofullerenes, and gadonanotubes within the porous structure of silicon microparticles (SiMPs) (Fig. 16a) were all reported by Ananta *et al.*,[186] demonstrating that such a strategy can successfully influence the paramagnetic behavior of Gd^{3+} ions, resulting in increased r_1 values. By prolonging τ_R and reducing the mobility of outer sphere water molecules, r_1 values about 4–50 times larger than their original values without SiMPs were obtained (Fig. 16b).

Recently, the use of such geometrical confinement for enhanced relaxivity was further confirmed by Gao and co-workers.[187] Ultrasmall Gd_2O_3 NPs with numerous coordinating water molecules were dispersed into worm-like mesoporous channels of MSNs, which, by increasing the tumbling time and creating a geometrically confined space, remarkably increased r_1 value from 14.93 mM^{-1} s^{-1} to 45.08 mM^{-1} s^{-1} at 0.5 T. (Fig. 16c). Thus, confinement of CAs in a porous structure offers a new and widely applicable strategy for strong T_1 contrast enhancement, where mesopores also hold the potential for drug loading and delivery for therapeutic applications.

As described above, loading small MnO or iron oxide NPs within the mesopores of MSNs was demonstrated to be more beneficial for relaxation enhancement than traditional silicacoated structures because such coating layers shielded the surface paramagnetic centers from interaction with the water molecules.[139,143] To further enhance the r_1 value of MnO NPs to exceed that of clinical Gd^{3+} chelates (*e.g.* Magnevist, r_1 = ~3.4 mM^{-1} s^{-1}), we loaded small MnO NPs into hollow mesoporous silica nanoparticles (HMSNs) *via* an *in situ* redox reaction to further facilitate the interaction between manganese paramagnetic centers and water protons (Fig. 16d).[61] Using this strategy, we were able to obtain a maximum r_1 value of 8.81 mM^{-1} s^{-1}, which is more than twice that of commercial Gd^{3+} chelates (Fig. 16e). In addition, the well-defined mesoporosity of HMSNs can enable efficient encapsulation of photosensitizers (*i.e.*, protoporphyrin) for therapeutic purposes, as well as further confinement of paramagnetic Mn ions based on metalloporphyrin chelating chemistry.[188] This mesoporous structure endowed these intriguing sensitizers with remarkably enhanced MRI performance (r_1 = 9.43 mM^{-1} s^{-1}).

By a facile but efficient physical-vapor-infiltration method, ultra-small iron oxide NPs have also been confined to the mesoporous networks of MSNs.[143] In particular, the highly dispersed iron species in the mesoporous channels can be used as anchoring sites for anti-cancer drugs, such that gradual exposure of these iron paramagnetic centers along with controllable drug release from the mesopores enables monitoring of drug release *in vivo* through synchronously intensified MRI contrast. In another recent report, Zhang *et al.* incorporated both $GdPO_4$ and g-Fe_2O_3 NPs in ordered mesoporous carbon composites, which exhibited satisfactory r_1 and r_2 values of 2.7 and 183.7 mM^{-1} s^{-1}, respectively.[189]

4.2 Metal alloying and metal ion doping

The MRI performance of magnetic NPs is strongly dependent on their magnetic characteristics. Metal alloy-based NPs such as FeCo and FePt NPs are another class of CAs,[77,146,190-194] which possess magnetic spins that align in parallel to the external magnetic field, resulting in typically higher magnetic moments than traditional ferromagnetic NPs. For example, the magnetic moment of FeCo alloys is approximately 2.4 μ_B per magnetic atom, while that of Fe_3O_4 NPs is approximately 1.3 μ_B.[146] These FeCo alloys have a comparably high M_s of 215 emu per gram of metal when coated with a graphite shell, leading to an exceptionally high r_2 value of 644 mM^{-1} s^{-1}, much larger than that of conventional Fe_3O_4 NPs (usually about 100 mM^{-1} s^{-1}). High X-ray absorption of Pt (6.95 cm^2 g^{-1} at 50 keV) makes FePt alloy NPs promising candidates for MRI/CT dual-modality CAs.[194] By conjugating FePt NPs with an antibody targeting Her2/neu, *in vivo* dual-modality imaging was achieved in cancer lesions in an animal model. Recently, it was reported that FePt NPs could also be used as an infrared-active nanoplatform for four imaging modalities (optical/photoacoustic/CT/MRI), which may allow for multiscale imaging from the cellular level to wholebody imaging.[192]

According to eqn (3), the r_2 value of magnetic NPs is proportional to their M_s. Thus, metal ion doping has been verified to be an effective method to engineer the magnetism of iron oxide NPs and obtain extremely high r_2 values, as investigated in detail by Cheon and co-workers.[84] They synthesized various types of MFe_2O_4 NPs in which Fe^{2+} ions can be

readily replaced by other transition-metal dopants M^{2+} where M = Mn, Ni, or Co. The magnetic moments per unit of $MnFe_2O_4$, $CoFe_2O_4$, and $NiFe_2O_4$ were estimated to be 5 μ_B, 3 μ_B, and 2 μ_B, respectively, leading to gradually decreasing M_s values from 110 emu per gram of metal for $MnFe_2O_4$ NPs to 85 emu per gram of metal for $NiFe_2O_4$ NPs (Fig. 17a). As a result, $MnFe_2O_4$ NPs exhibited the highest r_2 value of 358 mM^{-1} s^{-1}, two-fold higher than that of conventional iron oxide NPs. Such an enhancement is significant for clinical applications as the dosages of nanoparticulate CAs can potentially be decreased. By further co-doping Zn^{2+} and Mn^{2+} ions in $(Zn_xMn_{1-x})Fe_2O_4$ NPs, the same group obtained NPs that exhibited an extremely high magnetization value (175 emu g^{-1}) and provided the largest r_2 value (860 mM^{-1} s^{-1}) among the CAs reported to date (Fig. 17c).[83] In this study, it was also found that the magnetism was dependent on amount of metal ion doping and $x = 0.4$ doping of Zn^{2+} demonstrated the best contrast (Fig. 17b).

4.3 Self-assembly and disassembly

"Activatable" or "smart" nanoprobes with tunableMRI relaxivity through self-assembly or disassembly in the presence of certain pathophysiological parameters can serve as high-relaxivity CAs, resulting in enhanced detection sensitivity of MRI for specific molecular or biological events. For example, such a self-assembly strategy allows for small NPs to circulate in the blood pool over a prolonged time duration, which can then be triggered in the tumor to self-assemble into a large structure for enhanced MRI. The trigger may include many physiological characteristics, such as molecular interactions,[195] enzymes,[196] receptors,[197] and redox status.[198] On the other hand, the disassembly strategy utilizes the different tumor microenvironments to release CAs preconfined in NPs, also achieving amplified MRI contrast. Both strategies are highly versatile and useful as they could be potentially used to monitor *in vivo* biological processes of the tumor microenvironment and improve the accuracy of cancer diagnosis or monitoring the therapeutic efficacy.

4.3.1 Self-assembly—Liang and co-workers reported the controlled self-assembly of Gd^{3+}-based NPs through the condensation reaction between 1,2-aminothiol and 2-cyanobenzothiazole. [199] The probe was activated through disulfide reduction by tris(2-carboxyethyl)phosphine or glutathione (GSH) in cells and generated intermediate 1,2-aminothiol groups to react with the cyano groups on 2-cyanobenzothiazole, which results in selfassembly of large Gd^{3+} NPs with enhanced relaxivity. Presumably due to an increased rotational correlation time, a more than 2-fold increase in r_1 value was observed for the larger assembly when compared to its small molecule form of Gd^{3+} chelates. Through further optimization of self-assembly strategy by intermolecular macrocyclization chemistry, the same group obtained biothiol-specific Gd^{3+}-based CAs with amplified relaxivity after self-assembly, which were capable of detecting GSH concentrations with high sensitivity using MRI.[200] In addition to redoxactivatable self-assembly, Ye *et al.* reported novel caspase-3/7 activated Gd-based CAs, which could self-assemble into Gd^{3+} NPs upon reduction and activation by caspase-3/7, an important early biomarker for apoptosis.[201] Higher r_1 relaxivity and longer retention time in apoptotic tumors were found with such self-assembling CAs, suggesting the potential for MRI of *in vivo* enzyme activity.

Self-assembly of small magnetic NPs into nanoclusters to increase effective magnetic size is also a widely used strategy for enhancing their magnetic properties and thus obtaining a higher r_2 value. Using charge compensation and electrostatic adsorption between oppositely charged moieties, Berret *et al.* assembled 6.3 nm iron oxide NPs into larger nanoclusters, resulting in remarkably increased r_2 values from 39 mM^{-1} s^{-1} for single NPs to 71 mM^{-1} s^{-1} for 70 nm nanoclusters and 162 mM^{-1} s^{-1} for 170 nm nanoclusters.[202] The detection sensitivity of MRI using these NPs was thus substantially improved. A similar effect was also reported by Ai *et al.* in their first proofof- concept study regarding clustering of monodispersed iron oxide NPs inside the core of polymeric micelles.[203] When compared to single core nanoparticles, multi-core nanoclusters with an average core size of 50 nm (self-assembled from 13 nm iron oxide NPs) provided much higher M_s values and subsequently exhibited higher performance in MRI contrast enhancement.[204]

Although larger sized iron oxide NPs present enhanced magnetic properties for MRI contrast enhancement, an ideal scenario is the self-assembly of small iron oxide NPs into larger nanostructures at the target sites (*e.g.*, tumor) for substantially amplified relaxation, since smaller NPs (below renal clearance threshold of approximately 10 nm) exhibit longer blood circulation half-life and hence are cleared more slowly from the blood pool than their larger counterparts. Mao and co-workers reported that ultrafine iron oxide NPs (~3.5 nm) with high T_1 relaxivity exhibited prolonged *in vivo* circulation life time and could be self-assembled or clustered into larger ones in the tumor, thereby switching from bright T_1 contrast to dark T_2 contrast in MRI.[205] In another report, two complementary iron oxide NPs that were linked to a peptide substrate for enzymatic cleavage and a functional group (azide or alkyne) for click reaction[196] were able to self-assemble into a larger nanocluster network in the presence of matrix metalloproteinase enzymes, leading to approximately 160% enhancement of T_2 signal intensity.

Recently, Liang and co-workers reported a caspase-3/7- instructed biorthogonal cyclization to self-assemble Fe_3O_4@1 NPs in apoptotic cells and tumors for greatly enhanced T_2 MRI (Fig. 18a).[197] Caspase-3/7-mediated self-assembly of Fe_3O_4@1 NPs (r_2 = 185 mM^{-1} s^{-1}) induced an approximately 65% increase of r_2 value when compared to the control group (r_2 = 112 mM^{-1} s^{-1}) (Fig. 18b). More importantly, *in vivo* MRI revealed that Fe_3O_4@1 NPs provided specific T_2 enhanced contrast in apoptotic tumors, whereas the control Fe_3O_4@1-Scr NPs showed no contrast enhancement (Fig. 18c). In another recent study, Gao and co-workers synthesized Fe_3O_4 NPs modified with a responsive peptide sequence,[198] which enabled GSH-triggered self-assembly of Fe_3O_4 NPs within the tumor microenvironment and the formation of aggregates through inter-particle cross-linking reactions (Fig. 18d and e). Both *in vitro* and *in vivo* experiments demonstrated that such self-assembly strategies substantially enhanced MRI performance (Fig. 18f).

4.3.2 Disassembly—In general, disassembly strategies switch the relaxivity of CAs from “off” to “on” after responding to pathophysiological parameters such as low pH value and high GSH concentration within the tumor, thereby maximizing the signal from region-of-interest and minimizing the signal from background tissues to improve specificity and sensitivity of CAs. For example, Viger *et al.* encapsulated a large number of ultra-small Gd_2O_3 NPs in biodegradable polymer capsules, which showed extremely weak MRI contrast

due to effective silencing of both inner and outer sphere relaxation.[131] The r_1 of the ultra-small Gd_2O_3 NPs could be recovered after disassembling the large capsules under acidic conditions and/or in the presence of H_2O_2, which are both characteristic of many diseases such as cancer (Fig. 19a). In this study, encapsulation of ultra-small Gd_2O_3 NPs within pH-responsive polymer particles resulted in deactivation of their contrast enhancement at pH 7.4. However, burst degradation was observed within 1 min at pH 6.5 (approximately the extracellular pH of diseased tissue), leading to an instantaneous 4.2-fold increase of r_1 value, which remained constant thereafter (Fig. 19b). This concept was also verified using a peroxide-degradable polymer for encapsulation of ultra-small Gd_2O_3 NPs, indicating a general strategy of disassembly (Fig. 19c).[131] A redox-modulated disassembly of Gd^{3+}-based nanosystem was developed by Martinelli *et al.*[206] The disassembly was achieved *via* the cleavage of S–S bridges in response to reducing environments, leading to the release of Gd^{3+} complexes and a subsequent significant change in relaxivity.

Similar to the above-mentioned strategies used for Gd-based NPs, the release of Mn^{2+} from the disassembled matrix at lowpH sites was also employed to obtain high-relaxivity CAs for pH-responsive MRI.[61,63] For example, Kim *et al.* reported core–shell Fe_3O_4@Mn_3O_4 NPs, where Mn^{2+} ions released from the Mn_3O_4 shell under reducing conditions allowed Fe_3O_4 NPs to interact with water protons, thereby enhancing contrast of both T_1 and T_2-weighted MRI.[207] By confining Mn^{2+} within pH-sensitive calcium phosphate NPs (PEGMnCaP NPs, Fig. 20a), Mi *et al.* found a remarkable increase of r_1 from 4.73 mM^{-1} s^{-1} to 19.96 mM^{-1} s^{-1} after exposure to acidic environments simulating intratumoral pH, wherein the pH-sensitive CaP was disassembled (Fig. 20b).[52] The enhanced MRI signal by the dissembled CaP matrix and released Mn^{2+} was attributed to the increase in relaxivity after binding of Mn^{2+} with the protein. Such Mn^{2+}-triggered signal amplification could be further used for the precise imaging of tumors. After intravenous injection of PEGMnCaP NPs, enhanced MRI signal in tumor areas could be clearly visualized within 6 h after injection. Such a release of Mn^{2+} from the nanocomposites allowed these NPs to sensitively detect millimeter-sized metastatic tumors in the liver of mice, which were otherwise invisible (Fig. 20c). The signal of the gallbladder gradually increased due to hepatic clearance of PEGMnCaP. As hypoxic regions in tumors usually exhibit a lower local pH than surrounding tissues, the contrast in hypoxic regions was 20–30% higher than that in normally oxygenated regions within the tumors after intravenous injection of PEGMnCaP NPs (Fig. 20d and e).

By doping Mn^{2+} ions into HMSN (Mn–HMSNs), we have recently reported a strategy called “manganese extraction” to promote the disassembly of Mn–HMSNs and enhance MRI contrast (Fig. 20f).[208] Such a Mn^{2+} doping approach enabled accelerated disassembly of Mn–HMSNs in either mildly acidic or reducing microenvironments by breaking the Mn–O bond and subsequently triggering “manganese extraction,” which further accelerated breakage of Si–O–Si bonds in the framework and biodegradation of HMSNs (Fig. 20g and h). Such a fast disassembly of Mn–HMSNs enhanced the interaction probability of Mn paramagnetic centers with water molecules, allowing pH- and GSH-responsive MRI to be realized (Fig. 20i and j). The disassembly of Mn–HMSNs also accelerated the release of anticancer drugs to obtain tumor-sensitive theranostic functions.

4.4 Other strategies

Valency change—In principle, any physical or chemicalmethod to change the interaction between CAs and water molecules such as the number of bound water molecules (q), rotational correlation time (τ_R), and water residence time (τ_M) of T_1 CAs or to enhancemagnetic properties of T_2 CAs will undoubtedly result in enhanced MRI relaxivity of CAs. One major strategy for MRI contrast enhancement focuses on valency changes of ions, which has been widely applied through using redox-activated chemical exchange saturation transfer (CEST) agents that can be detected by MRI.[85,86,209] As previously discussed, the valency of ions affects electron spin that in turn influences relaxation of water protons. Owing to its pH- and redox-responsive properties, MnO_2 can be reduced to Mn_{2+} by GSH or H_2O_2/H^{+}.[51,53,210] For example, Chu *et al.* reported that MnO_2 nanosheets could serve as highly effective generators to trigger self-assembly of photosensitizers (sinoporphyrin sodium, DVDMS) after reduction by GSH and H_2O_2 (Fig. 21a).[211] Such processes could be monitored by *in vitro* and *in vivo* MRI (Fig. 21b and c), which was validated by TEM imaging of *ex vivo* tumor tissues (Fig. 21d).

Research from our group also suggested that MnO_2 nanosheets could generate oxygen to overcome the hypoxic environment of tumors by reacting with H_2O^2 [53] and the released Mn^{2+} could be used for pH-responsive MRI.[55] Zhao *et al.* designed a redox-responsive MnO_2 nanosheet, in which manganese atoms were coordinated in an octahedral geometry to six oxygen atoms that prevented direct contact with the aqueous environment, therefore making no contributions to the alteration of relaxation of water protons.[54] Intracellular GSH could then reduce endocytosed MnO_2 nanosheets, generating numerous Mn^{2+} ions for MRI with greatly enhanced r_1 and r_2 values.

Oxygen vacancy—To date, the strategy of increasing the number of bound water molecules has not been employed in inorganic Gd^{3+}-based NPs. Recently, we introduced oxygen vacancy into Gd^{3+}-based NPs by designing a novel Gd^{3+}-doped tungsten bronze (termed as PEG-Na_xGdWO_3 nanorods).[37] For the first time, controllable oxygen vacancies in inorganic nanosized CAs were generated for accelerated proton relaxation, favorably resulting in a substantially enhanced r_1 value due to the oxygen vacancies' natural affinity to oxygen atoms in water molecules.[212] Such a strategy was validated with oxygen-deficient PEG-Na_xGdWO_3 nanorods, which exhibited extraordinarily high r_1 values up to 80 mM^{-1} s^{-1} at 0.7 T and 32.1 mM^{-1} s^{-1} on a clinical 3.0 T scanner (Fig. 21e and f), offering excellent blood pool imaging and tumor diagnosis capabilities at a low CA dosage. NMRD profiles indicated that r_1 value was apparently increased by changes in the distribution of the number of bound water molecules (q) either through secondary- or outer-sphere effects (Fig. 21g).

Distance regulation—Recently, Choi *et al.* have introduced a distance-dependent magnetic resonance tuning systembased on the interaction between a superparamagnetic 'quencher' and a paramagnetic 'enhancer', where T_1 signal was tuned "on" or "off" depending on separation distance between the enhancer and quencher.[213] As the enhancer moved far away from the quencher ($d_1 > d_c$, where d_c is the critical separation distance), the electron spin fluctuation of the enhancer accelerated water proton relaxation, resulting in a

stronger T_1 signal ("on" state); however, when the enhancer and quencher were in close proximity to one another ($d_2 < d_c$), the resulting spin fluctuation became too slow to induce effective water proton relaxation, resulting in a low T_1 signal "off" state (Fig. 22a). The feasibility of this strategy was demonstrated through the control of thickness of SiO_2 shell, thereby separating the enhancer and quencher from 18 to 2 nm (Fig. 22b). The d_c was set to 7 nm, where the T_1 relaxivity quenching efficiency was 50% (Fig. 22c). Measurements from X-band electron paramagnetic resonance and NMRD profiles revealed distance-dependent values of correlation time (τ_c) and T_{1e} (for details, please see eqn (2)), indicating that the enhancer electron spin fluctuation became slower as separation distance decreased. Furthermore, such a distance-dependent tuning effect of MRI signal was verified using three representative models of molecular interactions (*i.e.*, cleavage, binding, and folding/unfolding) *via* modular combinations of enhancers and quenchers though interactive linkers (Fig. 22d).

Tuning inhomogeneity—A novel strategy to greatly enhance r_2 relaxivity by tuning magnetic field inhomogeneity of iron oxide nanoclusters has been recently reported by Chen and co-workers.[214] Using both experimental validations and theoretical simulations, the group found that the clustering of iron oxide NPs could enhance local field inhomogeneity due to reduced field symmetry. Clusters of mixed 5 nm plus 15 nm iron oxide NPs exhibited a much higher r_2 value of 533.4mM^{-1} s^{-1}, when compared to clusters containing 5 nm NPs only (r_2 = 231.6 mM^{-1} s^{-1}) or 15 nm NPs only (r_2 = 358.3 mM^{-1} s^{-1}) (Fig. 23a), indicating the important roles of particle distribution and fraction in generating local field inhomogeneity. By artificially involving iron oxide NPs with heterogeneous geometries (*e.g.*, iron oxide cubes and plates to assemble clusters) (Fig. 23b and c), the levels of field inhomogeneity were further elevated when compared to iron oxide sphere clusters. The iron oxide cube clusters showed the highest r_2 value (589.3 mM^{-1} s^{-1}) due to the presence of spinpolarized cubes in nanoclusters (Fig. 23d). Landau–Lifshitz–Gilbert simulations confirmed their hypothesis (Fig. 23e and f), suggesting that regulating magnetic field inhomogeneity is a powerful way to establish correlations between magnetization and T_2 relaxivity of iron oxide NPs.

5. Summary and outlook

The design and fabrication of high-relaxivity and ultra-sensitive CAs for MRI provides not only a great challenge to overcome, but also provides great opportunities to make significant contributions in the biomedical field. The imaging performances of commercially available MRI CAs have been far from optimal, which necessitates the development of novel nanosized CAs with large enough contrast effects for highly sensitive detection of lesions. Undoubtedly, controllable synthesis and facile engineering of inorganic nanoparticulate CAs and their excellent *in vivo* behavior as imaging agents will greatly deepen our understanding and subsequent effective diagnosis and treatment of diseases.

This review article provides a comprehensive summary of methods that have been investigated to construct highperformance CAs, including size control of Gd-, Mn-, Fe-, Dyand Ho-based NPs, surface modification with different ligands, coating of silica shells (dense or mesoporous shells) or inorganic nanolayers on NPs, and regulation of shape of

NPs for accelerated relaxation of water protons. Some widely applied strategies to achieve high relaxivity forMRI contrast enhancement such as confinement of CAs in mesopores, doping with metal ions, and self-assembly or disassembly have been discussed. In addition, other recently developed novel strategies including valency change, oxygen vacancy, and distance-dependent tuning have been briefly described. While there is no simple answer to the question of "how do these factors impact relaxivity of NPs," several principles that can guide the engineering of future NPs as high-performance MRI CAs are as follows:

1. Size effect of NPs will determine whether surface-tovolume ratio or τ_R is the dominant contributing factor for generating T_1 contrast with any given NP. Meanwhile, size-dependent magnetization of magnetic NPs can be utilized in the design of T_2 CAs with high r_2 values.

2. Surface modification of NPs is indispensable not only for controlling NP growth but also for increasing compatibility and functionalization of NPs. The surface of NPs can be further adjusted to enhance or reduce MRI signal after size, which depends on coating species, hydrophilicity, density, and thickness of organic ligands, silica shells, and inorganic layers.

3. Shape confinement of Gd^{3+}-based CAs has recently been utilized to impact relaxation of water protons by engineering Gd^{3+} chelates into dense and hydrophilic microenvironments that are closely related to the shape of NPs. In the meantime, the magnetic field inhomogeneity enhanced by shape anisotropy of magnetic NPs can be artificially regulated to enhance T_2 relaxivity by reducing symmetry of the induced field.

4. Biodistribution, pharmacokinetics, and metabolism of NPs are also mediated by factors such as particle size, surface, and shape. The successful engineering of NPs as high-performance imaging agents must consider their behavior *in vivo*. Ultrasmall sized NPs with higher relaxivity are promising imaging agents because they can be excreted by the kidneys on a short time scale.

5. Strategies to achieve high relaxivity for MRI contrast enhancement are mainly focused on tuning the interaction between NPs and nearby water protons, either enhancing or reducing the contrast of MRI. By further exploiting tumor microenvironment characteristics such as acidic pH, unevenness of blood flow, and hypoxia, engineering of NPs for stimuliresponsive MRI can be realized for the precise imaging of tumors and detection of their pathological conditions with MRI.

Despite the recent significant progress and promising results in preclinical animal models, the investigation, evaluation, and optimization of NP-based MRI CAs for clinical use are still in their infancy. To facilitate and enable the successful translation of these CAs from laboratories to clinics, we outline several considerations for future research on the interdisciplinary cooperation among engineers, material scientists, biologists, clinicians, and others toward future (molecular) MRI (Fig. 24).

1. Although some factors/strategies have been explored by regulating the key parameters that influence the perturbation of protons by the dipolar field of NPs,

we believe that more novel factors/strategies for the design of high-relaxivity CAs are on the horizon. In addition, because the biodistribution, excretion, and pharmacokinetics of NPs are dependent on their size, shape, and surface status, rigorous and extensive attention should be paid to deep understanding the co-relations among nanoparticle characteristics (*e.g.*, size, shape, and surface status), *in vivo* metabolism, and MRI contrast enhancement efficiency. Through a basic understanding of how these factors work together, future clinical applications may be realized. Synergistic integration of these factors may offer promising approaches in fabricating low-toxicity and high-performance CAs that are amenable to clinical translation which will eventually benefit patients.[18]

2. Efficient systemic delivery of CAs to the targeted tissues is of utmost importance for accurate and sensitive detection by MRI, which can include passive accumulation of elaborately synthesized NPs to maximize enhanced permeability and retention (EPR) effect, as well as active targeting of NPs *via* various ligands such as antibodies, antibody fragments, peptides, small molecules, and proteins. The impacts of nanoparticle size, surface modification, and shape on proton relaxation have been well studied, while their relationship with the EPR effect remains to be further elucidated. Generally, ultra-small sized renal clearable NPs exhibit poor EPR effect.[215] Future studies should focus on the specific interaction between MRI contrast performance of CAs and EPR effect to develop a clinically relevant and useful strategy for obtaining high-relaxivity NPs with an optimal balance between renal clearance and strong EPR effects over a suitable time scale (*e.g.*, less than a few hours).[216]

3. The hypoxic microenvironment in various tumors has received tremendous attention from researchers because it is closely related to the tumor's aggressiveness and resistance to therapy,[217,218] and a number of NPs have been used to effectively eradicate hypoxic tumors in preclinical animal models.[219-222] Although in this review article we have discussed various strategies based on NPs for efficient MRI, there has been no literature report on hypoxia-responsive NPs as MRI CAs except on several chemical complexes for hypoxia-related MRI such as T_1 or T_2 CAs,[223] ^{19}F-based probes,[224] and CEST probes.[86] We believe that research on this subject is likely already in progress, and the NPs that respond to hypoxia *via*, for example, valency change, size/morphology variation, assembly, and disassembly for enhanced MRI, will likely play multiple roles in accurate and noninvasive delineation of hypoxic areas, more precise and effective treatment, and real-time and noninvasive monitoring of therapeutic efficacy.

4. The next generation of MRI CAs will be developed not only based on design principles of NPs described in this review article, but also on the concurrent development of advanced nanotechnology, novel MRI sequences and scanners, and new biological applications. The synthesis of these NPs needs further optimization, and NPs that are synthesized in an easy, low-cost, and large-scale way is prerequisite to future clinical translation, a challenge which may be overcome by seeking more facile, reproducible, and economic one-pot syntheses without harmful reagents. With an in-depth understanding of the involved

processes, we firmly believe that good biocompatibility and biodegradability, high relaxivity, and novelMRI contrast mechanisms can all be achieved with the future generation of novel inorganic NPs to usher in the new era of 21st century precision medicine (Table 3).

Acknowledgments

This work has been financially supported by the China National Funds for Distinguished Young Scientists (Grant No. 51725202), the National Natural Science Foundation of China (Grant No. 51372260) and the Shanghai Excellent Academic Leaders Program (Grant No. 16XD1404000). This work was also supported, in part, by the University of Wisconsin – Madison, the National Institutes of Health (NIBIB/NCI 1R01CA169365, 1R01EB021336, T32GM008505, and P30CA014520), and the American Cancer Society (125246-RSG-13-099-01-CCE).

References

1. Cao Y, Depinho RA, Ernst M, Vousden K. Nat Rev Cancer. 2011; 11:749. [PubMed: 21918542]
2. Rudin M, Weissleder R. Nat Rev Drug Discovery. 2003; 2:123. [PubMed: 12563303]
3. Smith BR, Gambhir SS. Chem Rev. 2017; 117:901. [PubMed: 28045253]
4. Angelovski G. Angew Chem Int Ed. 2016; 55:7038.
5. Lohrke J, Frenzel T, Endrikat J, Alves FC, Grist TM, Law M, Lee JM, Leiner T, Li K-C, Nikolaou K. Adv Ther. 2016; 33:1. [PubMed: 26809251]
6. Burtea, C., Laurent, S., Vander Elst, L., Muller, RN. Molecular imaging I. Springer; 2008. p. 135
7. Raymond KN, Pierre VC. Bioconjugate Chem. 2005; 16:3.
8. Penfield JG, Reilly RF. Nat Clin Pract Nephrol. 2007; 3:654. [PubMed: 18033225]
9. Estelrich J, Sanchez-Martin MJ, Busquets MA. Int J Nanomed. 2015; 10:1727.
10. Zhou Z, Lu ZR. Wiley Interdiscip Rev : Nanomed Nanobiotechnol. 2013; 5:1. [PubMed: 23047730]
11. Cao Y, Xu LJ, Kuang Y, Xiong DS, Pei RJ. J Mater Chem B. 2017; 5:3431.
12. Pan D, Caruthers SD, Senpan A, Schmieder AH, Wickline SA, Lanza GM. Wiley Interdiscip Rev : Nanomed Nanobiotechnol. 2011; 3:162. [PubMed: 20860051]
13. Pan D, Schmieder AH, Wickline SA, Lanza GM. Tetrahedron. 2011; 67:8431. [PubMed: 22043109]
14. Shen Z, Wu A, Chen X. Mol Pharmaceutics. 2017; 14:1352.
15. Reddy LH, Arias JL, Nicolas J, Couvreur P. Chem Rev. 2012; 112:5818. [PubMed: 23043508]
16. Lee H, Shin TH, Cheon J, Weissleder R. Chem Rev. 2015; 115:10690. [PubMed: 26258867]
17. Feliu N, Docter D, Heine M, del Pino P, Ashraf S, Kolosnjaj-Tabi J, Macchiarini P, Nielsen P, Alloyeau D, Gazeau F, Stauber RH, Parak WJ. Chem Soc Rev. 2016; 45:2440. [PubMed: 26862602]
18. Park, S-m, Aalipour, A., Vermesh, O., Yu, JH., Gambhir, SS. Nat Rev Mater. 2017; 2:17014.
19. Das GK, Johnson NJJ, Cramen J, Blasiak B, Latta P, Tomanek B, van Veggel FCJM. J Phys Chem Lett. 2012; 3:524. [PubMed: 26286058]
20. Zhang X, Blasiak B, Marenco AJ, Trudel S, Tomanek B, van Veggel FCJM. Chem Mater. 2016; 28:3060.
21. Ni D, Zhang J, Bu W, Zhang C, Yao Z, Xing H, Wang J, Duan F, Liu Y, Fan W, Feng X, Shi J. Biomaterials. 2016; 76:218. [PubMed: 26546914]
22. Prodi L, Rampazzo E, Rastrelli F, Speghini A, Zaccheroni N. Chem Soc Rev. 2015; 44:4922. [PubMed: 26090530]
23. Lee DE, Koo H, Sun IC, Ryu JH, Kim K, Kwon IC. Chem Soc Rev. 2012; 41:2656. [PubMed: 22189429]
24. Shin TH, Choi Y, Kim S, Cheon J. Chem Soc Rev. 2015; 44:4501. [PubMed: 25652670]
25. Chen H, Zhang W, Zhu G, Xie J, Chen X. Nat Rev Mater. 2017; 2:17024. [PubMed: 29075517]

26. Na HB, Song IC, Hyeon T. Adv Mater. 2009; 21:2133.
27. Lee SH, Kim BH, Na HB, Hyeon T. Wiley Interdiscip Rev : Nanomed Nanobiotechnol. 2014; 6:196. [PubMed: 24123961]
28. Huang J, Zhong X, Wang L, Yang L, Mao H. Theranostics. 2012; 2:86. [PubMed: 22272222]
29. Lee N, Hyeon T. Chem Soc Rev. 2012; 41:2575. [PubMed: 22138852]
30. Jun YW, Lee JH, Cheon J. Angew Chem Int Ed. 2008; 47:5122.
31. Zhou Z, Bai R, Munasinghe J, Shen Z, Nie L, Chen X. ACS Nano. 2017; 11:5227. [PubMed: 28613821]
32. Hingorani DV, Bernstein AS, Pagel MD. Contrast Media Mol Imaging. 2015; 10:245. [PubMed: 25355685]
33. van Duijnhoven SM, Robillard MS, Langereis S, Grull H. Contrast Media Mol Imaging. 2015; 10:282. [PubMed: 25873263]
34. Angelovski G. Acc Chem Res. 2017; 50:2215. [PubMed: 28841293]
35. Caravan P, Ellison JJ, McMurry TJ, Lauffer RB. Chem Rev. 1999; 99:2293. [PubMed: 11749483]
36. Zheng XY, Zhao K, Tang J, Wang XY, Li LD, Chen NX, Wang YJ, Shi S, Zhang X, Malaisamy S, Sun LD, Wang X, Chen C, Yan CH. ACS Nano. 2017; 11:3642. [PubMed: 28350963]
37. Ni D, Zhang J, Wang J, Hu P, Jin Y, Tang Z, Yao Z, Bu W, Shi J. ACS Nano. 2017; 11:4256. [PubMed: 28323405]
38. Ni D, Shen Z, Zhang J, Zhang C, Wu R, Liu J, Yi M, Wang J, Yao Z, Bu W, Shi J. ACS Nano. 2016; 10:3783. [PubMed: 26910513]
39. Johnson NJ, He S, VA Huu Nguyen, Almutairi A. ACS Nano. 2016; 10:8299. [PubMed: 27588579]
40. Xing H, Zhang S, Bu W, Zheng X, Wang L, Xiao Q, Ni D, Zhang J, Zhou L, Peng W, Zhao K, Hua Y, Shi J. Adv Mater. 2014; 26:3867. [PubMed: 24677351]
41. Hou Y, Qiao R, Fang F, Wang X, Dong C, Liu K, Liu C, Liu Z, Lei H, Wang F, Gao M. ACS Nano. 2013; 7:330. [PubMed: 23199030]
42. Shao Y, Tian X, Hu W, Zhang Y, Liu H, He H, Shen Y, Xie F, Li L. Biomaterials. 2012:6438. [PubMed: 22704842]
43. Kimura Y, Kamisugi R, Narazaki M, Matsuda T, Tabata Y, Toshimitsu A, Kondo T. Adv Healthcare Mater. 2012; 1:657.
44. Ahren M, Selegard L, Klasson A, Soderlind F, Abrikossova N, Skoglund C, Bengtsson T, Engstrom M, Kall PO, Uvdal K. Langmuir. 2010; 26:5753. [PubMed: 20334417]
45. Bridot J-L, Faure A-C, Laurent S, Rivière C, Billotey C, Hiba B, Janier M, Josserand V, Coll J-L, Vander Elst L, Muller R, Roux S, Perriat P, Tillement O. J Am Chem Soc. 2007; 129:5076. [PubMed: 17397154]
46. Evanics F, Diamente PR, van Veggel FCJM, Stanisz GJ, Prosser RS. Chem Mater. 2006; 18:2499.
47. Toth E, Bolskar RD, Borel A, Gonzalez G, Helm L, Merbach AE, Sitharaman B, Wilson LJ. J Am Chem Soc. 2005; 127:799. [PubMed: 15643906]
48. Park JY, Baek MJ, Choi ES, Woo S, Kim JH, Kim TJ, Jung JC, Chae KS, Chang Y, Lee GH. ACS Nano. 2009; 3:3663. [PubMed: 19835389]
49. Johnson NJJ, Oakden W, Stanisz GJ, Scott Prosser R, van Veggel FCJM. Chem Mater. 2011; 23:3714.
50. Silva AC, Lee JH, Aoki I, Koretsky AP. NMR Biomed. 2004; 17:532. [PubMed: 15617052]
51. Ma Z, Jia X, Bai J, Ruan Y, Wang C, Li J, Zhang M, Jiang X. Adv Funct Mater. 2017; 27:1604258.
52. Mi P, Kokuryo D, Cabral H, Wu H, Terada Y, Saga T, Aoki I, Nishiyama N, Kataoka K. Nat Nanotechnol. 2016; 11:724. [PubMed: 27183055]
53. Fan W, Bu W, Shen B, He Q, Cui Z, Liu Y, Zheng X, Zhao K, Shi J. Adv Mater. 2015; 27:4155. [PubMed: 26058562]
54. Zhao Z, Fan H, Zhou G, Bai H, Liang H, Wang R, Zhang X, Tan W. J Am Chem Soc. 2014; 136:11220. [PubMed: 25061849]
55. Chen Y, Ye D, Wu M, Chen H, Zhang L, Shi J, Wang L. Adv Mater. 2014; 26:7019. [PubMed: 25156250]

56. Chen Y, Xu P, Shu Z, Wu M, Wang L, Zhang S, Zheng Y, Chen H, Wang J, Li Y, Shi J. Adv Funct Mater. 2014; 24:4386.
57. Liu ZJ, Song XX, Tang Q. Nanoscale. 2013; 5:5073. [PubMed: 23640287]
58. Kim SM, Im GH, Lee DG, Lee JH, Lee WJ, Lee IS. Biomaterials. 2013; 34:8941. [PubMed: 23973173]
59. Létourneau M, Tremblay M, Faucher L, Rojas D, Chevallier P, Gossuin Y, Lagueux J, Fortin M-A. J Phys Chem B. 2012; 116:13228. [PubMed: 23030472]
60. Lee YC, Chen DY, Dodd SJ, Bouraoud N, Koretsky AP, Krishnan KM. Biomaterials. 2012; 33:3560. [PubMed: 22341582]
61. Chen Y, Yin Q, Ji XF, Zhang SJ, Chen HR, Zheng YY, Sun Y, Qu HY, Wang Z, Li YP, Wang X, Zhang K, Zhang LL, Shi JL. Biomaterials. 2012; 33:7126. [PubMed: 22789722]
62. Kim T, Momin E, Choi J, Yuan K, Zaidi H, Kim J, Park M, Lee N, McMahon MT, Quinones-Hinojosa A, Bulte JW, Hyeon T, Gilad AA. J Am Chem Soc. 2011; 133:2955. [PubMed: 21314118]
63. Kim T, Cho EJ, Chae Y, Kim M, Oh A, Jin J, Lee ES, Baik H, Haam S, Suh JS, Huh YM, Lee K. Angew Chem Int Ed. 2011; 50:10589.
64. Chen Y, Chen H, Sun Y, Zheng Y, Zeng D, Li F, Zhang S, Wang X, Zhang K, Ma M, He Q, Zhang L, Shi J. Angew Chem Int Ed. 2011; 50:12505.
65. Bennewitz MF, Lobo TL, Nkansah MK, Ulas G, Brudvig GW, Shapiro EM. ACS Nano. 2011; 5:3438. [PubMed: 21495676]
66. Yang H, Zhuang Y, Hu H, Du X, Zhang C, Shi X, Wu H, Yang S. Adv Funct Mater. 2010; 20:1733.
67. Schladt TD, Shukoor MI, Schneider K, Tahir MN, Natalio F, Ament I, Becker J, Jochum FD, Weber S, Köhler O. Angew Chem Int Ed. 2010; 49:3976.
68. Shin J, Anisur RM, Ko MK, Im GH, Lee JH, Lee IS. Angew Chem Int Ed. 2009; 48:321.
69. Na HB, Lee JH, An K, Park YI, Park M, Lee IS, Nam DH, Kim ST, Kim SH, Kim SW, Lim KH, Kim KS, Kim SO, Hyeon T. Angew Chem Int Ed. 2007; 46:5397.
70. Norek M, Kampert E, Zeitler U, Peters JA. J Am Chem Soc. 2008; 130:5335. [PubMed: 18355014]
71. Norek M, Peters JA. Prog Nucl Magn Reson Spectrosc. 2011; 59:64. [PubMed: 21600356]
72. Kattel K, Park JY, Xu W, Kim HG, Lee EJ, Bony BA, Heo WC, Jin S, Baeck JS, Chang Y, Kim TJ, Bae JE, Chae KS, Lee GH. Biomaterials. 2012; 33:3254. [PubMed: 22277624]
73. Das GK, Zhang Y, D'Silva L, Padmanabhan P, Heng BC, Chye Loo JS, Selvan ST, Bhakoo KK, Yang Tan TT. Chem Mater. 2011; 23:2439.
74. Kattel K, Park JY, Xu W, Kim HG, Lee EJ, Bony BA, Heo WC, Lee JJ, Jin S, Baeck JS, Chang Y, Kim TJ, Bae JE, Chae KS, Lee GH. ACS Appl Mater Interfaces. 2011; 3:3325. [PubMed: 21853997]
75. Kolosnjaj-Tabi J, Lartigue L, Javed Y, Luciani N, Pellegrino T, Wilhelm C, Alloyeau D, Gazeau F. Nano Today. 2016; 11:280.
76. Xie J, Chen K, Lee HY, Xu C, Hsu AR, Peng S, Chen X, Sun S. J Am Chem Soc. 2008; 130:7542. [PubMed: 18500805]
77. Gao J, Liang G, Cheung JS, Pan Y, Kuang Y, Zhao F, Zhang B, Zhang X, Wu EX, Xu B. J Am Chem Soc. 2008; 130:11828. [PubMed: 18681432]
78. Park J, An K, Hwang Y, Park JG, Noh HJ, Kim JY, Park JH, Hwang NM, Hyeon T. Nat Mater. 2004; 3:891. [PubMed: 15568032]
79. Jun Y-W, Huh Y-M, Choi J-S, Lee J-H, Song H-T, Kim S, Yoon S, Kim K-S, Shin J-S, Suh J-S, Cheon J. J Am Chem Soc. 2005; 127:5732. [PubMed: 15839639]
80. Mohapatra J, Mitra A, Tyagi H, Bahadur D, Aslam M. Nanoscale. 2015; 7:9174. [PubMed: 25849780]
81. Joshi HM, Lin YP, Aslam M, Prasad PV, Schultz-Sikma EA, Edelman R, Meade T, Dravid VP. J Phys Chem C. 2009; 113:17761.
82. Song Q, Zhang ZJ. J Am Chem Soc. 2004; 126:6164. [PubMed: 15137781]
83. Jang JT, Nah H, Lee JH, Moon SH, Kim MG, Cheon J. Angew Chem Int Ed. 2009; 48:1234.

84. Lee JH, Huh YM, Jun YW, Seo JW, Jang JT, Song HT, Kim S, Cho EJ, Yoon HG, Suh JS, Cheon J. Nat Med. 2007; 13:95. [PubMed: 17187073]
85. Tsitovich PB, Spernyak JA, Morrow JR. Angew Chem Int Ed. 2013; 52:13997.
86. Funk AM, Clavijo Jordan V, Sherry AD, Ratnakar SJ, Kovacs Z. Angew Chem Int Ed. 2016; 55:5024.
87. Aime S, Fasano M, Terreno E. Chem Soc Rev. 1998; 27:19.
88. Solomon I. Phys Rev. 1955; 99:559.
89. Debroye E, Parac-Vogt TN. Chem Soc Rev. 2014; 43:8178. [PubMed: 25211043]
90. Tsai CP, Hung Y, Chou YH, Huang DM, Hsiao JK, Chang C, Chen YC, Mou CY. Small. 2008; 4:186. [PubMed: 18205156]
91. Taylor KM, Kim JS, Rieter WJ, An H, Lin W. J Am Chem Soc. 2008; 130:2154. [PubMed: 18217764]
92. Hsiao JK, Tsai CP, Chung TH, Hung Y, Yao M, Liu HM, Mou CY, Yang CS, Chen YC, Huang DM. Small. 2008; 4:1445. [PubMed: 18680095]
93. Endres PJ, Paunesku T, Vogt S, Meade TJ, Woloschak GE. J Am Chem Soc. 2007; 129:15760. [PubMed: 18047347]
94. Culver KSB, Shin YJ, Rotz MW, Meade TJ, Hersam MC, Odom TW. J Phys Chem C. 2016; 120:22103.
95. Rotz MW, Culver KS, Parigi G, MacRenaris KW, Luchinat C, Odom TW, Meade TJ. ACS Nano. 2015; 9:3385. [PubMed: 25723190]
96. Bruckman MA, Yu X, Steinmetz NF. Nanotechnology. 2013; 24:462001. [PubMed: 24158750]
97. Song Y, Xu X, MacRenaris KW, Zhang XQ, Mirkin CA, Meade TJ. Angew Chem Int Ed. 2009; 48:9143.
98. Alric C, Taleb J, Le Duc G, Mandon C, Billotey C, Le Meur-Herland A, Brochard T, Vocanson F, Janier M, Perriat P, Roux S, Tillement O. J Am Chem Soc. 2008; 130:5908. [PubMed: 18407638]
99. Helm L, Merbach A. Coord Chem Rev. 1999; 187:151.
100. Aime S, Barge A, Borel A, Botta M, Chemerisov S, Merbach AE, Müller U, Pubanz D. Inorg Chem. 1997; 36:5104.
101. Pierre VC, Botta M, Aime S, Raymond KN. Inorg Chem. 2006; 45:8355. [PubMed: 16999435]
102. Gillis P, Koenig SH. Magn Reson Med. 1987; 5:323. [PubMed: 2824967]
103. Gillis P, Moiny F, Brooks RA. Magn Reson Med. 2002; 47:257. [PubMed: 11810668]
104. Brooks RA, Moiny F, Gillis P. Magn Reson Med. 2001; 45:1014. [PubMed: 11378879]
105. Tong S, Hou S, Zheng Z, Zhou J, Bao G. Nano Lett. 2010; 10:4607. [PubMed: 20939602]
106. Willets KA, Van Duyne RP. Annu Rev Phys Chem. 2007; 58:267. [PubMed: 17067281]
107. Luther JM, Jain PK, Ewers T, Alivisatos AP. Nat Mater. 2011; 10:361. [PubMed: 21478881]
108. Alivisatos AP. Science. 1996; 271:933.
109. Kodama R. J Magn Magn Mater. 1999; 200:359.
110. Tong S, Quinto CA, Zhang L, Mohindra P, Bao G. ACS Nano. 2017; 11:6808. [PubMed: 28625045]
111. Lu F, Wu SH, Hung Y, Mou CY. Small. 2009; 5:1408. [PubMed: 19296554]
112. Sonavane G, Tomoda K, Makino K. Colloids Surf B. 2008; 66:274.
113. Briley-Saebo KC, Johansson LO, Hustvedt SO, Haldorsen AG, Bjørnerud A, Fayad ZA, Ahlstrom HK. Invest Radiol. 2006; 41:560. [PubMed: 16772849]
114. Hoshyar N, Gray S, Han H, Bao G. Nanomedicine. 2016; 11:673. [PubMed: 27003448]
115. Talamini L, Violatto MB, Cai Q, Monopoli MP, Kantner K, Krpetic Z, Perez-Potti A, Cookman J, Garry D, Silveira CP, Boselli L, Pelaz B, Serchi T, Cambier S, Gutleb AC, Feliu N, Yan Y, Salmona M, Parak WJ, Dawson KA, Bigini P. ACS Nano. 2017; 11:5519. [PubMed: 28558193]
116. Huang C-C, Su C-H, Li W-M, Liu T-Y, Chen J-H, Yeh C-S. Adv Funct Mater. 2009; 19:249.
117. Passuello T, Pedroni M, Piccinelli F, Polizzi S, Marzola P, Tambalo S, Conti G, Benati D, Vetrone F, Bettinelli M. Nanoscale. 2012; 4:7682. [PubMed: 23117700]
118. Zheng X-Y, Sun L-D, Zheng T, Dong H, Li Y, Wang Y-F, Yan C-H. Sci Bull. 2015; 60:1092.

119. Li I-F, Yeh C-S. J Mater Chem. 2010; 20:2079.
120. Liu Y, Ai K, Yuan Q, Lu L. Biomaterials. 2011; 32:1185. [PubMed: 21055806]
121. Guo W, Yang W, Wang Y, Sun X, Liu Z, Zhang B, Chang J, Chen X. Nano Res. 2014; 7:1581. [PubMed: 25485043]
122. Zhang F, Sun T-T, Zhang Y, Li Q, Chai C, Lu L, Shen W, Yang J, He X-W, Zhang Y-K. J Mater Chem B. 2014; 2:7201.
123. Mulder WJ, Koole R, Brandwijk RJ, Storm G, Chin PT, Strijkers GJ, de Mello Donega C, Nicolay K, Griffioen AW. Nano Lett. 2006; 6:1. [PubMed: 16402777]
124. Kumar R, Nyk M, Ohulchanskyy TY, Flask CA, Prasad PN. Adv Funct Mater. 2009; 19:853.
125. Park YI, Kim HM, Kim JH, Moon KC, Yoo B, Lee KT, Lee N, Choi Y, Park W, Ling D, Na K, Moon WK, Choi SH, Park HS, Yoon SY, Suh YD, Lee SH, Hyeon T. Adv Mater. 2012; 24:5755. [PubMed: 22915170]
126. Naccache R, Chevallier P, Lagueux J, Gossuin Y, Laurent S, Vander Elst L, Chilian C, Capobianco JA, Fortin MA. Adv Healthcare Mater. 2013; 2:1478.
127. Du F, Zhang L, Zhang L, Zhang M, Gong A, Tan Y, Miao J, Gong Y, Sun M, Ju H. Biomaterials. 2017; 121:109. [PubMed: 28086179]
128. Yu C, Xuan T, Chen Y, Zhao Z, Liu X, Lian G, Li H. J Alloys Compd. 2016; 688:611.
129. Zhou L, Yang T, Wang J, Wang Q, Lv X, Ke H, Guo Z, Shen J, Wang Y, Xing C, Chen H. Theranostics. 2017; 7:764. [PubMed: 28255365]
130. Le Duc G, Miladi I, Alric C, Mowat P, Brauer-Krisch E, Bouchet A, Khalil E, Billotey C, Janier M, Lux F, Epicier T, Perriat P, Roux S, Tillement O. ACS Nano. 2011; 5:9566. [PubMed: 22040385]
131. Viger ML, Sankaranarayanan J, Lux CD, Chan M, Almutairi A. J Am Chem Soc. 2013; 135:7847. [PubMed: 23672342]
132. An K, Park M, Yu JH, Na HB, Lee N, Park J, Choi SH, Song IC, Moon WK, Hyeon T. Eur J Inorg Chem. 2012:2148.
133. Li B, Gu Z, Kurniawan N, Chen W, Xu ZP. Adv Mater. 2017; doi: 10.1002/adma.201700373
134. Seo WS, Jo HH, Lee K, Kim B, Oh SJ, Park JT. Angew Chem Int Ed. 2004; 43:1115.
135. Kim BH, Lee N, Kim H, An K, Park YI, Choi Y, Shin K, Lee Y, Kwon SG, Na HB, Park JG, Ahn TY, Kim YW, Moon WK, Choi SH, Hyeon T. J Am Chem Soc. 2011; 133:12624. [PubMed: 21744804]
136. Zhang H, Li L, Liu XL, Jiao J, Ng CT, Yi JB, Luo YE, Bay BH, Zhao LY, Peng ML, Gu N, Fan HM. ACS Nano. 2017; 11:3614. [PubMed: 28371584]
137. Zhao Z, Zhou Z, Bao J, Wang Z, Hu J, Chi X, Ni K, Wang R, Chen X, Chen Z, Gao J. Nat Commun. 2013; 4:2266. [PubMed: 23903002]
138. Huang J, Bu L, Xie J, Chen K, Cheng Z, Li X, Chen X. ACS Nano. 2010; 4:7151. [PubMed: 21043459]
139. Chen Y, Chen HR, Zhang SJ, Chen F, Sun SK, He QJ, Ma M, Wang X, Wu HX, Zhang LX, Zhang LL, Shi JL. Biomaterials. 2012; 33:2388. [PubMed: 22177841]
140. Liu J, Bu J, Bu W, Zhang S, Pan L, Fan W, Chen F, Zhou L, Peng W, Zhao K, Du J, Shi J. Angew Chem Int Ed. 2014; 53:4551.
141. Tromsdorf UI, Bruns OT, Salmen SC, Beisiegel U, Weller H. Nano Lett. 2009; 9:4434. [PubMed: 19799448]
142. Wei H, Bruns OT, Kaul MG, Hansen EC, Barch M, Wisniowska A, Chen O, Chen Y, Li N, Okada S, Cordero JM, Heine M, Farrar CT, Montana DM, Adam G, Ittrich H, Jasanoff A, Nielsen P, Bawendi MG. Proc Natl Acad Sci U S A. 2017; 114:2325. [PubMed: 28193901]
143. Wu M, Meng Q, Chen Y, Xu P, Zhang S, Li Y, Zhang L, Wang M, Yao H, Shi J. Adv Funct Mater. 2014; 24:4273.
144. Moon SH, Noh SH, Lee JH, Shin TH, Lim Y, Cheon J. Nano Lett. 2017; 17:800. [PubMed: 28045532]
145. Yablonskiy DA, Haacke EM. Magn Reson Med. 1994; 32:749. [PubMed: 7869897]

146. Seo WS, Lee JH, Sun X, Suzuki Y, Mann D, Liu Z, Terashima M, Yang PC, McConnell MV, Nishimura DG, Dai H. Nat Mater. 2006; 5:971. [PubMed: 17115025]
147. Tromsdorf UI, Bigall NC, Kaul MG, Bruns OT, Nikolic MS, Mollwitz B, Sperling RA, Reimer R, Hohenberg H, Parak WJ, Förster S, Beisiegel U, Adam G, Weller H. Nano Lett. 2007; 7:2422. [PubMed: 17658761]
148. Duan H, Kuang M, Wang X, Wang YA, Mao H, Nie S. J Phys Chem C. 2008; 112:8127.
149. Zeng J, Jing L, Hou Y, Jiao M, Qiao R, Jia Q, Liu C, Fang F, Lei H, Gao M. Adv Mater. 2014; 26:2694. [PubMed: 24615901]
150. Bowen CV, Zhang X, Saab G, Gareau PJ, Rutt BK. Magn Reson Med. 2002; 48:52. [PubMed: 12111931]
151. Roch A, Gossuin Y, Muller RN, Gillis P. J Magn Magn Mater. 2005; 293:532.
152. Suk JS, Xu Q, Kim N, Hanes J, Ensign LM. Adv Drug Delivery Rev. 2016; 99:28.
153. Xu Q, Ensign LM, Boylan NJ, Schon A, Gong X, Yang JC, Lamb NW, Cai S, Yu T, Freire E, Hanes J. ACS Nano. 2015; 9:9217. [PubMed: 26301576]
154. Liu J, Yu M, Ning X, Zhou C, Yang S, Zheng J. Angew Chem Int Ed. 2013; 52:12572.
155. Otsuka H, Nagasaki Y, Kataoka K. Adv Drug Delivery Rev. 2003; 55:403.
156. Chen Y, Chen H, Shi J. Adv Mater. 2013; 25:3144. [PubMed: 23681931]
157. Liu JN, Bu WB, Shi JL. Acc Chem Res. 2015; 48:1797. [PubMed: 26057000]
158. Chen WH, Luo GF, Lei Q, Cao FY, Fan JX, Qiu WX, Jia HZ, Hong S, Fang F, Zeng X, Zhuo RX, Zhang XZ. Biomaterials. 2016; 76:87. [PubMed: 26519651]
159. Chen F, Bu W, Zhang S, Liu J, Fan W, Zhou L, Peng W, Shi J. Adv Funct Mater. 2013; 23:298.
160. Peng YK, Lai CW, Liu CL, Chen HC, Hsiao YH, Liu WL, Tang KC, Chi Y, Hsiao JK, Lim KE, Liao HE, Shyue JJ, Chou PT. ACS Nano. 2011; 5:4177. [PubMed: 21548648]
161. Cheng L, Yang K, Li Y, Chen J, Wang C, Shao M, Lee ST, Liu Z. Angew Chem Int Ed. 2011; 50:7385.
162. Xia A, Gao Y, Zhou J, Li C, Yang T, Wu D, Wu L, Li F. Biomaterials. 2011; 32:7200. [PubMed: 21742376]
163. Cheong S, Ferguson P, Feindel KW, Hermans IF, Callaghan PT, Meyer C, Slocombe A, Su CH, Cheng FY, Yeh CS, Ingham B, Toney MF, Tilley RD. Angew Chem Int Ed. 2011; 50:4206.
164. Chen F, Bu W, Zhang S, Liu X, Liu J, Xing H, Xiao Q, Zhou L, Peng W, Wang L, Shi J. Adv Funct Mater. 2011; 21:4285.
165. Wang F, Deng R, Liu X. Nat Protoc. 2014; 9:1634. [PubMed: 24922272]
166. Ni D, Zhang J, Bu W, Xing H, Han F, Xiao Q, Yao Z, Chen F, He Q, Liu J, Zhang S, Fan W, Zhou L, Peng W, Shi J. ACS Nano. 2014; 8:1231. [PubMed: 24397730]
167. Kinnear C, Moore TL, Rodriguez-Lorenzo L, Rothen-Rutishauser B, Petri-Fink A. Chem Rev. 2017; 117:11476. [PubMed: 28862437]
168. Rikken RS, Nolte RJ, Maan JC, van Hest JC, Wilson DA, Christianen PC. Soft Matter. 2014; 10:1295. [PubMed: 24652392]
169. Huang X, Teng X, Chen D, Tang F, He J. Biomaterials. 2010; 31:438. [PubMed: 19800115]
170. Chithrani BD, Ghazani AA, Chan WC. Nano Lett. 2006; 6:662. [PubMed: 16608261]
171. Huang X, Li L, Liu T, Hao N, Liu H, Chen D, Tang F. ACS Nano. 2011; 5:5390. [PubMed: 21634407]
172. Albanese A, Tang PS, Chan WC. Annu Rev Biomed Eng. 2012; 14:1. [PubMed: 22524388]
173. Toy R, Peiris PM, Ghaghada KB, Karathanasis E. Nanomedicine. 2014; 9:121. [PubMed: 24354814]
174. Liu C, Gao Z, Zeng J, Hou Y, Fang F, Li Y, Qiao R, Shen L, Lei H, Yang W, Gao M. ACS Nano. 2013; 7:7227. [PubMed: 23879437]
175. Zhao M, Beauregard DA, Loizou L, Davletov B, Brindle KM. Nat Med. 2001; 7:1241. [PubMed: 11689890]
176. Yang L, Mao H, Wang YA, Cao Z, Peng X, Wang X, Duan H, Ni C, Yuan Q, Adams G. Small. 2009; 5:235. [PubMed: 19089838]

177. Weissleder R, Moore A, Mahmood U, Bhorade R, Benveniste H, Chiocca EA, Basilion JP. Nat Med. 2000; 6:351. [PubMed: 10700241]
178. Louie AY, Huber MM, Ahrens ET, Rothbacher U, Moats R, Jacobs RE, Fraser SE, Meade TJ. Nat Biotechnol. 2000; 18:321. [PubMed: 10700150]
179. Torres E, Mainini F, Napolitano R, Fedeli F, Cavalli R, Aime S, Terreno E. J Controlled Release. 2011; 154:196.
180. Lim EK, Huh YM, Yang J, Lee K, Suh JS, Haam S. Adv Mater. 2011; 23:2436. [PubMed: 21491515]
181. Yang X, Grailer JJ, Rowland IJ, Javadi A, Hurley SA, Matson VZ, Steeber DA, Gong S. ACS Nano. 2010; 4:6805. [PubMed: 20958084]
182. Chan KW, Liu G, Song X, Kim H, Yu T, Arifin DR, Gilad AA, Hanes J, Walczak P, van Zijl PC, Bulte JW, McMahon MT. Nat Mater. 2013; 12:268. [PubMed: 23353626]
183. Nejadnik H, Lenkov O, Gassert F, Fretwell D, Lam I, Daldrup-Link HE. Sci Rep. 2016; 6:25897. [PubMed: 27174199]
184. Nejadnik H, Ye D, Lenkov OD, Donig JS, Martin JE, Castillo R, Derugin N, Sennino B, Rao J, Daldrup-Link H. ACS Nano. 2015; 9:1150. [PubMed: 25597243]
185. Schwarz S, Wong JE, Bornemann J, Hodenius M, Himmelreich U, Richtering W, Hoehn M, Zenke M, Hieronymus T. Nanomedicine. 2012; 8:682. [PubMed: 21893141]
186. Ananta JS, Godin B, Sethi R, Moriggi L, Liu X, Serda RE, Krishnamurthy R, Muthupillai R, Bolskar RD, Helm L, Ferrari M, Wilson LJ, Decuzzi P. Nat Nanotechnol. 2010; 5:815. [PubMed: 20972435]
187. Ni K, Zhao Z, Zhang Z, Zhou Z, Yang L, Wang L, Ai H, Gao J. Nanoscale. 2016; 8:3768. [PubMed: 26814592]
188. Huang P, Qian X, Chen Y, Yu L, Lin H, Wang L, Zhu Y, Shi J. J Am Chem Soc. 2017; 139:1275. [PubMed: 28024395]
189. Zhang Q, Wang P, Ling Y, Li X, Xia L, Yang Y, Liu X, Zhang F, Zhou Y. Adv Funct Mater. 2017; 27:1605313.
190. Lu AH, Salabas EL, Schuth F. Angew Chem Int Ed. 2007; 46:1222.
191. Chung R-J, Ou K-L, Chen S-P, Liu H-L. Adv Powder Technol. 2016; 27:994.
192. Chou S-W, Liu C-L, Liu T-M, Shen Y-F, Kuo L-C, Wu C-H, Hsieh T-Y, Wu P-C, Tsai M-R, Yang C-C. Biomaterials. 2016; 85:54. [PubMed: 26854391]
193. Sun S. Adv Mater. 2006; 18:393.
194. Chou SW, Shau YH, Wu PC, Yang YS, Shieh DB, Chen CC. J Am Chem Soc. 2010; 132:13270. [PubMed: 20572667]
195. Perez JM, Josephson L, O'Loughlin T, Hogemann D, Weissleder R. Nat Biotechnol. 2002; 20:816. [PubMed: 12134166]
196. Gallo J, Kamaly N, Lavdas I, Stevens E, Nguyen QD, Wylezinska-Arridge M, Aboagye EO, Long NJ. Angew Chem Int Ed. 2014; 53:9550.
197. Yuan Y, Ding Z, Qian J, Zhang J, Xu J, Dong X, Han T, Ge S, Luo Y, Wang Y, Zhong K, Liang G. Nano Lett. 2016; 16:2686. [PubMed: 27031226]
198. Gao Z, Hou Y, Zeng J, Chen L, Liu C, Yang W, Gao M. Adv Mater. 2017:29.
199. Liang G, Ronald J, Chen Y, Ye D, Pandit P, Ma ML, Rutt B, Rao J. Angew Chem Int Ed. 2011; 50:6283.
200. Ye D, Pandit P, Kempen P, Lin J, Xiong L, Sinclair R, Rutt B, Rao J. Bioconjugate Chem. 2014; 25:1526.
201. Ye D, Shuhendler AJ, Pandit P, Brewer KD, Tee SS, Cui L, Tikhomirov G, Rutt B, Rao J. Chem Sci. 2014; 4:3845. [PubMed: 25429349]
202. Berret JF, Schonbeck N, Gazeau F, ElKharrat D, Sandre O, Vacher A, Airiau M. J Am Chem Soc. 2006; 128:1755. [PubMed: 16448152]
203. Ai H, Flask C, Weinberg B, Shuai XT, Pagel MD, Farrell D, Duerk J, Gao J. Adv Mater. 2005; 17:1949.
204. Chen H, Yeh J, Wang L, Khurshid H, Peng N, Wang AY, Mao H. Nano Res. 2010; 3:852.

205. Wang L, Huang J, Chen H, Wu H, Xu Y, Li Y, Yi H, Wang YA, Yang L, Mao H. ACS Nano. 2017; 11:4582. [PubMed: 28426929]
206. Martinelli J, Fekete M, Tei L, Botta M. Chem Commun. 2011; 47:3144.
207. Kim MH, Son HY, Kim GY, Park K, Huh YM, Haam S. Biomaterials. 2016; 101:121. [PubMed: 27281684]
208. Yu L, Chen Y, Wu M, Cai X, Yao H, Zhang L, Chen H, Shi J. J Am Chem Soc. 2016; 138:9881. [PubMed: 27441571]
209. Loving GS, Mukherjee S, Caravan P. J Am Chem Soc. 2013; 135:4620. [PubMed: 23510406]
210. Deng R, Xie X, Vendrell M, Chang YT, Liu X. J Am Chem Soc. 2011; 133:20168. [PubMed: 22107163]
211. Chu C, Lin H, Liu H, Wang X, Wang J, Zhang P, Gao H, Huang C, Zeng Y, Tan Y, Liu G, Chen X. Adv Mater. 2017:29.
212. Shi J. Chem Rev. 2013; 113:2139. [PubMed: 23190123]
213. Choi JS, Kim S, Yoo D, Shin TH, Kim H, Gomes MD, Kim SH, Pines A, Cheon J. Nat Mater. 2017; 16:537. [PubMed: 28166216]
214. Zhou Z, Tian R, Wang Z, Yang Z, Liu Y, Liu G, Wang R, Gao J, Song J, Nie L, Chen X. Nat Commun. 2017; 8:15468. [PubMed: 28516947]
215. Yu M, Zheng J. ACS Nano. 2015; 9:6655. [PubMed: 26149184]
216. Ehlerding EB, Chen F, Cai W. Adv Sci. 2016; 3
217. Liu JN, Bu W, Shi J. Chem Rev. 2017; 117:6160. [PubMed: 28426202]
218. Dai Y, Xu C, Sun X, Chen X. Chem Soc Rev. 2017; 46:3830. [PubMed: 28516983]
219. Song G, Liang C, Yi X, Zhao Q, Cheng L, Yang K, Liu Z. Adv Mater. 2016; 28:2716. [PubMed: 26848553]
220. Song G, Chen Y, Liang C, Yi X, Liu J, Sun X, Shen S, Yang K, Liu Z. Adv Mater. 2016; 28:7143. [PubMed: 27275921]
221. Chen Q, Feng L, Liu J, Zhu W, Dong Z, Wu Y, Liu Z. Adv Mater. 2016; 28:7129. [PubMed: 27283434]
222. Liu YY, Liu Y, Bu WB, Cheng C, Zuo CJ, Xiao QF, Sun Y, Ni DL, Zhang C, Liu JA, Shi JL. Angew Chem Int Ed. 2015; 54:8105.
223. Di Gregorio E, Ferrauto G, Gianolio E, Lanzardo S, Carrera C, Fedeli F, Aime S. ACS Nano. 2015; 9:8239. [PubMed: 26234938]
224. Tanabe K, Harada H, Narazaki M, Tanaka K, Inafuku K, Komatsu H, Ito T, Yamada H, Chujo Y, Matsuda T. J Am Chem Soc. 2009; 131:15982. [PubMed: 19842623]

Biographies

Dalong Ni

Dalong Ni received his PhD degree in 2016 from the Shanghai Institute of Ceramics, Chinese Academy of Sciences (SICCAS), under the supervision of Prof. Wenbo Bu. He then joined the Department of Radiology at the University of Wisconsin-Madison as a postdoctoral fellow under the supervision of Prof. Weibo Cai. His research interests focus on

design, synthesis, and biomedical applications of multifunctional nanoplatforms for imaging and therapy applications, such as MRI and MRI-guided cancer therapy.

Wenbo Bu

Wenbo Bu received his PhD degree from Nanjing Tech University (China) in 2002. He has been a full-time professor in SICCAS since 2008. In 2016, he moved from SICCAS to East China Normal University. His research mainly focuses on design and synthesis of multifunctional rareearth- based nanomaterials for cancer imaging and therapeutic applications.

Emily B. Ehlerding

Emily B. Ehlerding received her MS degree in Medical Physics from the University of Wisconsin- Madison in 2016 and her BS in Chemistry and Physics from Manchester University in 2014. She is currently a PhD candidate in Medical Physics at UW-Madison, working with antibody-based platforms for multimodality imaging of immunotherapy-related targets.

Weibo Cai

Weibo Cai received his PhD degree in Chemistry from University of California, San Diego, in 2004 and is now an associate professor at the University of Wisconsin- Madison (http://mi.wisc.edu). He has published more than 230 peerreviewed articles (H-index 4 60) and has

received many awards such as the Society of Nuclear Medicine and Molecular Imaging (SNMMI) Young Professionals Committee Best Basic Science Award (2007), the European Association of Nuclear Medicine Springer Prize (2011 & 2013), American Cancer Society Research Scholar (2013–2017), and UW-Madison Vilas Distinguished Achievement Professor Award (2017). His trainees have received more than 80 awards to date, such as the 2012 Berson-Yalow Award from SNMMI.

Jianlin Shi

Jianlin Shi received his PhD degree from SICCAS. He has been a full-time professor at SICCAS since 1994. His research interests include the synthesis of mesoporous silica nanoparticles and mesoporous silica-based nanocomposites for biomedical applications. He has published over 400 scientific papers, which have been cited more than 22 000 times by other scientists, and has an H-index of 79.

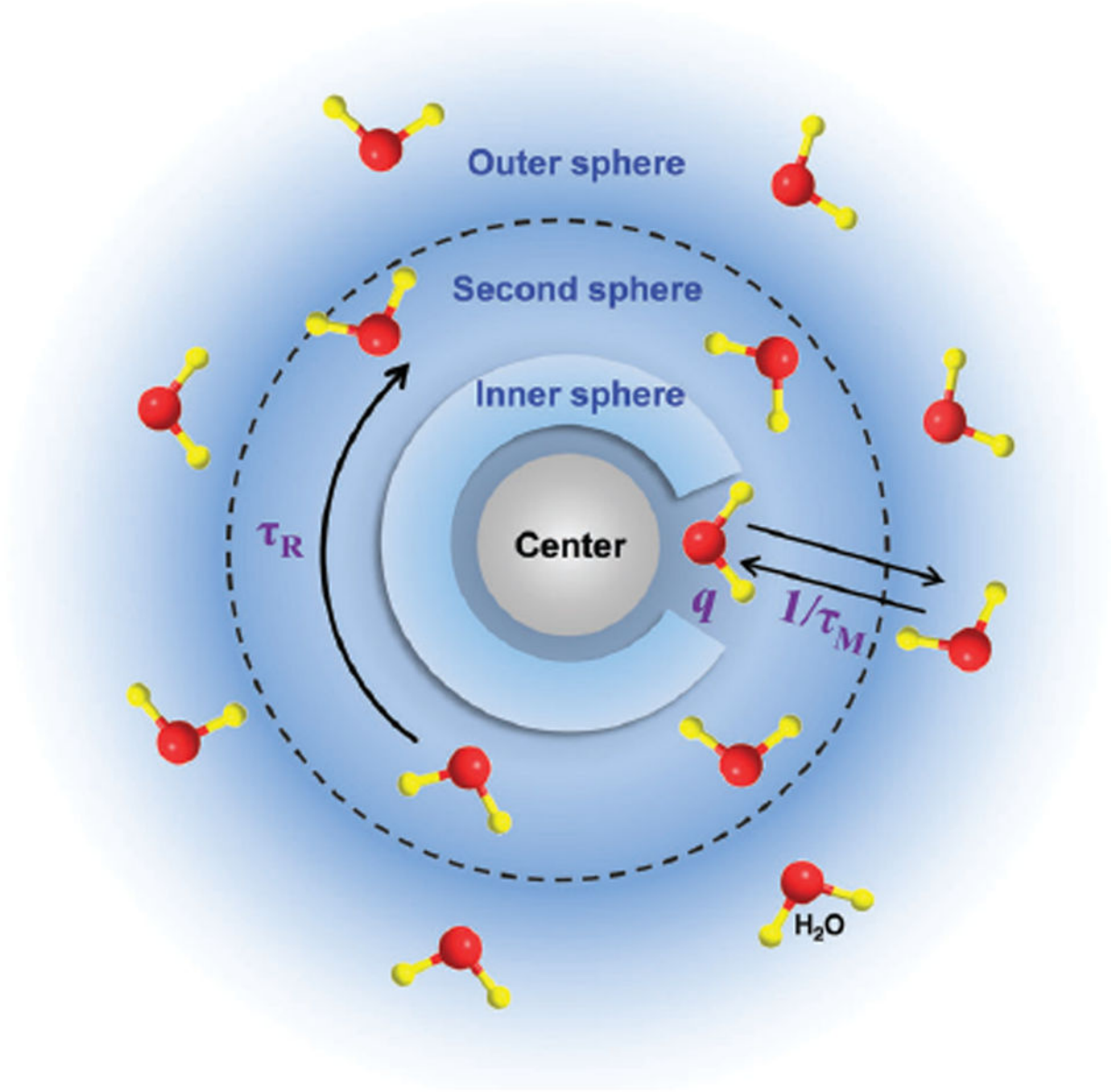

Fig. 1.
Inner sphere, secondary sphere, and outer sphere can influence relaxation rates of MRI CAs.

Fig. 2.
Factors influencing relaxation of MRI CAs: size, surface, and shape effects at the nanoscale.

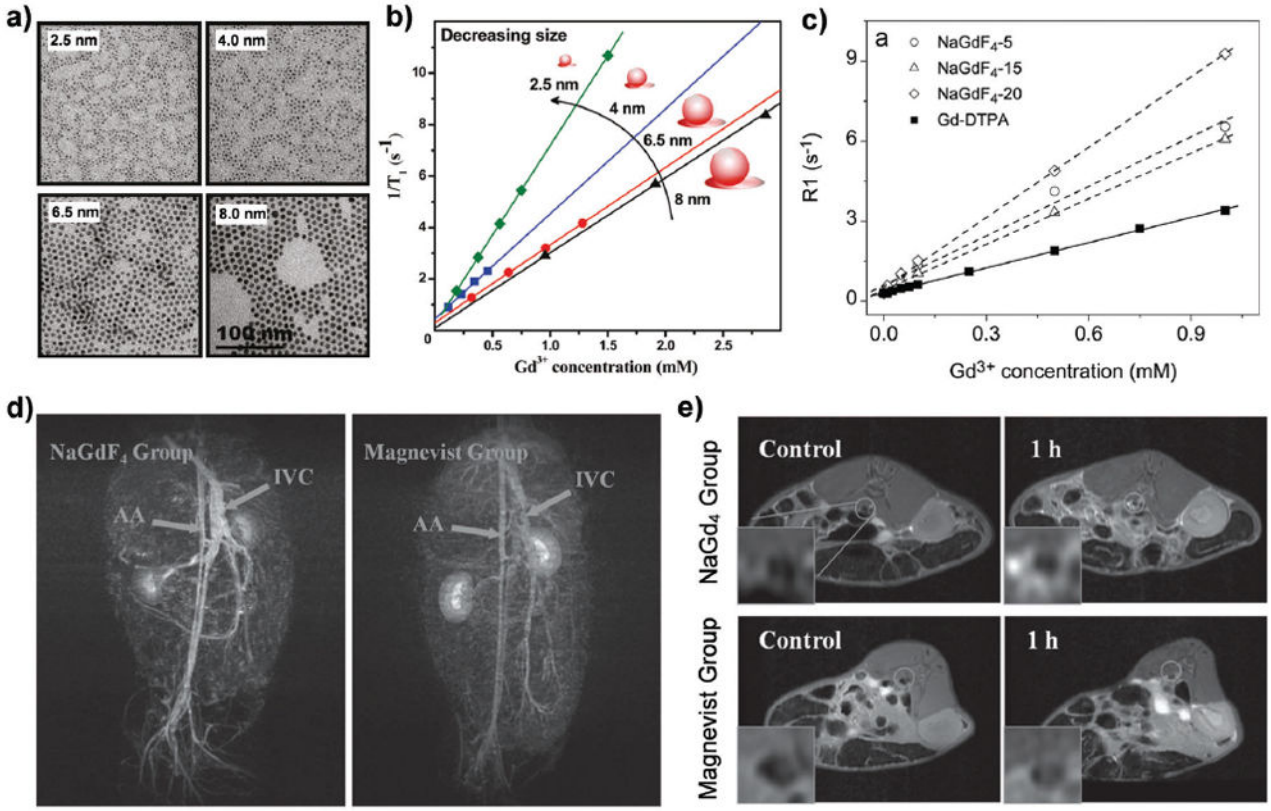

Fig. 3.

(a) TEM images of oleate-stabilized $NaGdF_4$ NPs of varied particle sizes (scale bar is the same for all images). (b) Plots of $1/T_1$ *versus* Gd^{3+} concentration for varied $NaGdF_4$ NPs in water (1.5 T). Reproduced with permission from ref. 49. Copyright 2011, American Chemical Society. (c) R_1 relaxivity of aqueous solutions containing $NaGdF_4$ NPs of different sizes or Gd–DTPA with different concentrations of Gd^{3+}. Reproduced with permission from ref. 41. Copyright 2013, American Chemical Society. (d) Magnetic resonance angiography of rabbits within 3 min after injection of ultra-small $NaGdF_4$ nanodots or Magnevist. AA: abdominal aorta; IVC: inferior vena cava. (e) Transverse cross-sectional images of rabbit atherosclerotic plaques before and after injection of ultra-small $NaGdF_4$ nanodots or Magnevist at the same dosage (13 mg Gd per kg). Reproduced with permission from ref. 40. Copyright 2014, Wiley-VCH.

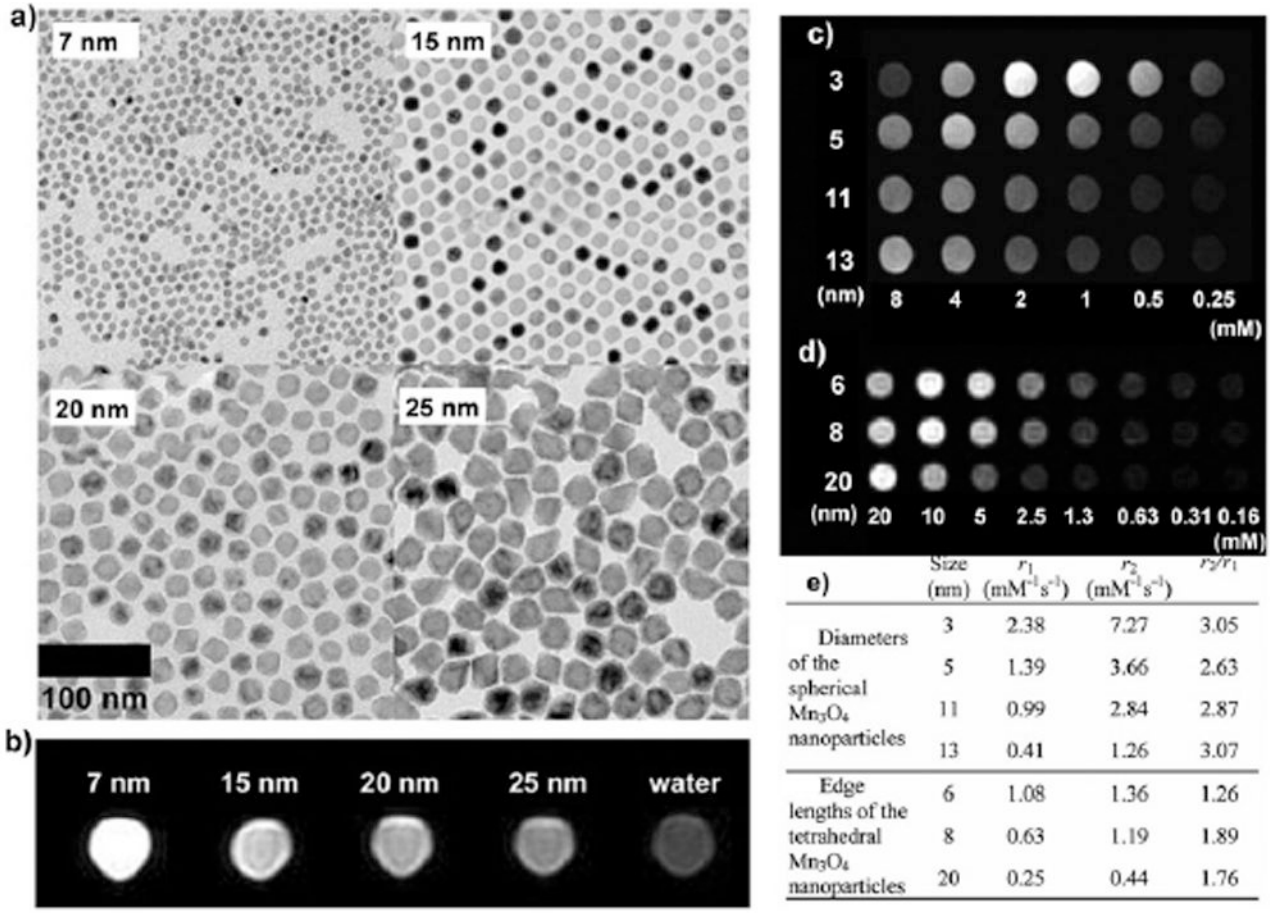

e)

	Size (nm)	r_1 ($mM^{-1}s^{-1}$)	r_2 ($mM^{-1}s^{-1}$)	r_2/r_1
Diameters of the spherical Mn_3O_4 nanoparticles	3	2.38	7.27	3.05
	5	1.39	3.66	2.63
	11	0.99	2.84	2.87
	13	0.41	1.26	3.07
Edge lengths of the tetrahedral Mn_3O_4 nanoparticles	6	1.08	1.36	1.26
	8	0.63	1.19	1.89
	20	0.25	0.44	1.76

Fig. 4.

(a) TEM images of MnO NPs of varied sizes (7, 15, 20, and 25 nm) in water. (b) T_1-weighted MR image of MnO NPs in a 3.0 T clinical MRI system. Reproduced with permission from ref. 69. Copyright 2007, Wiley-VCH. Size-dependent T_1-weighted MR images and relaxivities of water-dispersible spherical (c) and tetrahedral (d) Mn_3O_4 NPs at varied Mn^{2+} concentrations. (e) The r_1 and r_2 values and r_2/r_1 ratios of Mn_3O_4 MPs from c and d. Reproduced with permission from ref. 132. Copyright 2012, Wiley-VCH.

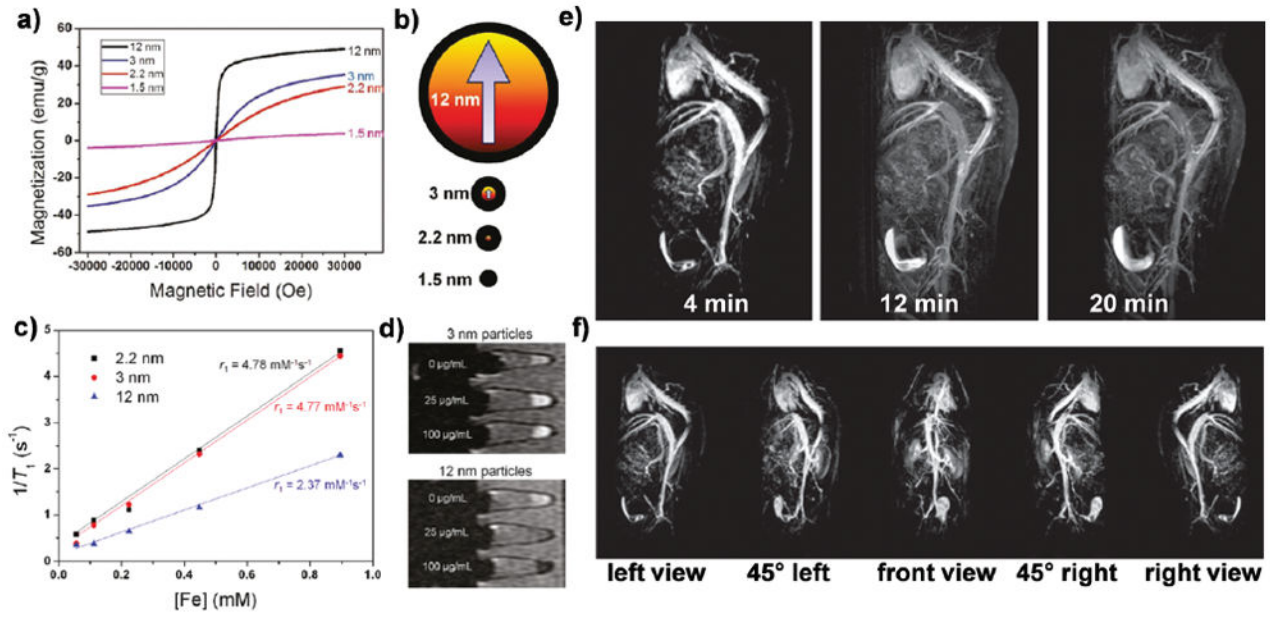

Fig. 5.

(a) Field-dependent magnetization curves at 300 K for iron oxide NPs of varied sizes. (b) Description of spin canting effect (canting layer = 0.9 nm) in iron oxide NPs of varied sizes. Red and black colors represent magnetic cores and magnetically disordered shells. (c) Plots of $1/T_1$ over concentration of iron oxide NPs of 3 nm and 12 nm diameter. (d) T_1-weighted MR images of MCF-7 cell pellets after 24 h incubation with iron oxide NPs of 3 nm and 12 nm in diameters. Reproduced with permission from ref. 135. Copyright 2011, American Chemical Society. (e) T_1-weighted magnetic resonance angiography (MRA) of a mouse injected with ultra-small iron oxide NPs at 7 T. (f) Five different perspectives of MRA images, which were extracted from a 3D scan, at 4 minutes post-injection. Reproduced with permission from ref. 142. Copyright 2017, National Academy of Sciences.

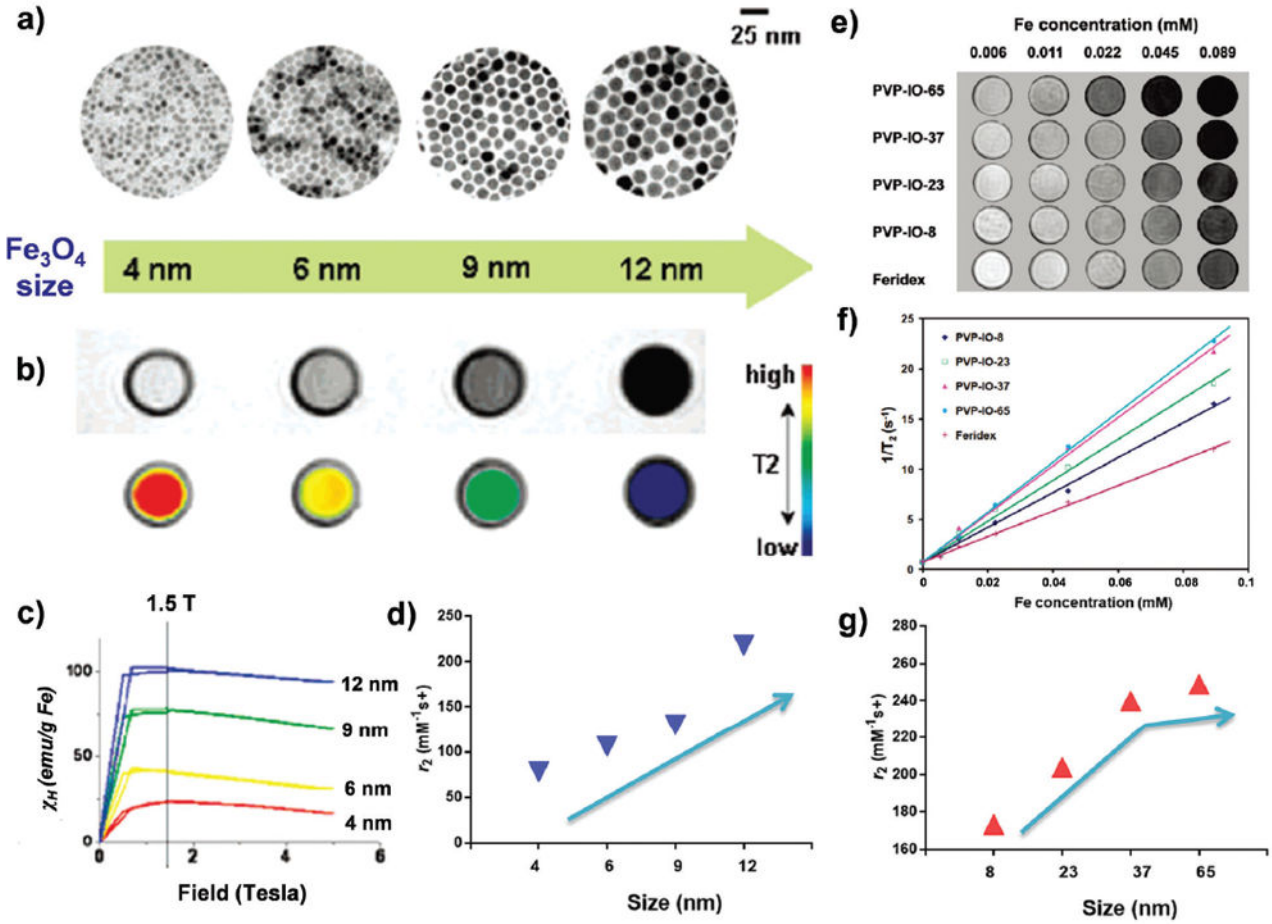

Fig. 6.

(a) TEM images of iron oxide NPs of 4, 6, 9, and 12 nm. (b) Upper panel: Size-dependent T_2-weighted MR images of iron oxide NPs in aqueous solution at 1.5 T; lower panel: size-dependent changes from red to blue in color-coded MR images based on T_2 values. (c) The magnetization of iron oxide NPs measured by a SQUID magnetometer. (d) Size-dependent r_2 values of iron oxide NPs. Reproduced with permission from ref. 79. Copyright 2005, American Chemical Society. (e) Size-dependent T_2-weighted MR images of PVP-coated iron oxide NPs in aqueous solution with various concentrations at 7 T. (f) Plots of $1/T_2$ against Fe concentration of PVP-coated iron oxide NPs. (g) Size-dependent r_2 values of iron oxide NPs. Reproduced with permission from ref. 138. Copyright 2010, American Chemical Society.

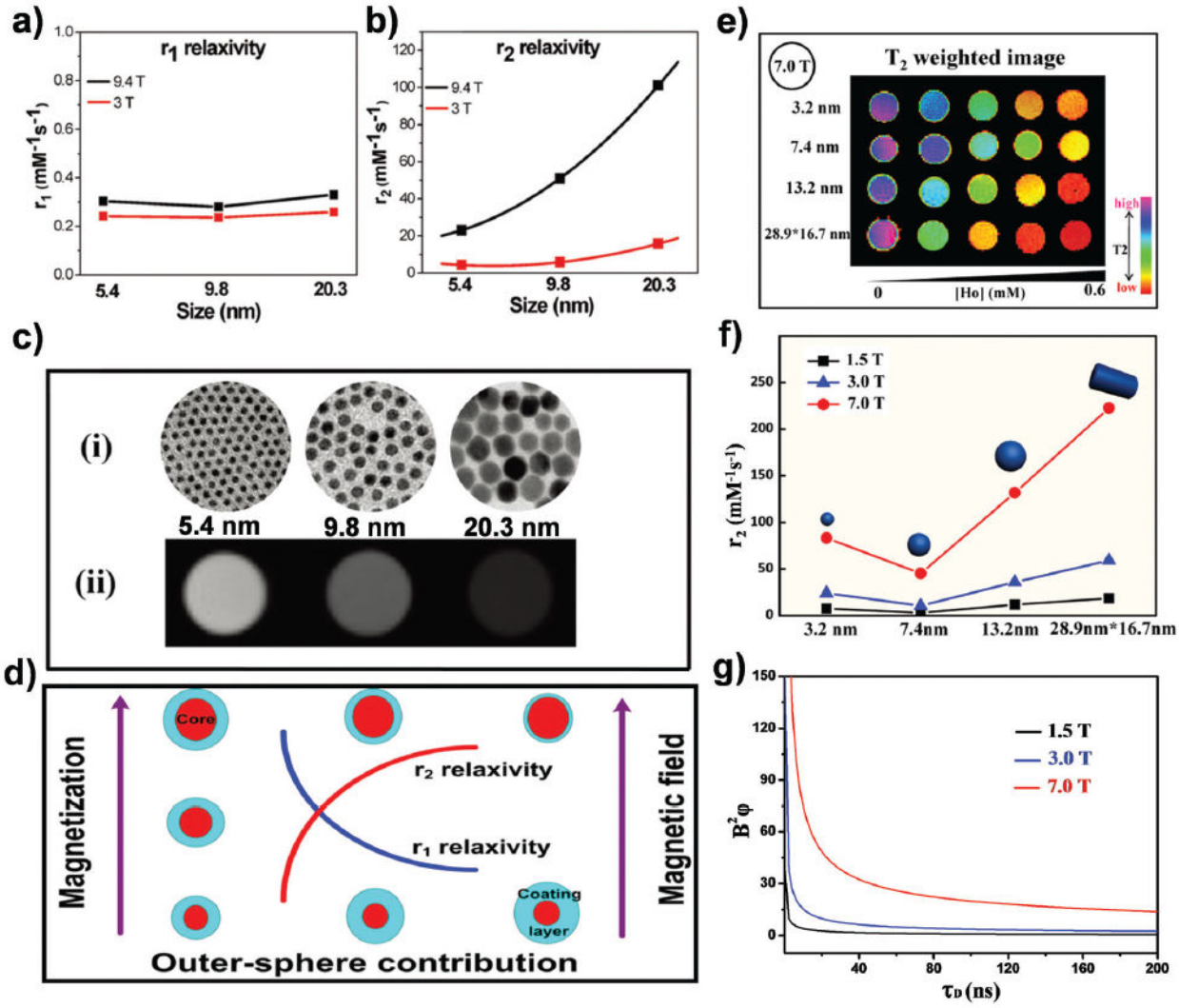

Fig. 7.

(a) r_1 and (b) r_2 values of $NaDyF_4$ NPs (three different sizes) at 3 and 9.4 T. (c) (i) TEM images of 5.4, 9.8, and 20.3 nm $NaDyF_4$ NPs, (ii) phantom MR images of NPs at 1.0 mM Dy^{3+} concentration at 9.4 T. Reproduced with permission from ref. 19. Copyright 2012, American Chemical Society. (d) Schematic of the effect of size and a coating layer on the relaxation of $NaDyF_4$ and $NaHoF_4$ NPs. Reproduced with permission from ref. 20. Copyright 2016, American Chemical Society. (e) T_2-weighted MR images of $NaHoF_4$ NPs of varied sizes in aqueous solutions at 7.0 T. (f) r_2 values obtained for varied sized $NaHoF_4$ NPs at 1.5 T, 3.0 T, and 7.0 T. (g) Simulated curves of $B^2\varphi$ from Curie contribution *versus* diffusion correlation time (τ_D), which is related to NP size. Reproduced with permission from ref. 21. Copyright 2016, Elsevier Ltd.

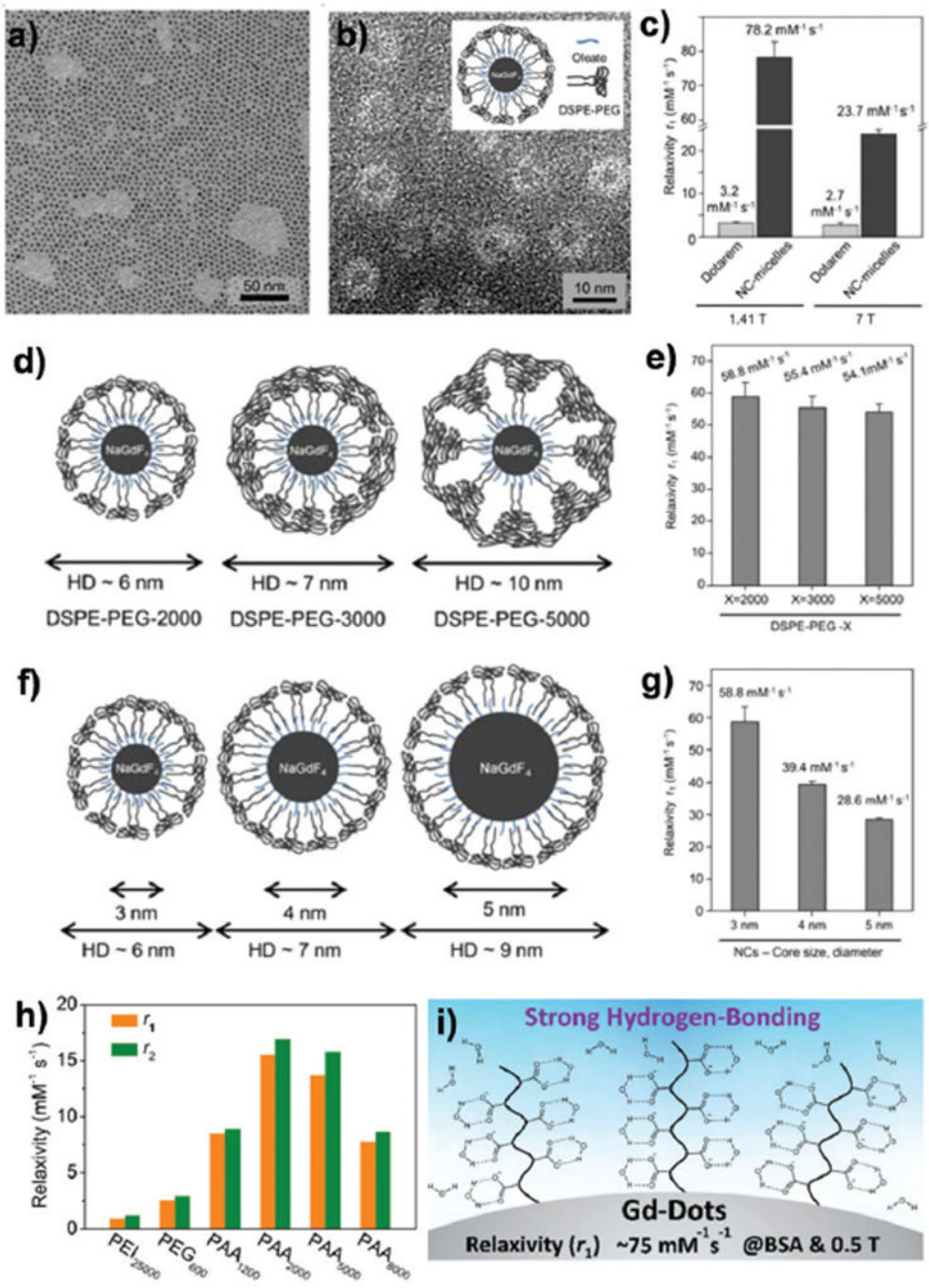

Fig. 8.

(a) A TEM image of ultra-small oleate-stabilized $NaGdF_4$ NPs of 3 nm diameter. (b) A representative negative-stained TEM image of DSPE– PEG-coated NP micelles. Inset: Schematic of a $NaGdF_4$ NP confined within a DSPE–PEG micelle. (c) r_1 values of a clinical MRI contrast agent (Dotarem) and the compact NP micelles at low (1.41 T) and high (7 T) fields. (d) Schematic and (e) r_1 values of $NaGdF_4$ NPs (3 nm) confined within DSPE–PEG micelles with varied PEG chain length. (f) Schematic and (g) r_1 values of $NaGdF_4$ NPs confined within DSPE–PEG micelles with variable core NP size (3–5 nm). Reproduced with permission from ref. 39. Copyright 2016, American Chemical Society. (h) r_1 and r_2 values of

$NaGdF_4$ NPs coated with different ligands measured at 0.5 T. (i) Schematic of the strong hydrogen-bonding capacity of PAA to water molecules to improve r_1. Reproduced with permission from ref. 36. Copyright 2017, American Chemical Society.

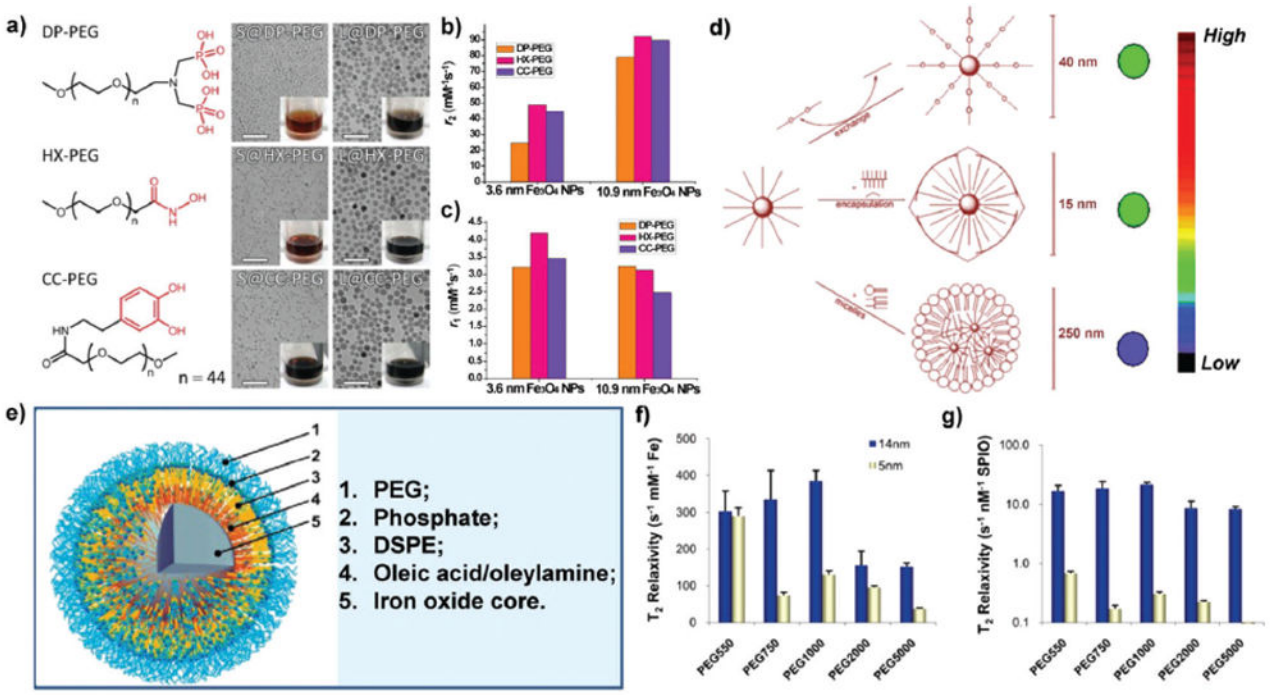

Fig. 9.

(a) Left panel: Chemical structures of PEGs used for exchanging the hydrophobic ligands of 3.6 nm(S: small) and 10.9 nm(L: large) iron oxide NPs; right panel: TEM images of resulting PEGylated NPs (scale bars: 50 nm); insets: photographs of aqueous solutions of PEGylated NPs at an equal Fe concentration of 20 mM. Comparison of (b) r_2 and (c) r_1 values of different kinds of PEGylated NPs. Reproduced with permission from ref. 149. Copyright 2014, Wiley-VCH. (d) Left panel: Schematic of three transfer approaches: ligand exchange of oleic acid with a water-soluble polymer (top), coating of individual NPs with the amphiphilic polymer (middle), and embedding into lipid micelles (bottom). Reproduced with permission from ref. 147. Copyright 2007, American Chemical Society. (e) Schematic of a nanoparticle with 4.8 nm iron oxide core and DSPE-PEG1000 coating. (f) T_2 relaxivity of iron oxide NPs at a constant iron concentration. (g) T_2 relaxivity of NPs on a per-particle basis. Iron oxide NPs with two core sizes, 5 and 14 nm, and five PEG sizes, 550, 750, 1000, 2000, and 5000 Da, were evaluated. Reproduced with permission from ref. 105. Copyright 2010, American Chemical Society.

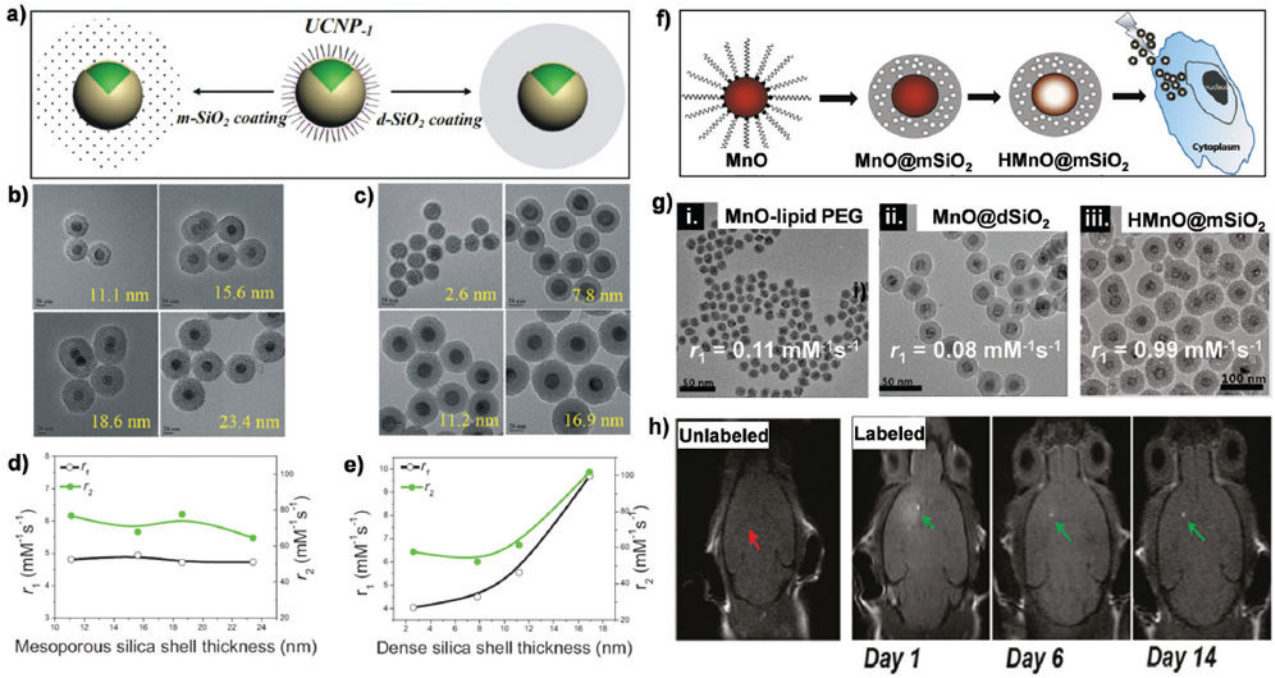

Fig. 10.

(a) Schematic illustration of coating UCNPs with $dSiO_2$ and $mSiO_2$ shells. (b) TEM images of (b) UCNP@$mSiO_2$ and (c) UCNP@$dSiO_2$ with varied shell thicknesses. Scale bar: 20 nm. (d) The plot of r_1 and r_2 *versus* $mSiO_2$ shell thickness. (e) The plot of r_1 and r_2 *versus* $dSiO_2$ shell thickness. Reproduced with permission from ref. 159. Copyright 2014, Wiley-VCH. (f) Schematic of the synthesis of HMnO@$mSiO_2$ NPs and labeling of mesenchymal stem cells. HMnO denotes hollow structure manganese oxide NPs. (g) TEM images and r_1 value of MnO–lipid PEG, MnO@$dSiO_2$, HMnO@$mSiO_2$ NPs. (h) No MRI contrast enhancement (red arrow) was detected in mice transplanted with unlabeled mesenchymal stem cells into the brain, whereas hyperintense signals (green arrows) were detected in mice transplanted with HMnO@$mSiO_2$-labeled mesenchymal stem cells, which were still visible 14 days after injection in the brain. The scheme and figures (with minor modifications) are licensed under the ACS AuthorChoice license. Reproduced with permission from ref. 62. Copyright 2011, American Chemical Society.

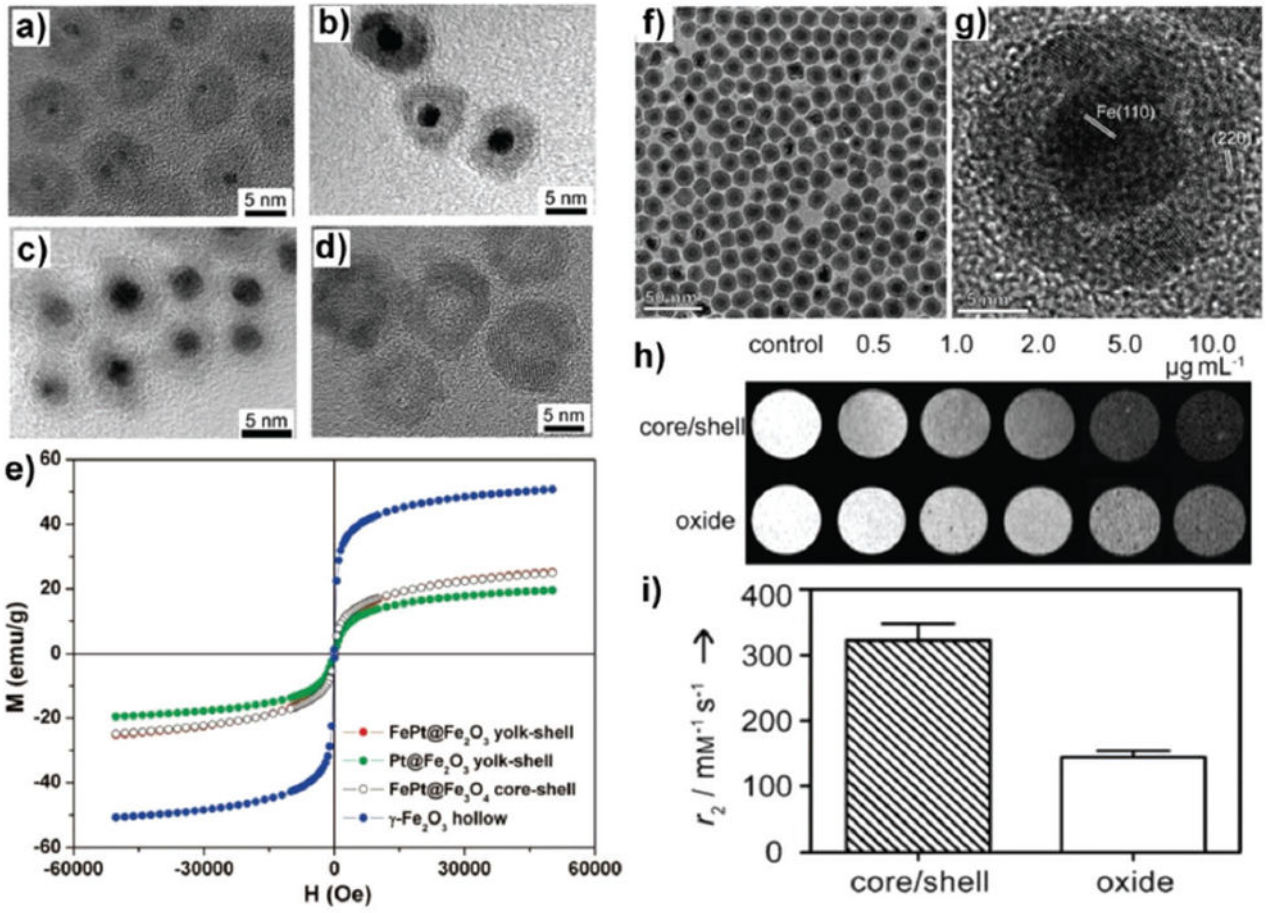

Fig. 11.

HRTEM images of (a) FePt@Fe_2O_3 yolk–shell NPs, (b) Pt@Fe_2O_3 yolk–shell NPs, (c) FePt@Fe_3O_4 core–shell NPs obtained by the seed-growth method, and (d) γ-Fe_2O_3 hollow NPs. (e) Room-temperature field-dependent magnetization measurements of different NPs. Reproduced with permission from ref. 77. Copyright 2008, American Chemical Society. (f) TEM image of 16 nm iron/iron oxide core/shell NPs. (g) HRTEM image showing a core of single-crystal a-Fe and a shell consisting of multiple domains of iron oxide. (h) T_2-weighted MR images at 9.4 T of iron/iron oxide core/shell NPs and iron oxide NPs. (i) r_2 values of the core/shell and oxide NPs determined from the same samples as in (h). Reproduced with permission from ref. 163. Copyright 2011, Wiley-VCH.

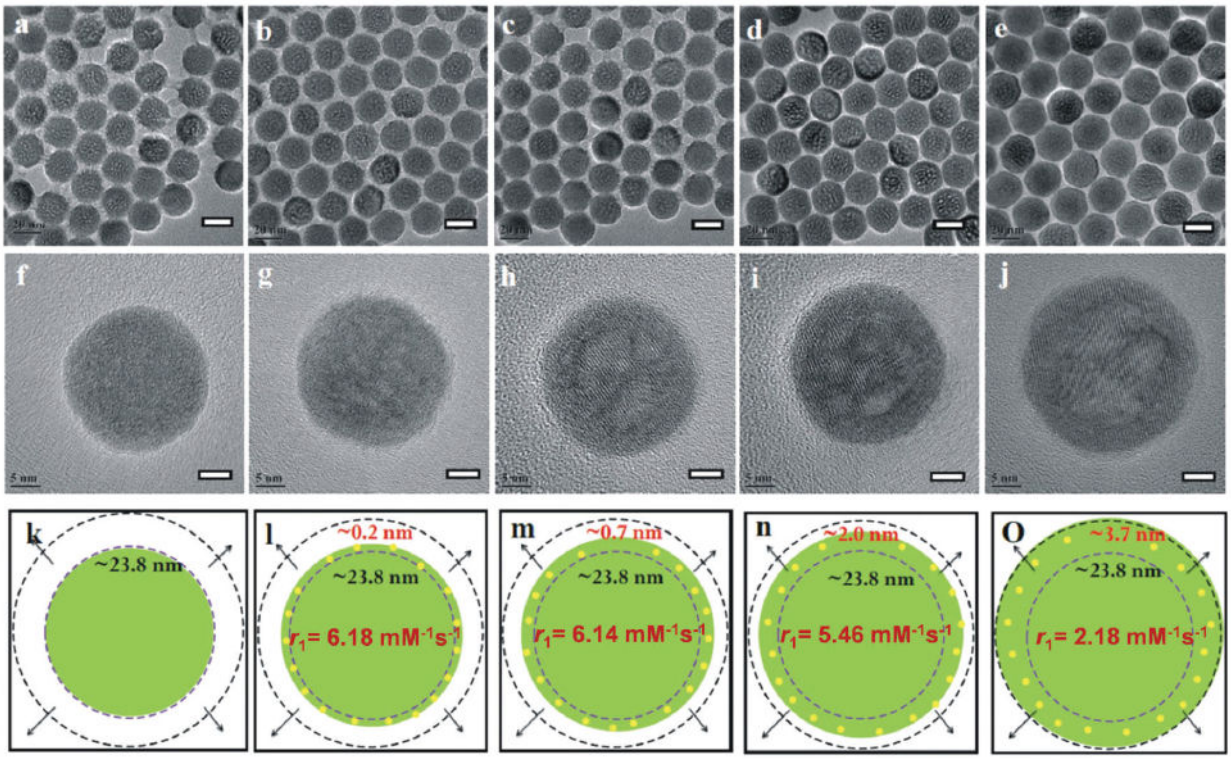

Fig. 12.

TEM images and schematic of Gd-free core (a, f and k) and core@$NaGdF_4$ with varied $NaGdF_4$ shell thicknesses of 0.2 nm (b, g, and l), 0.7 nm (c, h and m), 2.0 nm (d, i, and n), and 3.7 nm (e, j, and o). Yellow dots in l, m, n, and o represent Gd^{3+} ions. The r_1 values of silica-coated water-soluble core@$NaGdF_4$ NPs of various sizes are shown in the middle of the schematic illustrations. Reproduced with permission from ref. 164. Copyright 2011, Wiley-VCH.

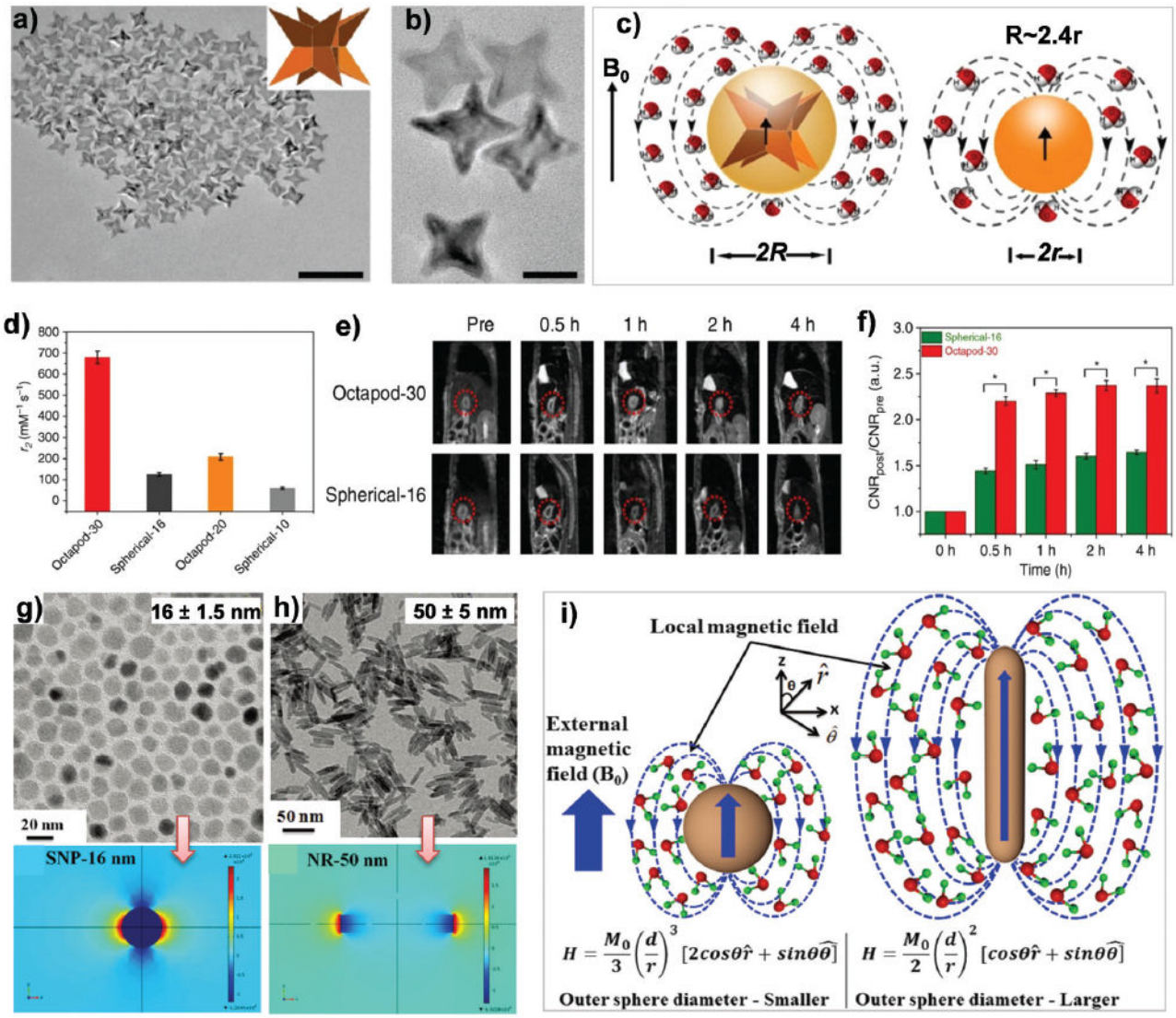

Fig. 13.

Shape effects on T_2 contrast. (a) TEM image (scale bar, 100 nm) and (b) higher magnification TEM image (scale bar, 20 nm) of octapod-30 NPs of uniform four-armed iron oxide NPs. (c) A cartoon showing octapod and spherical iron oxide NPs. With the same geometric core volumes, the octapod NPs have much larger effective volumes (radius, R) than the spherical NPs (radius, r). (d) Comparison of r_2 values of different iron oxide NPs. (e) *In vivo* sagittal MR images and (f) quantification of signal-to-background ratio (*P = 0.01) of orthotopic liver tumor models at 0, 0.5, 1, 2 and 4 h after intravenous injection of octapod-30 and spherical-16 iron oxide NPs. Reproduced with permission from ref. 137. Copyright 2013, Nature Publishing Group. (g and h) Top: TEM images of 16 nm iron oxide NPs (g) and 50 nm NRs (h). Bottom: Local magnetic field generated by the NRs and spherical Fe_3O_4 NPs of equivalent material volumes under an applied magnetic field of 3 T. (i) Schematic of the quantum mechanical outer sphere model of Fe_3O_4 NPs and NRs of the

same material volume. Reproduced with permission from ref. 80. Copyright 2015, Royal Society of Chemistry.

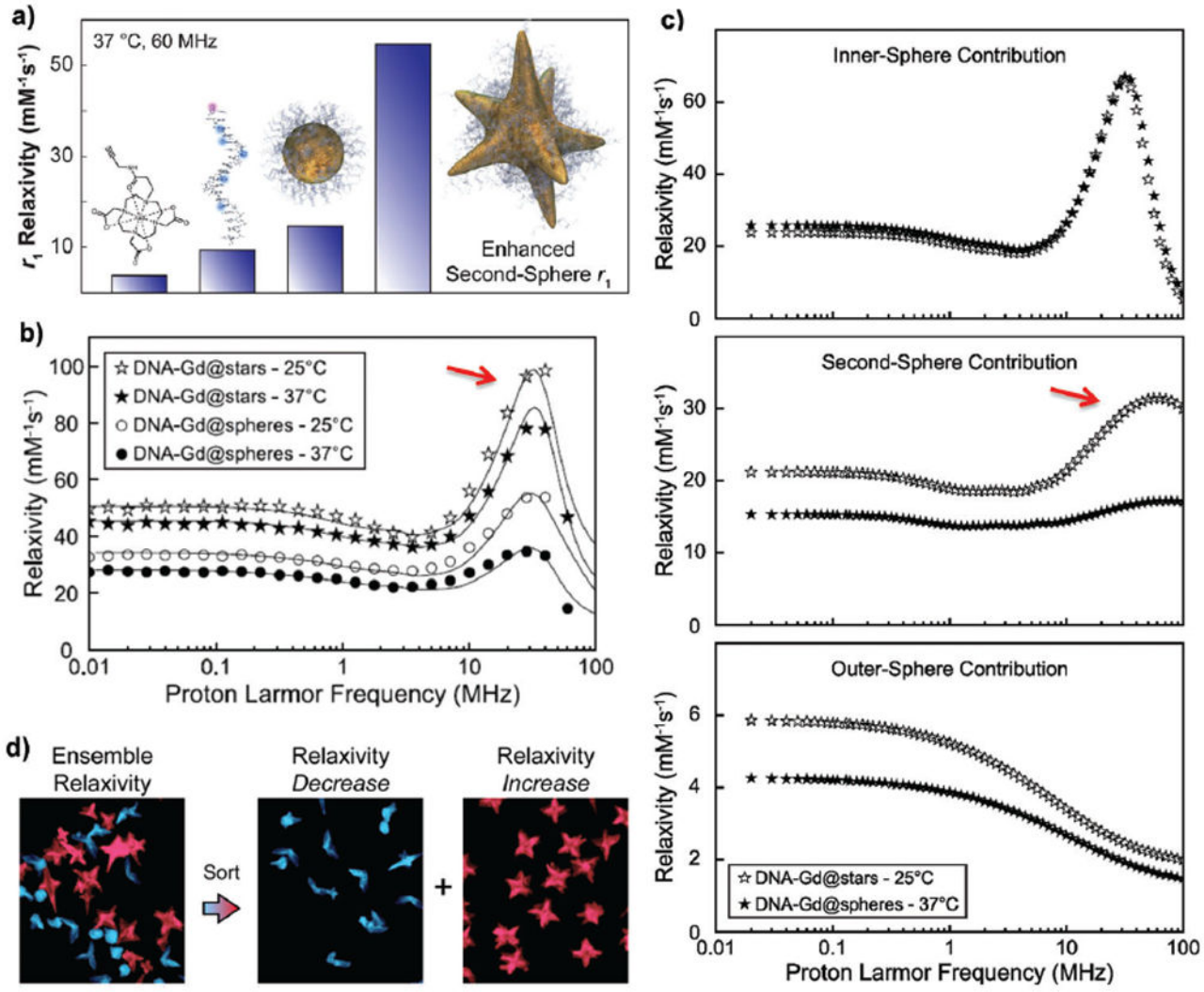

Fig. 14.

Effects of NP shape on T_1 relaxivity. (a) Schematic showing r_1 values of different kinds of MRI CAs including Gd^{3+} chelates, DNA–Gd@spheres, and DNA–Gd@stars. (b) NMRD profiles for water solutions of DNA–Gd@stars and DNA–Gd@spheres. (c) Simulated deconvolution of DNA–Gd@stars NMRD profiles into their inner, secondary, and outer sphere contributions. Reproduced with permission from ref. 95. Copyright 2015, American Chemical Society. (d) Schematic showing the dependence of relaxation on branch numbers of DNA–Gd@stars. Reproduced with permission from ref.94. Copyright 2016, American Chemical Society.

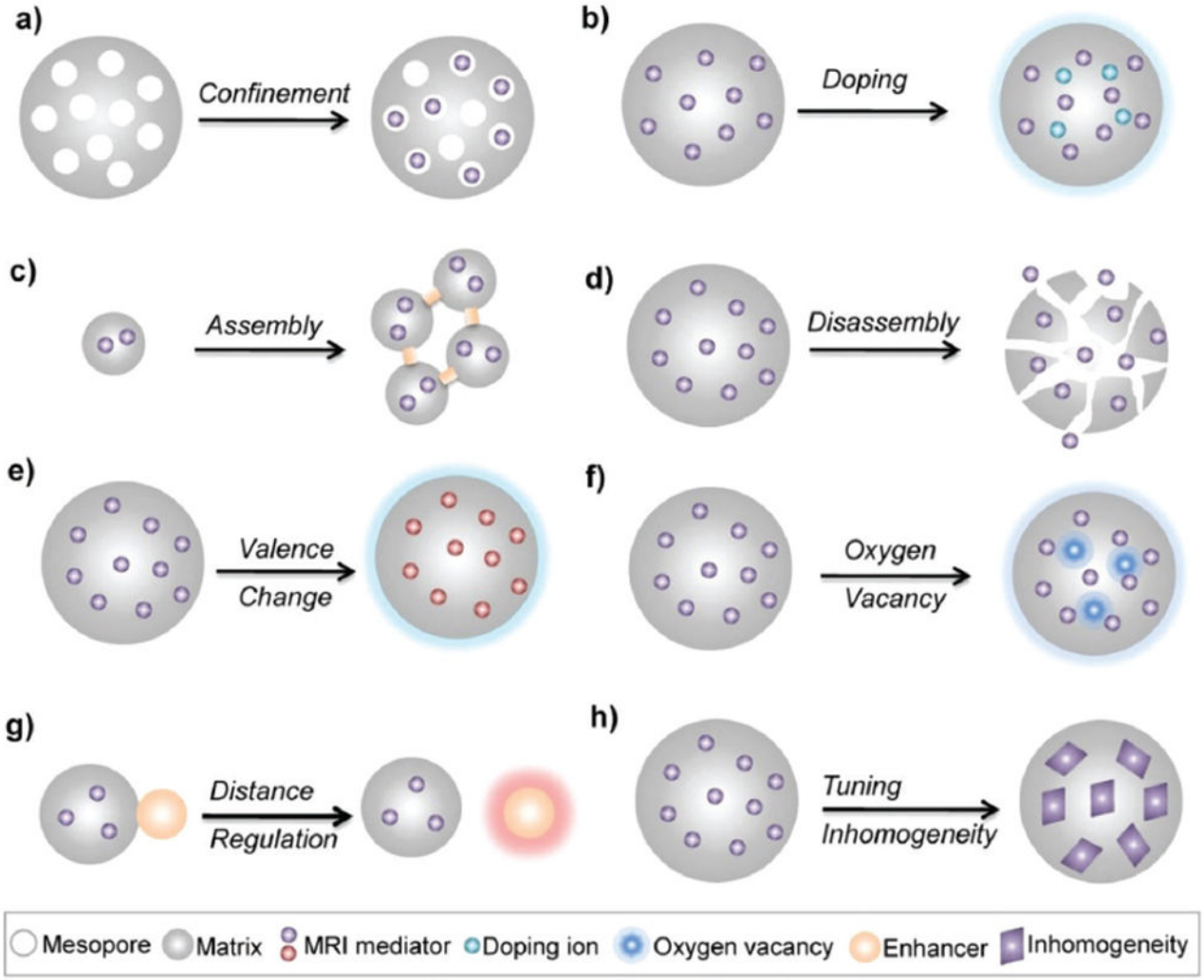

Fig. 15.
Schematic of engineering strategies to obtain high-relaxivity CAs for efficient MRI contrast enhancement.

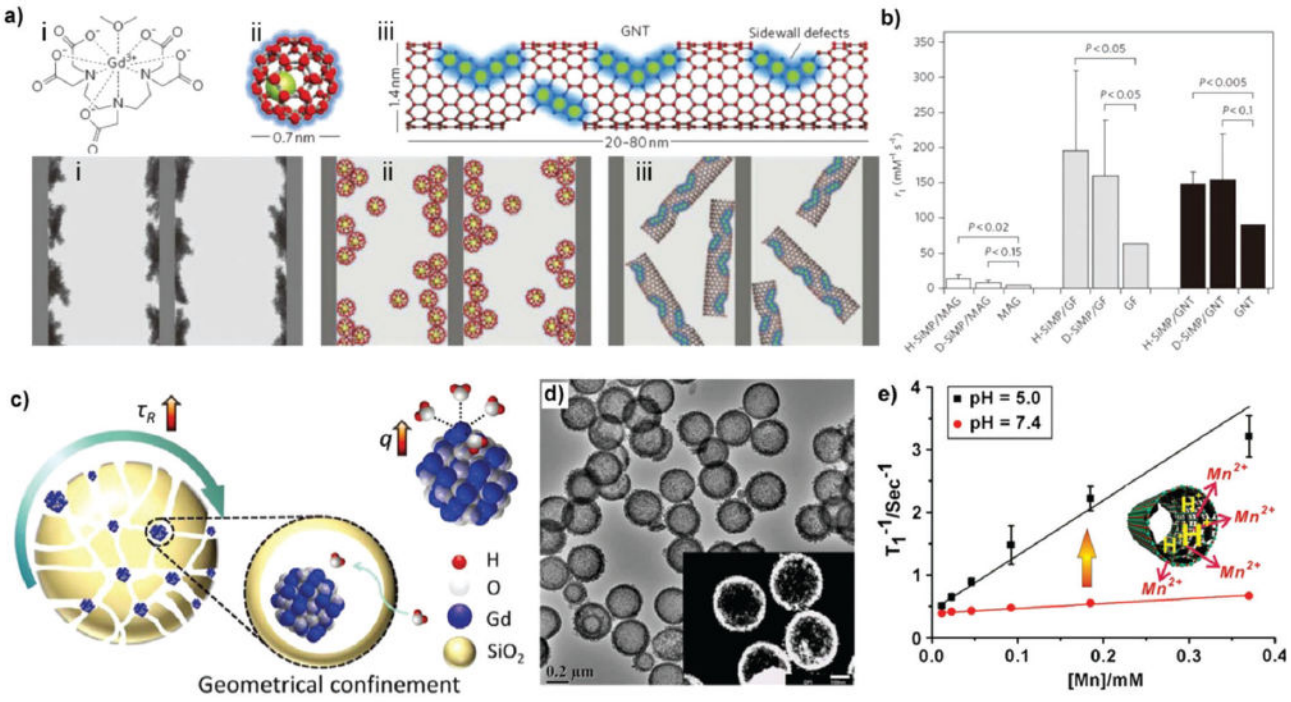

Fig. 16.

(a) Schematics showing (i) Magnevist (MAG), (ii) gadofullerenes (GF), and (iii) gadonanotubes (GNT) and cartoons showing Magnevist, GFs and GNTs entrapped within the porous structure of SiMPs. (b) r_1 values of six MRI CA nanostructures in comparison with corresponding Gd-based CAs at 1.41 T and 37 °C. Reproduced with permission from ref. 186. Copyright 2010, Nature Publishing Group. (c) Schematic of Gd_2O_3 confined in MSNs. Reproduced with permission from ref. 187. Copyright 2016, Royal Society of Chemistry. (d) TEM image of hybrid mesoporous composite nanocapsules (HMCNs). Inset: STEM image with scale bar = 100 nm. (e) Relaxivity of an aqueous suspension of HMCNs after 4 h of soaking in buffer solutions at pH 5.0 and 7.4 at 37 °C. Reproduced with permission from ref. 61. Copyright 2012, Elsevier Ltd.

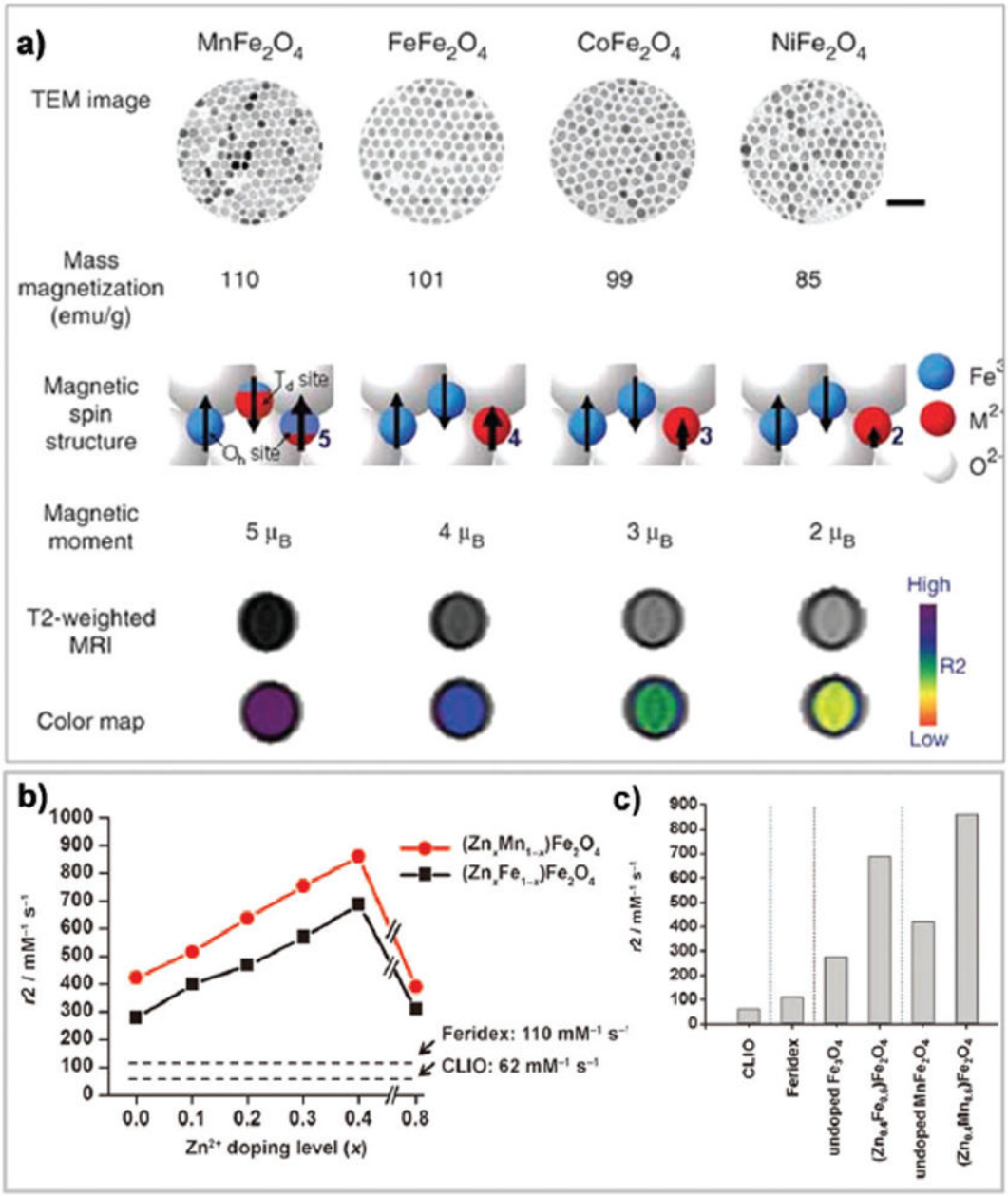

Fig. 17.

(a) TEM images, mass magnetization values, magnetic spin structures, magnetic moments, T_2-weighted images and colormaps of $MnFe_2O_4$, $FeFe_2O_4$, $CoFe_2O_4$, and $NiFe_2O_4$ NPs. Reproduced with permission from ref. 84. Copyright 2007, Nature Publishing Group. (b) Plots of r_2 *versus* Zn^{2+} doping level in $(Zn_xM_{1-x})Fe_2O_4$ (M = Mn^{2+}, Fe^{2+}) NPs at 4.5 T. (c) Comparison of r_2 values of NPs, showing that Zn^{2+} doped NPs have significantly enhanced MRI contrast when compared to conventional iron oxide NPs. Reproduced with permission from ref. 83. Copyright 2009, Wiley-VCH.

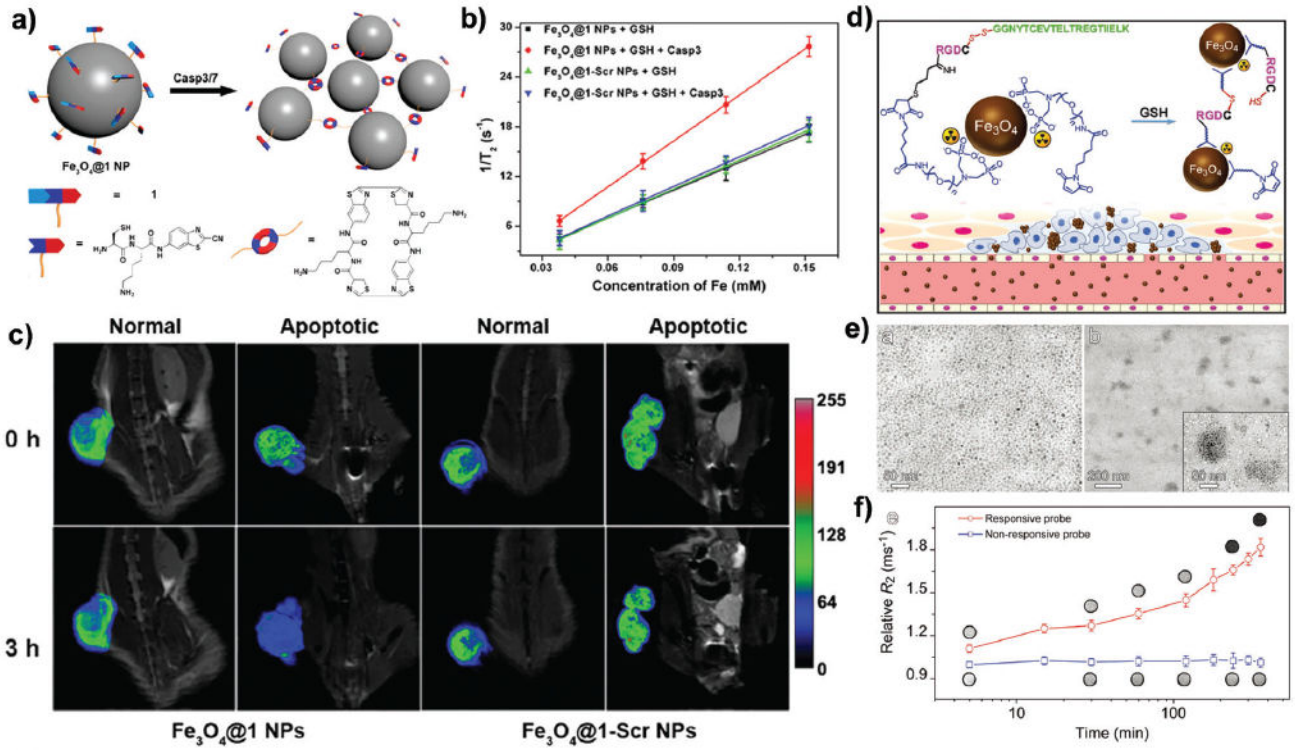

Fig. 18.

(a) Schematic of intracellular caspase-3/7-triggered aggregation of Fe_3O_4@1 NPs. (b) Plots of $1/T_2$ *versus* metal concentration in the presence or absence of caspase-3/7. (c) *In vivo* T_2-weighted coronal images of Fe_3O_4@1 NPs or Fe_3O_4@1-Scr NPs in saline or DOX-treated (*i.e.*, apoptotic) mice in 0 h (top) or 3 h (bottom) post injection. To make tumor apoptotic, about 8 mg kg^{-1} of doxorubicin (DOX) was injected intravenously, once every 4 days three times. Reproduced with permission from ref. 197. Copyright 2016, American Chemical Society. (d) Schematic of ^{99m}Tc-labeled Fe_3O_4 NPs and their responsiveness to GSH-triggering within the tumor microenvironment to form aggregates through inter-particle crosslinking reactions. (e) TEM images of the nonresponsive probe (left panel) and responsive probe (right panel) after being treated with GSH. (f) Temporal evolution of transverse relaxation rate R_2 for both the responsive probe and nonresponsive control recorded on a 3.0 T MRI scanner during incubation with GSH (inset: T_2-weighted images of probe solutions acquired at different incubation time points). Reproduced with permission from ref. 198. Copyright 2017, Wiley-VCH.

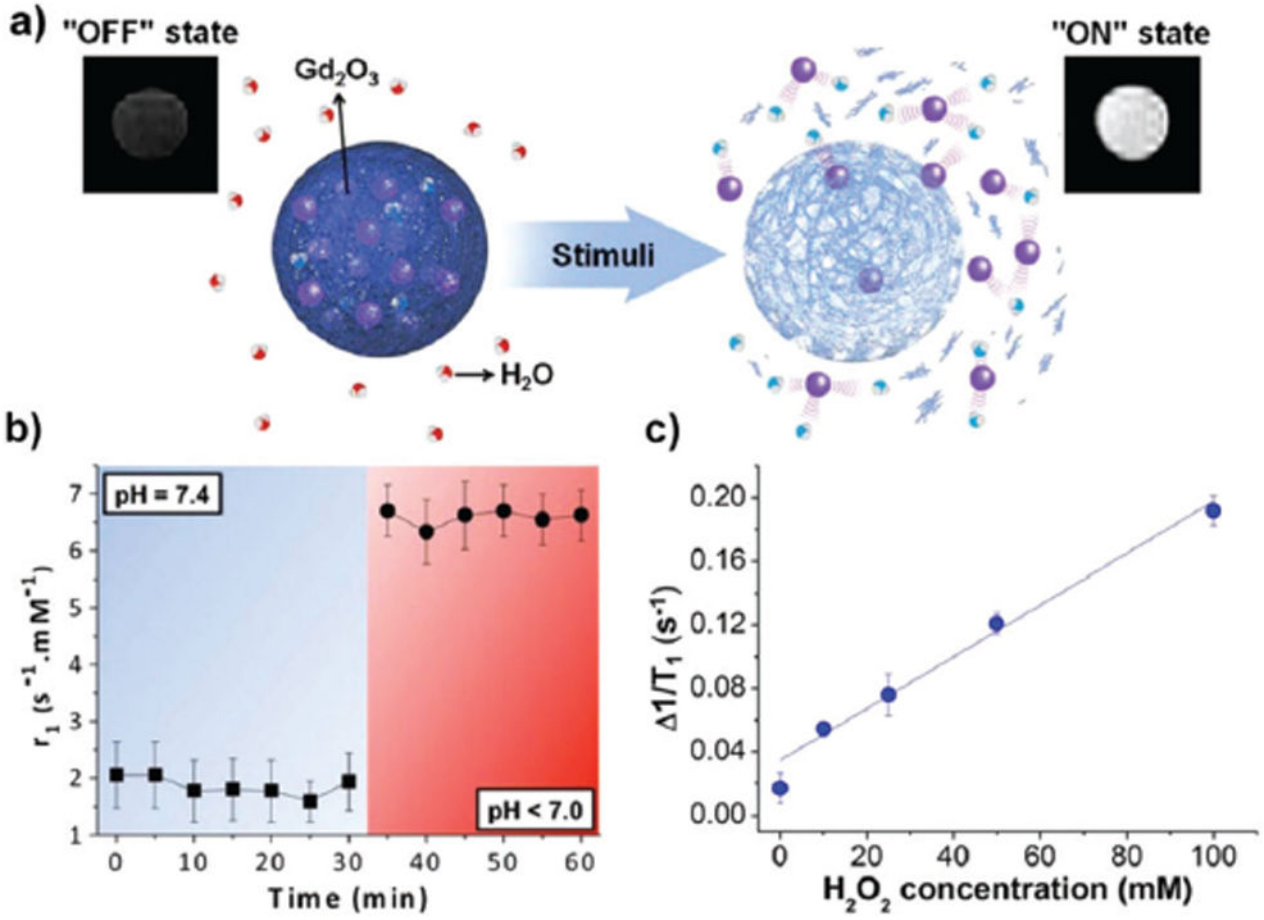

Fig. 19.

(a) Schematic of how a degradable polymermatrix is able to control the interaction of water molecules with Gd_2O_3 NPs (purple spheres). (b) Magnetic relaxivity of Gd_2O_3 NPs encapsulated in pH-responsive materials demonstrates a jump from neutral pH to mild acidity. (c) Increasing concentrations of H_2O_2 results in corresponding increases in the T_1 relaxation rates of Gd_2O_3 NPs encapsulated in an H_2O_2-responsive polymer. Reproduced with permission from ref. 131. Copyright 2013, American Chemical Society.

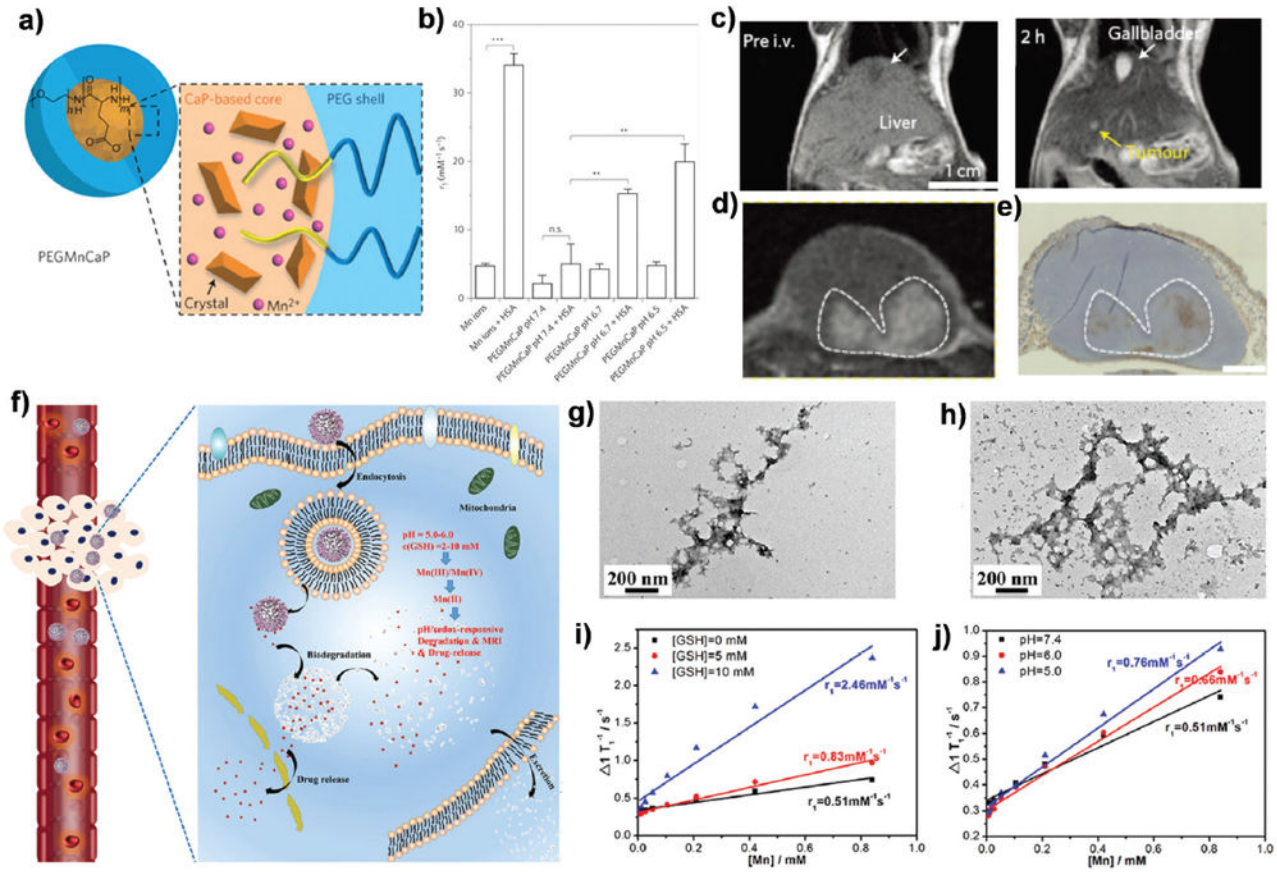

Fig. 20.

(a) Schematic of the hybrid structure of PEGMnCaP. PEGMnCaP consists of a CaP-based core and a PEG shell. The Mn^{2+} ions are trapped in the CaP core. (b) r_1 value of PEGMnCaP in physiological environments at different pH levels, with and without proteins (for example, HSA). (c) MR images of liver metastasis using 1 T MRI scanner after i.v. injection of PEGMnCaP NPs. Scale bar, 1 cm. (d) MR images of a hypoxic region within a C26 tumor at 1 T, 4 h after the i.v. injection of PEGMnCaP NPs. (e) Staining of tumor tissues with pimonidazole confirmed that the hypoxic regions (brown) are at the same location as the tumor regions with higher MRI contrast enhancement. Scale bar, 1 mm. Reproduced with permission from ref. 52. Copyright 2016, Nature Publishing Group. (f) Schematic of the disassembly of PEG/Mn–HMSNs through “manganese extraction” and release of Mn^{2+} component intracellularly. TEM images showing structural evolution of Mn–HMSNs after biodegradation at a GSH concentration of (g) 5.0 and (h) 10 mM at pH 5.0 for 48 h. (i) Plot of $1/T_1$ *versus* Mn concentration for PEG/Mn–HMSN solution at varied GSH concentrations and (j) at varied pH. Reproduced with permission from ref. 208. Copyright 2016, American Chemical Society.

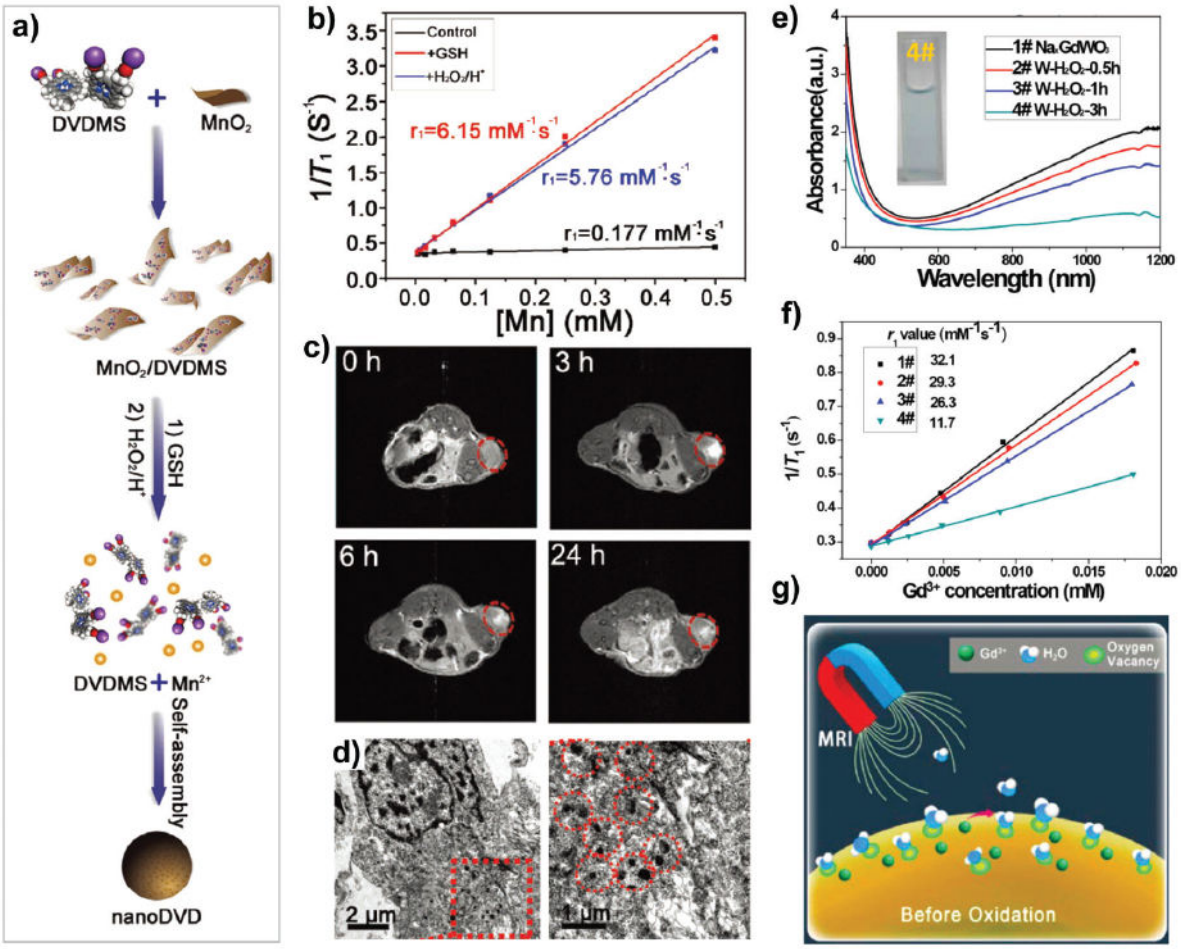

Fig. 21.

(a) Schematic illustration showing the fabrication process of MnO_2/DVDMS and the reaction in GSH solution or with H_2O_2 (pH 5.5). (b) Plot of $1/T_1$ *versus* Mn concentration for MnO_2/DVDMS (black line), MnO_2/DVDMS + GSH (red line), and MnO_2/DVDMS + H_2O_2/H^+ (blue line) solutions. (c) T_1-weighted MR images before and after injection of MnO_2/DVDMS. (d) TEM images of MCF-7 tumor sections at 24 h after injection of MnO_2/DVDMS. Reproduced with permission from ref. 211. Copyright 2017, Wiley-VCH. (e) UV-vis-NIR absorption spectra and (f) plot of $1/T_1$ *versus* Gd^{3+} concentration of PEG–Na_xGdWO_3 nanorods after oxidization with H_2O_2 for varied time periods: 1#: 0 h; 2#: 0.5 h; 3#: 1 h; 4#: 3 h. (g) Schematic of the affinity of oxygen vacancies for oxygen atoms and its impact on the interaction between water molecules and Gd^{3+} ions. Reproduced with permission from ref. 37. Copyright 2017, American Chemical Society.

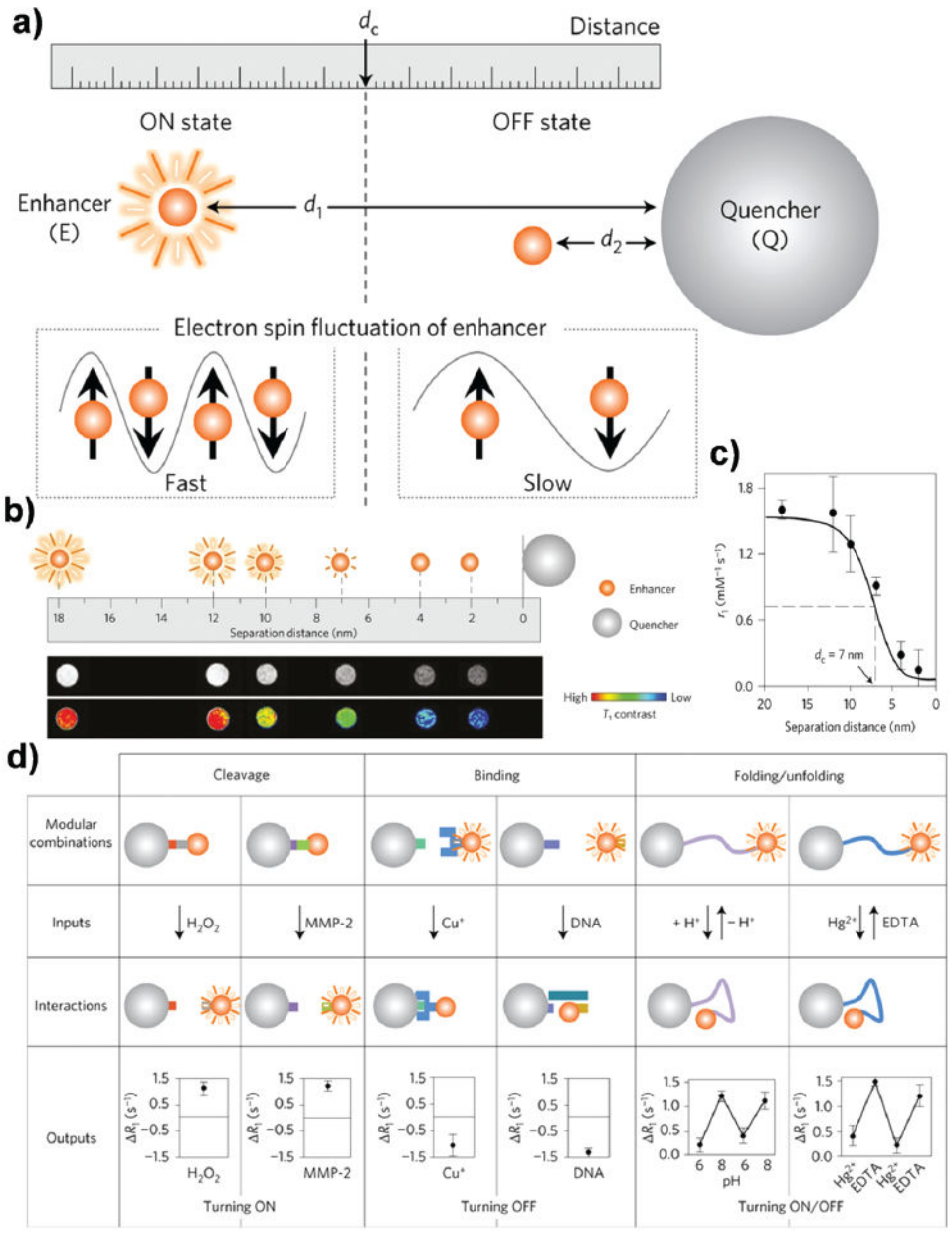

Fig. 22.

(a) Schematic representation of distance-dependent magnetic resonance tuning. (b) Schematic of a nanoscale ruler that shows a variable T_1 MRI signal, dependent on the separation distance between the paramagnetic enhancer (Gd-DOTA) and superparamagnetic quencher (*i.e.*, 12 nm $Zn_{0.4}Fe_{2.6}O_4$ particle). Lower panel: T_1-weighted MR image and color map image of a solution containing the enhancer and quencher with varied separation distances. (c) A plot of r_1 values *versus* separation distance. (d) Schematic of modular combinations for the preparation of distance-dependent magnetic resonance sensors, operated using three different modes of interactions (cleavage, binding, and conformational changes) and subsequent T_1 MRI signal outputs. Reproduced with permission from ref. 213. Copyright 2017, Nature Publishing Group.

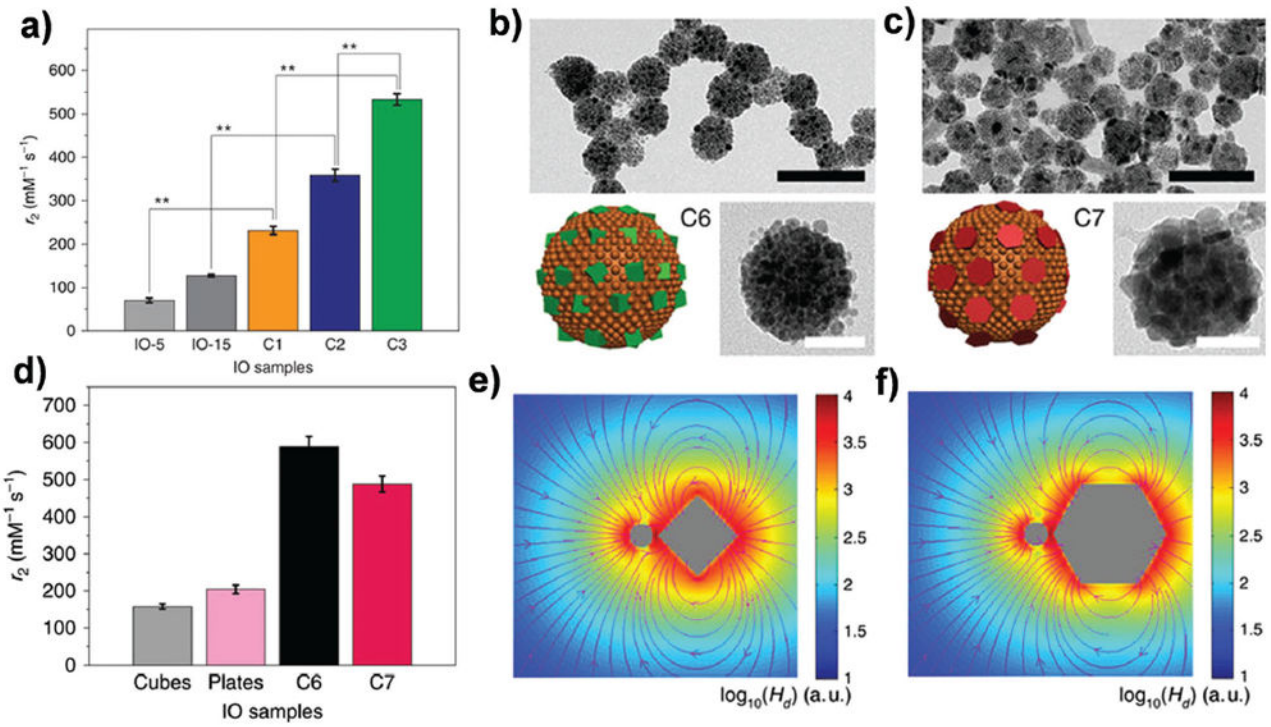

Fig. 23.

(a) Columns showing r_2 values of iron oxide (IO) clusters, as well as the single IO-5 and IO-15 NPs. C1: clusters of 5 nm NPs only; C2: clusters of 15 nm NPs only; C3: clusters of mixed 5 nm NPs and 15 nm NPs. (b and c) TEM and high-resolution TEM images, as well as cartoons of clusters C6 (IO cubes) and C7 (IO nanoplates), respectively. (d) Columns showing r_2 values of IO clusters C6 and C7, as well as the single IO cubes and plates. (e and f) Simulation models and calculated stray fields for clusters C6 and C7, respectively. Color bars represent $\log_{10}(H_d)$, where H_d is the calculated stray field. Reproduced with permission from ref. 214. Copyright 2017, Nature Publishing Group.

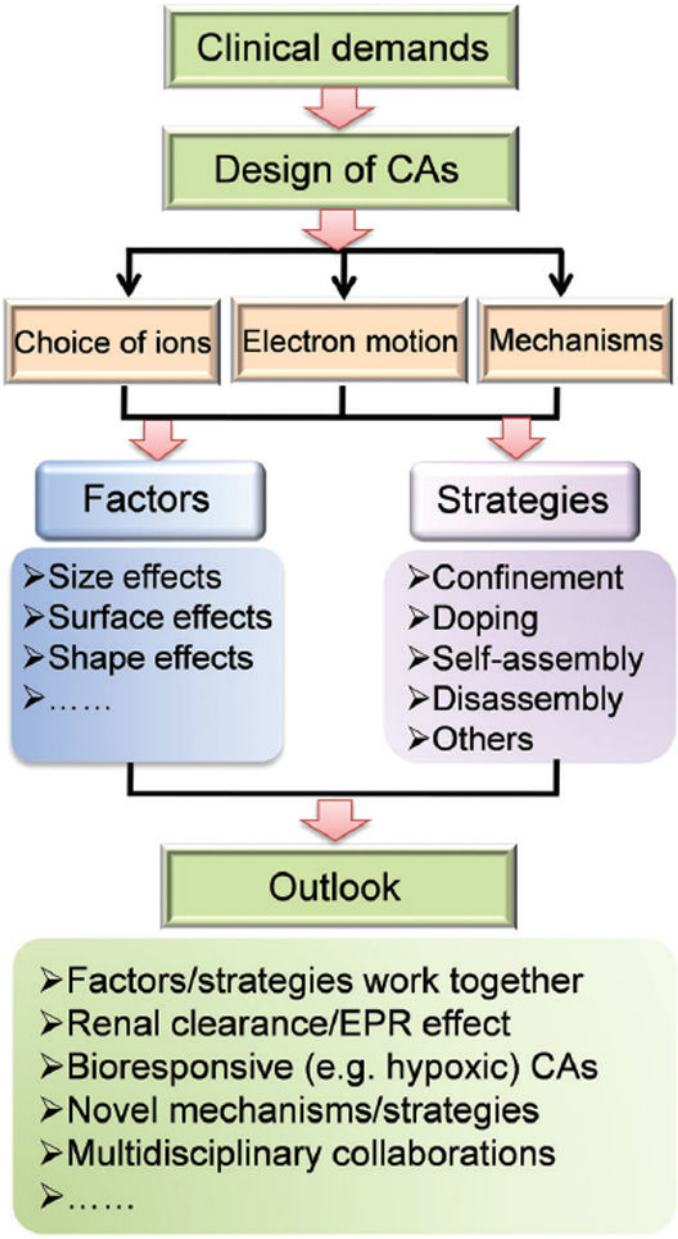

Fig. 24.
Summary and outlooks of designing inorganic NPs for MRI.

Table 1

Outer orbital and quantum parameters of metal ions

Ion	Orbital	*S*	*L*	*J*	(μ_{eff} μ_B)
Mn^{2+}	$3d^5$	5/2	0	5/2	5.92
Mn^{4+}	$3d^3$	3/2	3	9/2	3.87
Fe^{2+}	$3d^6$	2	2	4	4.90
Fe^{3+}	$3d^5$	5/2	0	5/2	5.92
Co^{2+}	$3d^7$	3/2	3	9/2	3.87
Co^{3+}	$3d^6$	2	2	4	4.90
Cu^{2+}	$3d^9$	1/2	2	5/2	1.73
Eu^{2+}	$4f^7$	7/2	0	7/2	7.94
Eu^{3+}	$4f^6$	3	3	0	—
Gd^{3+}	$4f^7$	7/2	0	7/2	7.94
Dy^{3+}	$4f^9$	5/2	5	15/2	10.65
Ho^{3+}	$4f^{10}$	2	6	8	10.61

Table 2

Representative inorganic nanoparticle size effect on relaxivity

NPs	Shape	Approximate size (nm)	Surface coating	Relaxivity (mM^{-1} s^{-1})	Field (T)	Ref.
$NaGdF_4$	Sphere	2.5/4.0/6.5/8.0	PVP	r_1 = 7.2/4.5/3.3/3.0	1.5	49
$NaGdF_4$	Sphere	5/15/20	PEG	r_1 = 6.2/5.7/8.78	3.0	41
$NaGdF_4$	Sphere	2.1/3.2/8.6	PAA	r_1 = 47.3/27.5/15.3	0.5	36
$NaGdF_4$	Sphere	3/4/5	PEG	r_1 = 58.8/39.4/28.6	1.4	39
Gd_3O_2	Sphere	2.2/3.8/4.6	SiPEG	r_1 = 8.8/8.8/4.4	7.0	45
Gd_3O_2	Sphere	4.4/5.4/10.1	Albumin	r_1 = 18.49/16.22/12.26	1.5	129
MnO	Irregular	7/15/20/25	PEG	r_1 = 0.37/0.18/0.13/0.12	3.0	69
Mn_2O_3	Sphere	3/5/11/13	PEG	r_1 = 2.38/1.39/0.99/0.41	1.5	132
Mn_2O_3	Tetrahedron	6/8/20	PEG	r_1 = 1.08/0.63/0.25	1.5	132
Fe_2O_3	Sphere	2.2/3/12	PEG	r_1 = 4.78/4.77/2.37	1.5	135
$MnFe_2O_4$	Sphere	2/3/3.9	PEG	r_1 = 8.43/8.23/6.98	3.0	136
Fe_3O_4	Sphere	4/6/9/12	DMSA	r_2 = 78/106/130/218	1.5	79
Fe_3O_4	Octapod	20/30	HDA-G2	r_2 = 679/209	7.0	137
Fe_3O_4	Sphere	8/23/37/65	PVP	r_2 = 173/204/240/249	7.0	138
Fe_3O_4	Rod	30[a]/40/50/60/70	PEI	r_2 = 312/381/427/545/608	3.0	80
$MnFe_2O_4$	Sphere	6/9/12	DMSA	r_2 = 208/265/358	1.5	84
$NaDyF_4$	Sphere	5.4/9.8/20.3	PEG	r_2 = 32/51/101	9.4	19
$NaDyF_4$	Rod	19[a]/20/25/35	PEG	r_2 = 75/65.2/91.4/204.4	9.4	20
$NaHoF_4$	Sphere	10.6/14.1/16.4	PEG	r_2 = 31.9/51.5/70.4	9.4	20
$NaHoF_4$	Sphere	3.2/7.4/13.2	PEG	r_2 = 83.4/45.4/131.7	7.0	21

[a]Length of nanorods.

Table 3

Full names and their corresponding abbreviations

Full name	Abbreviation	Full name	Abbreviation
5-Aminolevulinic acid	5-ALA	Mesoporous silica nanoparticles	MSNs
Catechol	CC	Mercaptosuccinic acid	MSA
Chemical exchange saturation transfer	CEST	Motional averaging regime	MAR
Computed X-ray tomography	CT	Nanoparticles	NPs
Dense silica	$dSiO_2$	Nanorods	NRs
Diethylenetriaminepentaacetic acid	DTPA	Nuclear magnetic relaxation dispersion	NMRD
Diffusion correlation time	τ_D	Number of bound water molecules	q
Diphosphate	DP	Poly(acrylic acid)	PAA
Contrast agents	CAs	Photoacoustic	PA
Distearyl phosphatidylethanolamine	DSPE	Polyethylene glycol	PEG
2,3-Dimercaptosuccinic acid	DMSA	Polyethylenimine	PEI
Effective magnetic moment	μ_{eff}	Polyvinylpyrrolidone	PVP
Electron spin angular momentum	S	Poly(maleic anhydride-*alt*-1-octadecene)	PMAO
Electron orbital angular momentum	L	Poly(maleic acid)-octadecene	PMO
Enhanced permeation and retention	EPR	Reticuloendothelial system	RES
Glutathione	GSH	Silicon microparticles	SiMPs
1-Hexadecylamine	HDA	Rotational correlation time	τ_R
High-resolution	TEM	HRTEM Saturation magnetization	M_s
Hollow mesoporous silica nanoparticles	HMSNs	Sinoporphyrin sodium	DVDMS
Hydroxamate	HX	Solomon–Bloembergen–Morgan	SBM
Lanthanide	Ln	Static dephasing regime	SDR
Magnetic resonance angiography	MRA	Transmission electron microscopy	TEM
Magnetic resonance imaging	MRI	Total electron angular momentum	J
Magnevist	Gd–DTPA	Upconversion nanoparticles	UCNPs
Mesoporous silica	$mSiO_2$	Water residence time	τ_M